MCNP SIMULATIONS FOR STANDOFF BOMB DETECTION USING NEUTRON INTERROGATION

by

MARK JOHLL

B.S., Benedictine College 2007

A THESIS

submitted in partial fulfillment of the requirements for the degree

MASTER OF SCIENCE

Department of Mechanical and Nuclear Engineering
College of Engineering

KANSAS STATE UNIVERSITY
Manhattan, Kansas

2009

Approved by:

Major Professor
Dr. William L. Dunn

Copyright

Abstract

This report investigates the feasibility of a standoff interrogation method to identify nitrogen-rich explosive samples shielded by other materials ("clutter") using neutron beams from ^{252}Cf and deuterium-tritium (D-T) generator sources. Neutrons from the beams interact with materials in the target to produce inelastic-scatter gamma rays, and, after slowing down to thermal energies, prompt-capture gamma rays. By detection of these gamma rays, a response vector is formed that is used to calculate a figure-of-merit, whose value is dependent upon the contents of the target. Various target configurations, which include an inert-material shield and a sample that may or may not be explosive, were simulated using the MCNP5 code. Both shielding and collimation of 14.1-MeV neutron beams were simulated to produce effective neutron beams for target interrogation purposes and to minimize dose levels. Templates corresponding to particular target scenarios were generated, and their effectiveness at nitrogen-rich explosive identification was explored. Furthermore, methods were proposed yielding more effective templates including grouping target responses by density and composition. The results indicate that neutron-based interrogation has potential to detect shielded nitrogen-rich explosives. The research found that using a tiered filter approach, in which a sample must satisfy several template requirements, achieved the best results for identifying the explosive cyclonite (RDX). A study in which a 14.1-MeV neutron beam irradiated a target containing a shielded sample, which could either be explosive (RDX) or inert, yielded no false negatives and only 2 false positives over a large parameter space of clutter-sample combinations.

Table of Contents

List of Figures

List of Tables

Acknowledgements

I would like to thank Dr. Dunn for allowing me to work on the project Standoff Bomb Detection. I would also like to thank Tom Dunn and M2 technologies for their financial assistance and support. I am thankful to Dr. Shultis for the design work in shielding the neutron generator source and for the plan of the beam catcher. Finally, I am grateful to all the other members of the Standoff Bomb Detection team for their hard work, particularly Kennard Callender for his help in the theoretical side of the project.

Dedication

This work is dedicated to my family, for their generous support and love.

CHAPTER 1 - Introduction

1.1 Definitions of IEs and IEDs

Throughout history, attempts have been made to cause destruction through the release of energy. One device that achieves this malicious goal is the IED, the Improvised Explosive Device, based on IEs or Improvised Explosives. IEs are, "compounds or mixtures of compounds, which have explosive properties and should be relatively easily prepared by laymen under simple conditions (home made) using freely available chemicals and information" (Schubert, 2006). Next, IED's are defined as, "explosive charges with IE-material in confined or unconfined shape, equipped with commercial or improvised initiators" (Schubert, 2006). An alternative definition of an IED is, "a device placed or fabricated in an improvising manner incorporating destructive, lethal, noxious, pyrotechnic, or incendiary chemicals and designed to destroy, incapacitate, harass or distract. It may incorporate military stores, but is normally devised from nonmilitary components" (Iraq Coalition Casualty Count, 2008).

1.2 Brief History and Description of the IED Problem

Explosives have been used for hundreds of years but IEDs employed in numerous amounts first occurred in World War II. After being introduced, IEDs have been a constituent of almost every major conflict since then, including Vietnam, Northern Ireland, and the war with Afghanistan, and they have a strong presence in the current war with Iraq through the Al Quaeda and Coalition Forces (Marolda, 2003; Sigaltchik, 1970; Iraq Coalition Causality Count, 2008). In the last decade, the audacity of acts of terrorism has dramatically increased across the world, as the attack on the World Trade Center on Sept. 11, 2001 indicates. During the months May to August 2007 in Iraq, there were more than 250 recorded fatalities from IEDs (Iraq Coalition Causality Count, 2008). Terrorists, who employ almost any type of destructive technology, particularly favor the IED for its versatility and destructive power. Thus, an urgent need exists for a type of technology that will detect IEDs effectively in many scenarios to decrease their destruction in both war and acts of terror. Currently, no comprehensive solution to the problem exists, particularly in regards to IED identification in bulk or cargo containers (Runkle, et al. 2009).

Many lives have been altered because of IEDS with total casualties for the year 2007, over many world regions (see Figure 1.1), of 5,426 documented, of which 71% were civilians (Mines Action Canada, 2008). The country with the most casualties from IEDs during 2007 was Columbia. However, IEDs have spread to most regions of the world and will most likely continue to spread as technology increases and world trade expands. Additionally, even if the number of IEDs does not increase dramatically in the future, thousands of IEDs and mines remain buried in fields from previous wars with ominous potential. By their nature, numerous types of IEDs exist, a fact that adds to the complexity of the detection process. Also, IEDs may vary in composition, design, and placement or concealment.

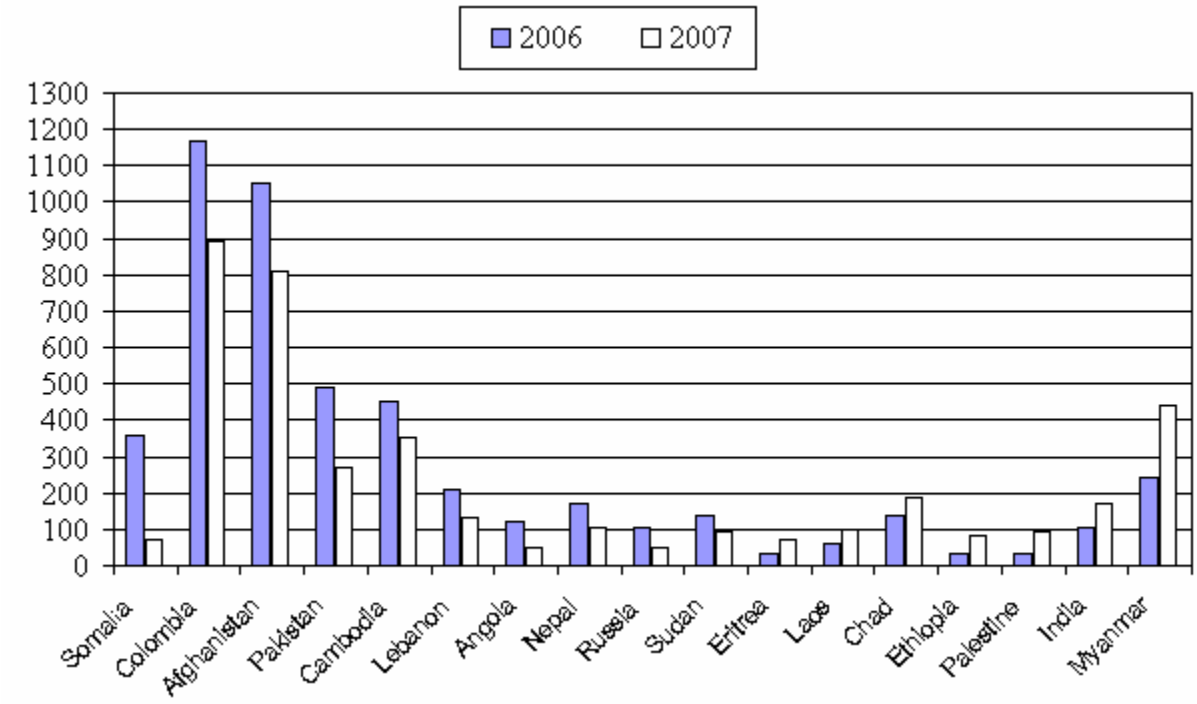

Figure 1.1 IED casualties in 2006 and 2007 in several countries (Mines Action Canada, 2008).

1.2.1 Explosives Utilized in IEDs

Many different types of explosives are used in IED fabrication, but they can be grouped into three main classes. One of the most common classes of explosives utilized in IEDs is military explosives, consisting of standard military explosives or mixtures of standard military explosive compounds. Examples of such compounds include TNT, PETN, RDX, HMX, NG, NC and others (Mostak and Stancl, 2006). Additionally, demilitarized explosives are often

employed. These are a subclass of military explosives and consist of a similar chemical composition to military explosives, however, in a dismantled or processed form. A second class is industrial explosives, which are used for mine blasting or other projects needing demolition capabilities. Examples of these types of explosives are primarily dynamites, ammonites, ANFO, slurries, emulsions and black powder (Mostak and Stancl, 2006). Finally, purely improvised explosives are a third category. These types of substances, in principle, have no limitations other than that they are inherently chemically unstable and possess the potential for the release of exothermic energy. Examples of such substances are organic peroxides and ammonium nitrates – fuel, oil sugar mixtures etc. (Mostak and Stancl, 2006). Because of a lack of group structure, when purely improvised explosives are used to make IEDs, they often prove the most difficult to detect. However, IEs and IEDs are often limited to the first two classes to maintain sufficiently volatile destruction capability, which will be further explained in chapter 3.

1.2.2 Design of IEDs

As IEDs are improvised by nature, no limitations on their design exist. The essential components consist of a volatile material coupled with a detonator. Generally, their creators seek a material with the most destructive potential to maximize damage. However, IEDs are often composed of whatever explosive material is readily available. Often pipe bombs will be used in the design of IEDs or other normal compact containers. Just as the IED is often shrewdly improvised, the detonation procedure follows analogously; detonation methods include timed detonation, pressure detonation, remote frequency (cell phones or garage door openers) and manual triggering through a direct wire (Schubert, 2006). IEDs may be designed for antipersonnel use, involving small charges and mines, or they may be devised to destroy vehicles, such as ambushing military convoys. As an example, an artillery shell IED is shown in Figure 1.2.

Figure 1.2 Common artillery shell IED design (Inert Explosive Training Products, 2009).

It is also necessary to parameterize the shapes of explosives. IEDs may be very diverse in shape, most commonly existing as sphere, sheet, cylindrical or rectangular shapes. Primarily, sheet explosives are defined as thin explosives spread over a large area, whereas bulk explosives are more compact explosive volumes including spheres, boxes, or cylinders and other compressed shapes. Generally, sheet explosives are less dangerous than bulk explosives, due to their large surface area to volume ratio when compared to bulk explosives which typically creates less pressure during explosions. Therefore, bulk explosives were focused in this report.

1.2.3 Placement of IEDs

As mentioned, IEDs are often cleverly hidden in safe-looking objects including fire extinguishers, briefcases, mail packages and other apparently benign devices (Schubert, 2006; Wilson, 2006). Placement of the IED usually depends on its size and the designer's intent for use. Often IEDs are buried or deployed in car trunks. Vehicle born IEDs (VBIED) generally contain large volumes of bulk explosives rather than simple mines and buried artillery shells. For more effect, often IEDs are coupled or "daisy chained," used in shape charges, or staged in a multilevel ambush on roadways to trap military convoys (Wilson, 2006). Such tactics optimize the destructive power of the IED and are popular choices for many terrorists. Additionally, IEDs may be surrounded by dangerous shrapnel materials, such as nails or small metal parts, causing debilitating fragments to be ejected during an explosion.

CHAPTER 2 - Explosive Detection Techniques

When dealing with IED threats, three common tactics exist for minimizing the threat: prevention, shielding and detection. IED prevention and shielding, though also important defense mechanisms, are not the subject of this thesis, and they will not be considered. Because of the gravity of the threat posed by IEDs in terrorism and warfare, development of an effective detection technique is critical. In general, methods exist for identifying hidden materials, such as explosives and contraband, but identification is a complex and multi-faceted task. Because of the difficulty of the problem and the variety of explosives used, many unique detection techniques have been proposed (see Figure 2.1) and vary in their effectiveness. Before a discussion of detection techniques, it is first important to define the term signature in relation to explosive detection.

- **Signature** - Any characteristic that may be consistently used to differentiate explosive targets from non-explosive or inert targets.

Detection of IEDs may be divided into three groups: non-explosive component detection, trace detection and bulk detection. Non-explosive component detection involves detecting IED parts that are not explosive by nature, for example detonators, shell casing, and unique circuitry. Because detection of non-explosive components of IEDs is not a widely used method due to a high false alarm rate and other problems, it will not be discussed. Secondly, trace detection methods involve seeking microscopic traces, including vapors or small pieces of evidence revealing the presence of an explosive device. Finally, bulk detection methods attempt to detect the macroscopic properties of the explosive device directly, often through imaging or scanning methods as shown in Figure 2.1. The following sections describe specific explosive detection methods in current literature.

2.1 Trace Detection Methods

Trace detection, differing from bulk detection, relies on one of two often difficult to detect signatures: explosive vapor and explosive particulate.

- **Explosive Vapor -** gas-phase molecules emitted from the surface of the explosive when the atmospheric pressure is higher than the vapor pressure of the explosive.

- **Explosive Particulate -** microscopic explosive particles that adhere to any surface that has been in direct or indirect contact with the explosive.

Thus, trace detection methods rely on collection of either of these types of evidence obtained from the explosive sample. Generally speaking, vapor pressures for common explosives as shown in Table 2.1 are known to be small, which makes accurate detection by vapor difficult because of reduced detection efficiency. Air currents are also a detriment to vapor detection systems, limiting their effectiveness in a drafty field environment.

Table 2.1 Vapor pressure for common explosives (Sanchez, et al. 2007).

Explosive	*Class*	*Vapor Pressure (Torr) at 293K*
RDX	Nitramine	5×10^{-9}
HMX	Nitramine	8×10^{-11}
TETRYL	Nitramine	6×10^{-6}
TNG	Nitrate Ester	4×10^{-4}
PETN	Nitrate Ester	1×10^{-8}
TNT	Nitroaromatic	7×10^{-6}

Next, effective particulate detection requires collecting explosive particles. Typically, contact is required with either the explosive surface or something that has come into contact with the explosive; however, this is often not possible. To prevent detection, frequently intentional concealment restricts the vapor and particulates from escaping the explosive container, making detection even more challenging. Fortunately, explosive contaminants are normally difficult to contain completely. Despite the challenges, many trace explosive detection techniques have been investigated and perform satisfactorily in some scenarios.

2.1.1 Electronic or Chemical

Chemiluminescence (CL) – This method of explosive detection uses chemical reactions that produce energy in the form of light, including ultraviolet, visible or infrared (Jimenez and Navas, 2007). In principle, ultraviolet and infrared light can be used for detection; however, observation of visible light (about 400-700 nm wavelength) is most common. Specifically, CL can be used to detect explosives by identifying the reaction of nitric oxide and the ozone:

$$NO + O_3 \rightarrow NO_2^* + O_2 \text{ and } NO_2^* \rightarrow NO_2 + \text{light (IR)}, \quad (2.1)$$

which occurs in nitrogen-rich explosives (Jimenez and Navas, 2004). However, the effectiveness of CL in detection of IEDs is limited. For example, it is primarily restricted to detecting nitrogen-rich explosives and is not selective when identifying the type of explosive (Jimenez and Navas, 2007).

Mass Spectrometry – This method analyzes a substance in relation to the masses of its corresponding atoms. Two primary methods exist for separation and analysis using mass spectrometry: a method based on time separation and a method based on geometric separation (Yinon, 2007). In general, mass spectrometry detects residual traces of explosives in contamination of air, dust etc. Often triple quadrupole mass spectrometers are necessary to monitor mass ratios in reactions by recording data through selected reaction monitoring (SRM). Disadvantages with the method include a minimum trace detection mass of at least 100 pg for TNT, NG, PETN and RDX (Yinon, 2007). Other disadvantages include high expenses, the need for advanced equipment, and lack of portability.

2.1.2 Optical

Infrared (IR) Spectroscopy - Because molecules absorb light at characteristic wavelengths, identifying chemical composition by examining an absorption spectrum is possible. Indeed, IR spectroscopy has been used to find the absorption spectrum from explosive particulates and explosive vapor for detection (Steinfeld and Wormhoudt, 1998). Cavity-ringdown spectroscopy, which uses mid-infrared light, also has been applied for explosive vapor detection. With this method, limits of 75 ppt for TNT and other explosives have been found, which allows for lower limits of detection than many vapor methods (Todd, et al. 2002).

Microcantilevers – Microcantilever detection is a trace detection method that detects particulates using a cantilever, a beam supported only on one end. In basic microcantilever detection, absorption of molecules on the unsupported side of the cantilever causes bending, which may be monitored with high sensitivity (Senesac and Thundat, 2007). Microcantilevers have the potential for detection because of their miniature size, array detection capabilities, high sensitivity and low power consumption (Van Neste, et al. 2008). Additionally, microcantilever explosive detection coupled with photothermal deflection spectroscopy is possible by observing the bend in the microcantilever after absorption of infrared light.

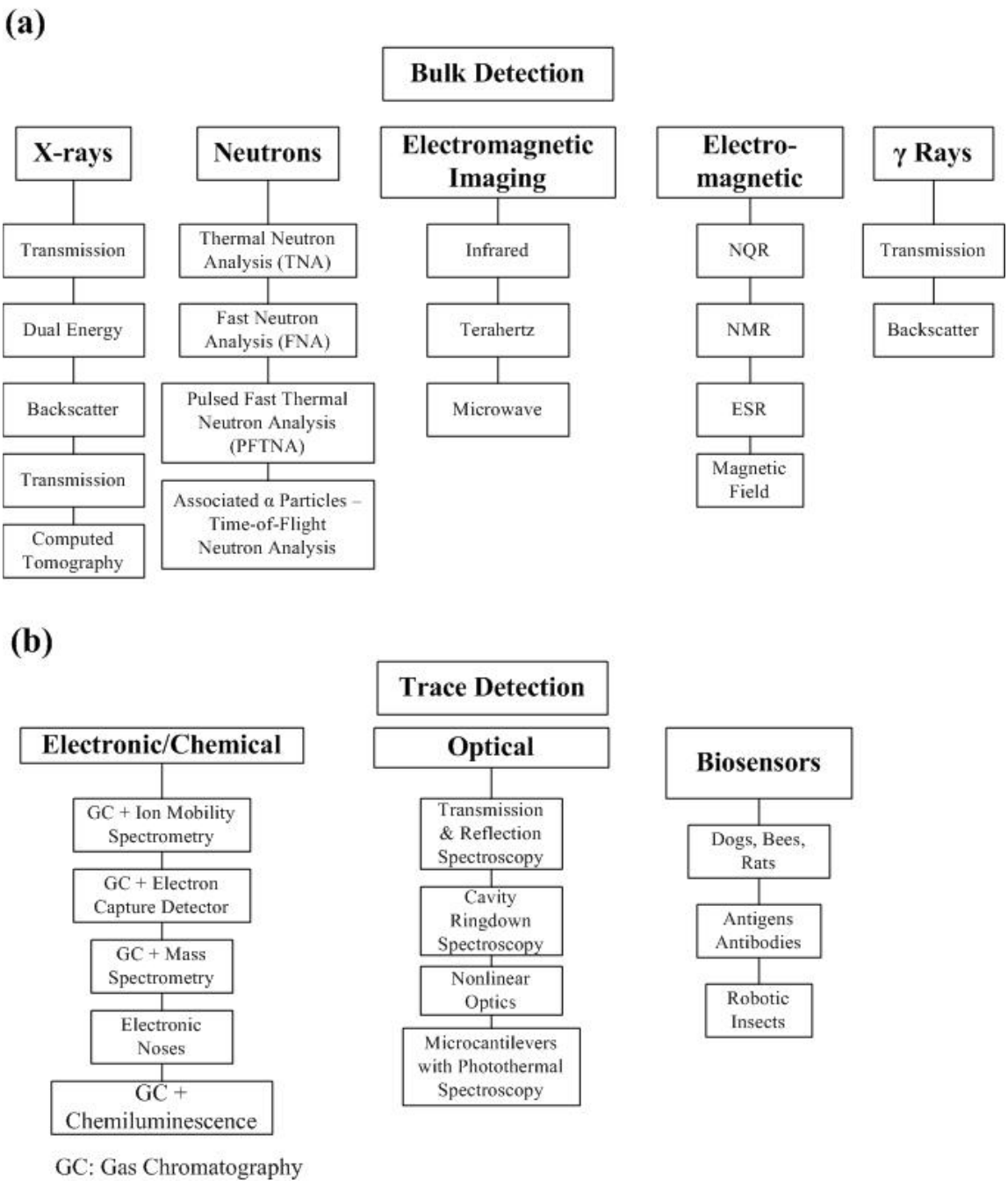

Figure 2.1 Common explosive detection technologies used currently for (a) bulk and (b) trace detection techniques.

2.1.3 Biosensors

Interestingly, it is possible to detect explosives with biosensors. Many biological systems are capable of acting as biosensors including canines, pigs, rats, bees, and microorganisms (Harper and Furton, 2007). Biosensors usually use the sense of smell or olfaction for explosive

detection. Notably, canine detection remains one of the most popular of these methods, mostly because the olfactory abilities of many dogs are exceptional and because dogs are easily trained. Highly sensitive breeds have approximately 1000 times the olfaction ability of a human. They may possess 220 million olfactory receptors compared to 5 million olfactory receptors in a human (Correa, 2005). Furthermore, the training and deployment of canines for explosive detection has been shown to be effective, and over 800 canine teams are in use by U.S. Customs and Border Protection with Homeland Security. Mimicking this capability, microsensors with gas chromatography (GC) called 'electronic noses' have been used as explosive detectors simulating olfaction, but they achieve less selectivity than canines. Bees, which have been studied as potential biological detector systems, have been found to detect explosive odor concentrations below most microsensors and possess an ability comparable to canines. Limitations of biosensors include expensive training, non-continuous operation and sometimes brief operation time, limited by the life-time of the animal.

2.2 Bulk Detection Methods

Given that bulk explosive detection consists of identifying the macroscopic characteristics of explosives, these methods detect explosives with electromagnetic and particle radiation. Currently, explored methods may implement microwave, photon, and neutron techniques. As the radiation must be probing, other types of radiation such as charged particles are ineffective because they cannot adequately penetrate clutter or soil materials. For example, alpha particle radiation cannot even penetrate a sheet of paper and thus is inadequate for shielded IEDs. Primarily, bulk detection methods use three signatures: shape of the IED, density of the IED and composition of the IED. Probing radiation used in bulk detection offers several potential advantages over many trace detection techniques for larger targets, including the following.

- **Greater Specificity** – Fewer false positives or non-explosives are labeled as explosives.
- **Penetrability** – It offers the ability to interrogate larger volumes.
- **Sensitivity** – It has fewer false negatives or explosives labeled as non-explosives.
- **Quick Interrogation** – It offers high intensity that allows rapid scanning.
- **Standoff Interrogation** – Detection from a distance improves operator and equipment safety.

A challenge to bulk detection techniques is sheet-shaped explosives. A cone-shaped beam of radiation will generally interact weakly with thin sheet explosives, because it passes through only a minimal amount of explosive material. Fortunately, as mentioned, they are generally less dangerous than bulk explosives. Several bulk explosive detection techniques are described next.

2.2.1 X-ray/Photon Interrogation

X-ray Transmission – X-ray interrogation provides information primarily about target density. X-ray transmission can be used to form a compound image that varies with the absorption of X rays in materials, which depends on their density and to a small extent on their atomic number. Some or all of the transmitted X rays are then absorbed by a detector, and an image is created. Transmission technology is advanced and is in effect in many airport screening scenarios (Singh, 2003). However, many false positives occur, and the method is not suited to standoff detection. Because explosives may be in any shape, imaging methods do not work well in large cargo volumes containing many diversely shaped types of materials. In small volumes, such as suitcases and small baggage, however, imaging technology is very effective. Additionally, X rays may detect other explosive components including wiring or supplementary mechanisms.

Backscattered X rays – Backscattered X rays can also be used to form radiographs and allow standoff detection. Because of the characteristics of backscattered radiography, it is particularly effective in discriminating against low atomic number and larger than average density materials, such as plastic explosives (Singh, 2003). However, false alarms and explosive shielding is a significant problem with this technique.

Computed Tomography (CT) - CT is an imaging method employing tomography, which allows two-dimensional images to be constructed, having excellent spatial resolution. However, it requires extensive scanning around all or portions of a target. Several methods exist including direct X-ray transmission imaging, coded X-ray scatter imaging, coherent scatter X-ray CT (Harding, 2004), and dual-energy CT. However, the method is ill-suited to standoff detection, because it requires extensive multi-angle scanning and position-sensitive detectors or detector arrays. Additionally, for all X-ray techniques, interpretation is typically required by a user or complex software algorithms, rendering the detection system user intensive or otherwise complex.

2.2.2 Electromagnetic Imaging Methods

Resonant Infrared Photothermal Imaging – This imaging method aims an infrared (IR) laser at a suspect surface and then views the surface through a photothermal imager. Resonant absorption occurs in the explosive particulates at specific IR wavelengths, which is observed using the thermal contrast. This method distinguishes trace explosives with particles as small as 10 μm (Furstenberg, et al. 2008), and is a trace detection method.

Microwave and Millimeter-wave – The use of electromagnetic waves with frequencies in the gigahertz range is valid because this method is a low dose exposure detection method able to penetrate some targets. Microwave and millimeter-wave scanning allow imaging of a target with larger wavelength frequencies generally producing higher resolution images. Microwave scanning may be used for interrogating people and can penetrate clothing. It can operate at standoff distances of 1 m or greater and requires simple, relatively inexpensive scanning equipment (Kuznetsov and Evsenin, 2006). Millimeter waves from 30-300 GHz behave similarly to microwaves for detection purposes. Both frequency ranges can produce images that can be used to identify some explosives (Sheen, et al. 2007). Disadvantages include strong wave attenuation through dense materials causing low penetrability in thick clutter materials. This allows explosives to be concealed. Ultimately, microwave and millimeter-wave scanning is a technique best suited for interrogating people rather than for volume interrogation.

Nuclear Quadrupole Resonance (NQR) – Nuclear quadrupole resonance uses magnetic resonance physics similar to the physics in magnetic resonance imaging (MRI). It operates on the principle that a quadrupole nucleus will align its spin with an electrostatic field. When a specific electric field gradient is applied, the nucleus will flip its electric quadrupole moment, generating a NQR pulse (Garroway, et al. 2001). Thus, NQR permits magnetic resonance without a magnet present. This differs from NMR, which requires a static homogenous magnetic field (Miller, 2007). In particular, NQR has been used to detect plastic explosives containing RDX, PETN, HMX and others (Rudakov, et al. 2006). Also, NQR has been proposed for vehicle screening; however, it is difficult to generate an RF magnetic field of sufficient magnitude for operation in a field environment. NQR also requires close proximity for detection purposes and thus is not a good standoff technique.

2.2.3 Neutron Interrogation Techniques

As will be further explained, most explosives contain similar compositions of hydrogen (H), carbon (C), nitrogen (N) and oxygen (O). Based on this similarity, neutron interrogation methods enable explosive identification from the stoichiometry of a target. Neutrons, because of their charge-less nature, offer a unique method to identify a compounds' composition. Neutrons are not governed by Coulomb's law and interact with nuclei. In one reaction, neutrons interact with the nuclei of the elements irradiated, generating gamma rays through inelastic scattering. Inelastic scattering is an energy de-excitation phenomenon that deals with energy level transitions within nuclei and is explained further in chapter 3. All nuclei possess excited states of higher quantized energy levels, which can be predicted by nuclear physics. This has been experimentally demonstrated, for example, through scattering energetic protons of known momentum off nuclei from an element of interest and measuring the scatter angles and final momenta of the protons. However, excited states of nuclei are not stable, and decay most prominently through gamma emission, the gamma rays having discrete energies characteristic of the changes in energy states. Each element may be identified by its specific set of inelastic-scatter gamma-ray energies, produced by high-energy neutrons. Frequently, many of these gamma-ray energies are not shared by other commonly existing elements in nature, making them distinct. Therefore characterization of neutron irradiated explosives is possible for explosives containing H, C, N, and O, by detection of gamma rays of the specific gamma-ray energies emitted from those elements. Thus, neutron interrogation presents signatures for identifying the composition of an explosive target. It remains to be determined which bulk method may be most useful for this type of detection. While X-ray and other bulk imaging methods are useful, as described, an IED is not limited to a specific shape. This limits the potential for detection based on imaging. Therefore, explosive shape when used as a signature is useful but not unique. Additionally, transmitted and scattered X-ray intensities are primarily affected by density and only minimally affected by composition. Thus, neutrons offer the following distinct advantages over many other bulk explosive detection methods.

- **Stoichiometric Identification** – Energy signatures may be used to identify the elemental composition, not only the density and approximate atomic number, as in X-ray methods.

- **Greater Penetrability** – While X rays do have good penetration in low Z materials, high-energy neutrons penetrate low and high Z materials such as iron, reducing the shielding effects of explosive shielding (see Table 2.2).

A challenge of neutron techniques is that they are inadequate for screening people because of the dose delivered. However, in screening cargo or other inert targets, they are useful as long as activation is kept to acceptable levels. Predominant neutron interrogation methods are summarized in the following paragraphs.

Table 2.2 Material thicknesses needed to attenuate both neutron and photon beams to 0.1% of the incident flux (Runkle, 2009).

	Attenuation Length (cm)			
Photon Beam	*Semtex-H*	*Machine Parts*	*Magazines*	*Electronics*
200 keV	35	5.1	62	120
1.2/1.3 MeV (^{60}Co)	81	17	140	516
2 MeV brems.	64	13	113	430
6 MeV brems.	110	21	200	680
Neutron Beam				
Thermal	6.3	5.4	5.8	5.7
D-D (2.45 MeV)	52	24	54	340
D-T (14.1 MeV)	110	53	170	1000

Thermal Neutron Analysis (TNA) – One of the first neutron interrogation techniques was TNA. This technique, which uses thermal neutrons with a most probable energy of approximately 0.0253 eV at room temperature, involves absorption of the neutron in the (n, γ) reaction. Both prompt and delayed gamma rays emitted from the reaction may be measured. One reason TNA has often been preferred is because the cross sections for thermal neutron absorption are much higher than for fast neutrons (Buffler, 2004; Hussein and Waller, 1998; Lanza, 2007). A drawback of TNA is that it is difficult to manufacture a portable intense source of thermal neutrons. A common source of thermal neutrons is reactor beam ports.

Fast Neutron Analysis (FNA) – In this method, gamma rays are detected after emission from a target isotope following (n, n'γ) reactions (Hussein and Waller, 1998; Lanza, 2007). Because fast neutrons are readily available in isotope or generator sources, this is a practical method.

Additionally, fast neutrons are attenuated less in an object than thermal neutrons, permitting better neutron imaging. FNA seeks the inelastic-scatter gamma rays generated from fast neutron interrogation of elements H, C, N, and O. Usually a detector with high resolution and good efficiency, such as a high purity germanium (HPGe) detector, is used with the technique.

Pulsed Fast Neutron Analysis (PFNA) – Similar to FNA, PFNA uses fast neutrons in the (n, n'γ) reaction to generate inelastic-scatter gamma rays, but the neutrons are emitted in multiple nanosecond pulses (Lanza, 2007). Detection methods are similar to FNA, and HPGe detectors are often used. The method may also identify the location of the inelastic-scatter gamma-ray emission voxel from a comparison of neutron generation and gamma-ray emission timing.

Pulsed Fast and Thermal Neutron Analysis (PFTNA) – In this method of scanning, the target is interrogated with alternating pulsed fast and thermal neutron beams to identify its composition. The reactions (n,n'γ), (n,p γ) and (n,γ) are used to identify the elemental composition (Vourvopoulos and Womble, 2001). The method has the advantage of being portable and being able to measure neutron information like TNA, but it is also able to measure fast neutron reactions, yielding more information than TNA and PFNA. It does have a slower, 10-ms pulse time versus a 2-ns pulse time capable in PFNA (Singh, 2003). Often, the source of the neutron beam is a neutron generator, either utilizing the reaction involving deuterium-deuterium (D-D) or the reaction of deuterium-tritium (D-T) for neutron generation.

Nanosecond Neutron Analysis/ Associated Particles Technique (NNA/APT) – In this method, inelastic-scatter gamma rays are measured following fast D-T neutron interrogation (Lanza, 2007; Tourneur, 2007). The D(T,α)n reaction produces an alpha particle emitted in the direction opposite to that of the neutron. Detection of the alpha (associated particle) can be used to determine the time and, if position sensitive detectors are used, the direction of the emitted neutron (Buffler, 2004). Gamma-ray detection is often achieved through use of NaI or BGO detectors. The alpha particle is detected at the time of neutron generation, and the neutron is time tagged. This allows for imaging of a target based on the time the gamma ray is received, which indicates the depth in the target at which the gamma ray was emitted.

2.3 Neutron Generator Sources

Neutron generator techniques have in the past been tried and not implemented, due to several discouraging factors (Hussein and Waller, 1998; Lacey, 2007). Previously, neutron

generators were difficult to obtain, operate and afford. Secondly, the technology was premature and needed refining. Also, past neutron generators were large and had short operation lifetimes. Finally, properly shielding a high energy portable neutron source is a challenging task to maintain the safety of both operators and bystanders.

While the latter problems are not trivial, they are not insurmountable because commercial neutron generator technology has evolved considerably. Additionally, as described, no current method of detection has the penetration and potential of neutrons for interrogation of bulk targets and shielded explosives. Therefore, it is worthy of investigation. Currently, commercial neutron generators are rising in availability. The technology has a much longer operation lifetime and some models operate with a much higher flux than previously possible, approaching 10^{10} n s^{-1} or higher (Yoshikawa, et al. 2007; Adelphi, 2005). This will allow for more rapid and deeper probing interrogation. Not only are current neutron generators powerful, but they are also compact, sometimes as small as a few cubic feet in size (see Figure 2.2), and portable.

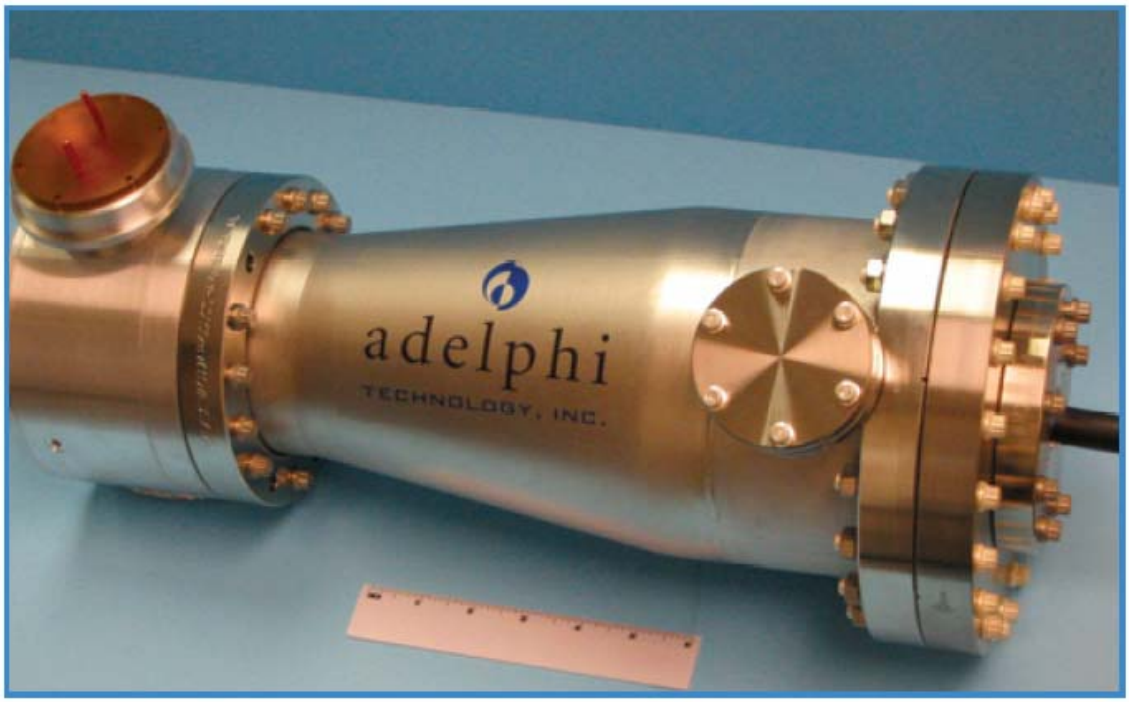

Figure 2.2 Adelphi's compact RF-plasma D-D 2.5-MeV neutron generator, capable of emitting 10^{10} n s^{-1} (Adelphi, 2005).

Two main types of neutron generators currently exist. Using the $^{2}H(d,n)^{3}He$ reaction, neutrons may be generated at an energy of 2.5 MeV with a D-D generator. Secondly, 14.1-MeV neutrons are produced with the $^{2}H(t,n)^{4}He$ reaction with a D-T generator. Because they may be

pulsed instead of used continuously, adequate shielding is achievable if properly designed, allowing operation in an urban environment. As mentioned, neutrons are not suited to human interrogation, but bulk target scanning is a feasible application. A hybrid approach is suggested by Runkle, in which a combination of neutrons producing gamma rays coupled with neutron counters and photon methods may be an effective approach. Finally, costly equipment is an unavoidable problem with all techniques for bulk detection (Runkle, et al. 2009).

2.4 IED Checking Systems

Two main types of IED detection systems are commonly in use: stationary systems and mobile systems. Stationary systems are only capable of interrogation at fixed locations, while mobile systems may be transported. Each type may operate either close to a target (operator and equipment), remotely (in which equipment is near the target but the operator is not) or as a standoff detection system (in which both operator and equipment are a distance from the target). Standoff systems are generally considered to be one-sided systems, in which all of the detection and scanning equipment is on the same side of the target. Some scenarios, such as airport or fixed explosive checkpoint stations, use stationary systems and may use standoff or remote detection. One such system using remote detection uses a D-T neutron generator coupled with HPGe detectors and is capable of vehicle scanning for IEDs (Koltick, et al. 2007). The system also has a GUI in place, which facilitates effective equipment operation. While this method may work for a checkpoint station, it does not function as a standoff technology, and it is large and costly. Another important part of an explosive interrogation system is the level of automation. Detection systems requiring extensive technical expertise to operate are not feasible for general use. Ideally, an optimal explosive detection system for a field environment would be feasible to produce, mobile, operable at standoff, and highly automated, requiring minimal user inputs.

2.5 Goal Statement and Research Summary

The explosive detection approach suggested in this thesis would operate with a portable D-T neutron generator, using fast and thermal neutron analysis for interrogation in eventual symbiosis with a photon interrogation method and neutron detectors. The research applies a signature-based radiation scanning (SBRS) approach that incorporates figures-of-merit. The thesis only investigates the neutron-induced gamma-ray portion of SBRS through simulations.

The objective of the research contained in the thesis was twofold. The first objective was to simulate shielding and collimation to produce appropriate neutron beams for interrogation purposes in a field environment from a 14.1-MeV isotropic point neutron source. Both a beam collimating source vault and a beam catcher were designed within this research.

The second and primary objective was to establish some bounds on how well beams of neutrons can be used to distinguish, at stand-off distances of up to a few meters, nitrogen-rich explosive materials from inert materials when these materials are hidden within small targets. The use of parallel neutron beams from californium-252 (^{252}Cf) and 14.1-MeV neutron generators was investigated for the utility of explosive identification using a template-matching technique. Simulations involved a variety of explosive and inert materials in various target configurations. The primary tool used was Monte Carlo simulation with the MCNP5 code. The use of neutron induced gamma-ray responses from the elements H, C, N and O for explosive detection was explored through simulations. An attempt was made to find the optimum prompt-capture and inelastic-scatter characteristic gamma-ray signature energies for nitrogen-rich explosive identification. A particular objective was to determine ways to minimize the effects of shielding materials called "clutter," or inert materials placed around or near an explosive sample within a target. The potential of using "average" templates, i.e., templates made from the average composition of nitrogen-rich explosives, or templates that represented an average response from a range of explosive materials or explosive materials with inert clutter materials, was considered. The use of responses from "artificial templates," or templates containing specific concentrations and densities of clutter materials was tested. Methods of organizing clutter materials into groups based on features such as density and atomic number were explored. A method that incorporated a tiered or multiple stage filter process was investigated. An effort was made to identify the minimum number of templates needed to distinguish nitrogen-rich explosives from inert targets in particular geometrical configurations that may incorporate clutter.

CHAPTER 3 - Theory

3.1 Elements of Neutron Physics

Although some elements of neutron physics have been explained in the previous section, a more in-depth explanation may be helpful. Neutrons are neutral, and they interact primarily with the nuclei of atoms, not with their electrons. Additionally, the nuclear forces that are involved in many neutron-nuclei interactions within matter interact at a very short range between neutrons and nucleons. Therefore, neutrons must pass near the nucleus of an atom for an interaction to occur. Because the size of a nucleus is small relative to the size of an atom, neutrons can travel considerable distances in matter. In contrast, X rays interact with electrons in a target. The kinetic energy of neutrons has a strong effect upon their behavior. Neutrons are generally divided into three groups according to their energy, consisting of thermal (< 0.2 eV), epithermal (0.2 eV < E < 0.1 MeV) and fast (> 0.1 MeV). Neutrons interact with matter in four primary ways.

1) **Neutron Capture** – Occurs when a neutron is captured or absorbed by an atomic nucleus to form a heavier nucleus. The interaction is of the form ${}^{A}\mathrm{X}(\mathrm{n},\gamma){}^{A+1}\mathrm{X}$, where the heavier nucleus de-excites through emission of one or more prompt, and in some cases delayed, gamma rays. Cross sections for neutron capture are high for thermal neutrons, lower for epithermal neutrons and very low for fast neutrons, and often are inversely proportional to $\sqrt{E}$, where E is neutron energy, over a large neutron energy range.
2) **Nuclear Reactions** – Are processes in which a neutron collides with a nucleus to form a new nucleus, which de-excites by emission of particles. Examples include reactions such as ${}^{A}_{Z}\mathrm{X}(\mathrm{n},\mathrm{p}){}^{A}_{Z-1}\mathrm{Y}$, ${}^{A}_{Z}\mathrm{X}(\mathrm{n},2\mathrm{n}){}^{A-1}_{Z}\mathrm{X}$, and ${}^{A}_{Z}\mathrm{X}(\mathrm{n},\alpha){}^{A-4}_{Z-2}\mathrm{Y}$. A variety of particles may be produced during nuclear reactions and delayed gamma rays often are emitted to make the nucleus energetically stable. Thermal, epithermal, and fast neutrons may all cause nuclear reactions.
3) **Elastic Scattering** – Occurs when a neutron scatters or collides with a nucleus, transferring some of its kinetic energy to kinetic energy of the nucleus, but not leaving the nucleus in an excited state. Elastic scattering conserves kinetic energy. The elastic scattering cross section is fairly constant with energy.

4) **Inelastic Scattering** – Is a scattering reaction that does not conserve kinetic energy. Instead, some of the neutron's kinetic energy is given to the nucleus, exciting it. The nucleus then de-excites via emission of a inelastic-scatter gamma ray. The reaction is of the type X(n, n'γ)X. Only neutrons above a threshold energy for a particular isotope may scatter inelastically.

3.2 Explosive Composition

In general explosive detection, two classes of materials exist: explosives (or explosive surrogates), and inert (or non-explosive) materials. Inert materials may be used for explosive shielding. Explosives encompass a broad category of energetically or chemically unstable substances. As mentioned in the introduction, three fundamental groups of prevalently used explosives exist: military explosives, industrial explosives and other unstable compounds (often improvised). Additionally, explosives may be categorized by their burning rate. Primary explosives, also called low explosives (LE) tend to burn rapidly, or deflagrate. Secondary explosives, also called high explosives (HE), detonate and burn in millionths of a second. HE create much more pressure than LE when burning, resulting in stronger explosions. Most military and industrial explosives are HE, but commercially available unstable compounds may be of either type. Figure 3.1 shows more completely the various categories of explosive substances. Propellants, though dangerous, are not considered in this thesis because they are

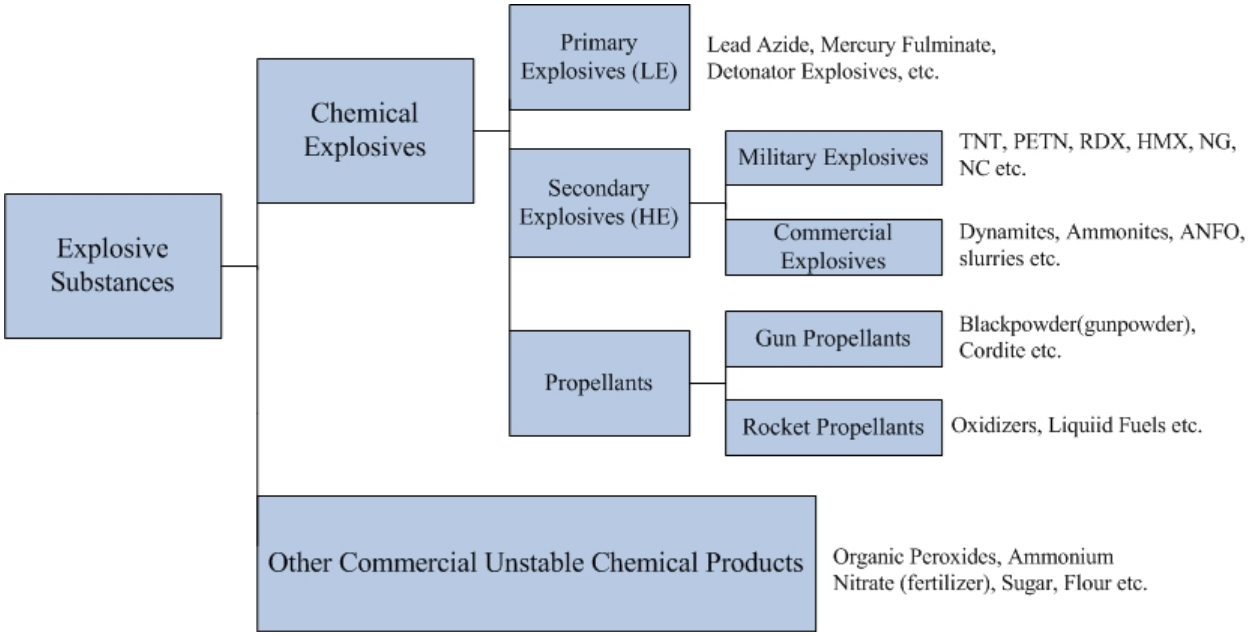

Figure 3.1 Explosive classification by substance.

much less dangerous than HE. Clearly, any type of explosive can be used in an act of war or terror, but HE are the preferred form for terrorists.

Chemically, explosives must include both oxidizing and reducing agents. Because strong oxidizers are very electronegative, explosives generally contain either nitrogen, oxygen, fluorine or chlorine. Fluorine and chlorine are both expensive and often too unstable to use practically for explosive manufacturing. Thus, most current HE contain large ratios of oxygen and nitrogen (National Research Council, 2004). Typically, hydrogen, carbon or other light elements are the reducing agents present in HE. Explosives containing large percentages of nitrogen are referred to as nitrogen-rich explosives. These explosives use inorganic or organic nitrate or nitro functional groups as the oxidant. Many of these nitrogen-rich explosives contain similar compositions, having been found to be approximately 3% H, 20% C, 31% N, and 46% O (National Research Council, 2004). Additionally, densities of explosives are generally > 50% higher than densities of common HCNO compounds (Dunn, 2007b). Buffler (2004) demonstrates that the HCNO composition of explosives is much different than that of many other HCNO containing materials. Specifically, Buffler lists ten nitrogen-rich explosives, 5 HCNO containing illicit drugs and 22 common HCNO materials (Buffler, 2004). The N and O atom fractions for the nitrogen-rich explosives are significantly higher than the N and O atom fractions present in either the illicit drugs or the HCNO containing inert materials shown (Buffler, 2004). This suggests that nitrogen-rich explosives have characteristics that differentiate them from most other ordinary HCNO containing materials. Furthermore, the partial density of O in explosives is higher than the partial density of C. Therefore, nitrogen-rich explosives may be differentiated from other materials that naturally contain nitrogen (see Figure 3.2) by utilizing ratios of the elements C, N and O. A strong case may then be made to apply this theory to differentiate nitrogen-rich explosives.

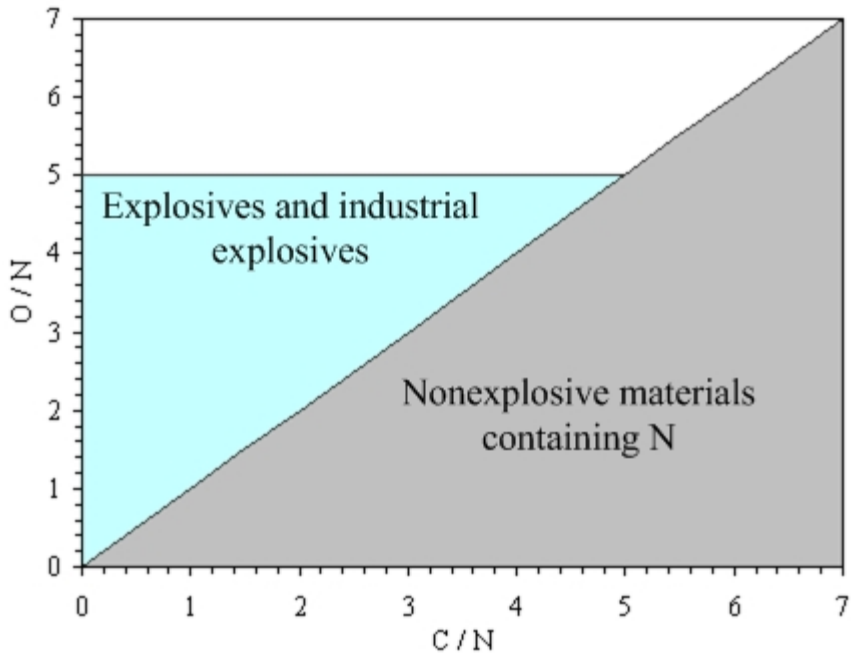

Figure 3.2 Ratios between partial densities of oxygen and carbon with nitrogen for various explosive and non-explosive materials (Kuznetsov, et al. 2006).

Within the bounds of this thesis, only nitrogen-rich explosives were considered. Thus, an inert material is defined as any material that is not a nitrogen-rich explosive. Therefore, it is important to note that while inert materials may not be intrinsically safe materials; they are, however, not nitrogen-rich explosives. The following section describes a method that capitalizes on the characteristics of nitrogen-rich explosives to differentiate them from inert materials.

3.3 Template Matching Procedure

Inelastic-scatter and prompt-capture gamma-ray signatures in principle can be used to identify nitrogen-rich explosives. Because these explosives may be distinctly categorized by their HCNO concentration, it is possible to develop templates using characteristic gamma-ray responses generated through neutron interrogation of those elements. By examining the excitation states for HCNO, many inelastic-scatter and prompt-capture gamma-rays have been identified. Table 3.1 lists 25 candidate signature energies identified for the utility of explosive detection. Only gamma-ray energies from interactions with significantly large cross sections are

Table 3.1 25 Candidate HCNO prompt-capture and inelastic-scatter signature energies (Group T-16, 98-2007; Molnar, 2004).

Element	*Energy (MeV)*	*Type of Reaction*	*Thermal σ (barns)*	*14.1-MeV σ (barns)*
Hydrogen	2.2232	Hydrogen prompt-capture	0.3326	-
Carbon	1.2618	Carbon prompt-capture	0.00124	-
	3.6839	Carbon prompt-capture	0.00122	-
	4.4390	Carbon inelastic-scatter	-	0.2106
	4.9453	Carbon prompt-capture	0.00261	-
Nitrogen	0.7284	Nitrogen inelastic-scatter	-	0.0206
	1.6353	Nitrogen inelastic-scatter	-	0.0228
	1.8848	Nitrogen prompt-capture	0.01470	-
	2.3128	Nitrogen inelastic-scatter	-	0.0557
	2.7931	Nitrogen inelastic-scatter	-	0.0106
	3.3786	Nitrogen inelastic-scatter	-	0.0109
	3.8907	Nitrogen inelastic-scatter	-	0.00354
	4.9151	Nitrogen inelastic-scatter	-	0.00687
	5.1059	Nitrogen inelastic-scatter	-	0.0437
	5.2692	Nitrogen prompt-capture	0.0236	-
	6.4462	Nitrogen inelastic-scatter	-	0.0122
	7.0291	Nitrogen inelastic-scatter	-	0.0242
	10.8291	Nitrogen prompt-capture	0.01068575	-
Oxygen	0.8707	Oxygen prompt-capture	0.00019	-
	1.0879	Oxygen prompt-capture	0.000155	-
	2.1845	Oxygen prompt-capture	0.000155	-
	2.7420	Oxygen inelastic-scatter	-	0.0433
	6.1299	Oxygen inelastic-scatter	-	0.144
	6.9171	Oxygen inelastic-scatter	-	0.0317
	7.1168	Oxygen inelastic-scatter	-	0.0625

listed in Table 3.1. First, gamma rays emitted by H, C, N, or O with the largest prompt-capture cross sections were selected for each element (Molnar, 2004). Next, inelastic-scatter gamma rays were selected, requiring cross sections to exceed 0.003 barns from interrogation by neutrons with energy 14.1 MeV (Group T-16, 98-2007). An effort was made to select several prompt-capture and several inelastic-scatter gamma rays for each element. Chapter 5 examines the utility of the signature energies shown in Table 3.1 for explosive detection.

Using the signature energies in Table 3.1 to form a predicted response from a target, it is possible to develop templates to represent many plausible target scenarios. A library of templates may be compiled based upon characteristic responses of HCNO containing nitrogen-rich explosives, giving rise to what is called signature-based radiation scanning (SBRS). SBRS is an implementation of a template matching procedure. It makes use of a template library, representing targets containing nitrogen-rich explosives in various geometries and in the presence of various clutter materials. Initially, an unknown target is interrogated with a neutron beam. Then, SBRS calculates figures-of-merit and their variances from an unknown target, which will be further described, and a template library derived from known targets. SBRS is a robust technique for explosive-inert differentiation. The template matching approach requires minimal user interaction, differentiating it from most techniques. Thus, the SBRS method offers much promise by providing an automated method for identifying IEDs. If this method is feasible, it will enable a considerable range of targets to be identified through neutron interrogation. The method should be field applicable for various IED containers, including briefcases, buried mines, vehicles and bulk cargo containers.

3.4 Template Generation Procedure for SBRS

It is assumed that for any given target type, a finite maximum of L templates will be able to represent it adequately. Let a template $\mathbf{S}_\ell$ be a vector of N signatures for a target that contains a known explosive sample, where the subscript ℓ indicates a particular target configuration (position of sample in the target, amount and distribution of clutter, etc.) out of a total of L configurations, i.e.,

$$\mathbf{S}_\ell = \left(S_{\ell 1}\ S_{\ell 2}\ \ldots\ S_{\ell N}\right),\ \ell = 1,2,\ldots,L\,. \tag{3.1}$$

After an appropriate number of templates is generated for a specific target type, an unknown

target of the same type is interrogated; this results in the generation of a response vector, **R.** Let **R** be a vector of the same *N* signatures for the test target, i.e.

$$\mathbf{R} = \left(R_1 \; R_2 \; \ldots \; R_N \right). \tag{3.2}$$

The response vector will then be compared to the library of *L* templates for the corresponding target type using a figure-of-merit (FOM) procedure described in the next section. A computer code is used to calculate figures-of-merit from the vectors $\mathbf{S}_\ell$ and **R**, explained below, for unknown targets. Table 3.2 demonstrates a sample template with *N* signatures and *N* standard deviations given by σ.

Table 3.2 Sample template format for case ℓ =1.

Signature Energy 1
S_1
σ_1
.
.
.
Signature Energy N
S_N
σ_N

The number of templates generated depends intimately on the specificity desired for explosive identification and on the characteristics or level of complexity of the target. For example, identifying large-volume explosives in a briefcase will require far fewer templates than will be needed to identify a small anti-personnel mine hidden in a car trunk with thick shielding. Clearly, important factors such as intensity of the beam, interrogation time, volume of explosive, thickness of the target, density of the target and distance of the target must all be considered.

Although theoretically infinite possibilities for template generation exist, it is assumed that a finite universe of templates may prove sufficient. The basis for this assumption relies on the ability for one template to match a group of closely related types of explosive target scenarios. First, it is not critical for an unknown explosive target to match a template perfectly. Thus, a finite number of templates may be generated that approximately represents a broad range of explosive target types. One of these templates should identify several explosive targets that are similar, but not identical to it. If this is possible, a finite number of templates may be enough to identify many IEDs. It will be demonstrated that it is possible to minimize the number of templates through a process of discretizing target composition and density. Also, it will be shown

that a tiered process can eliminate the majority of inert targets quickly. For example, nitrogen is rarely present in significant proportions in most inert materials. If the figures-of-merit for nitrogen are checked first, it is possible to eliminate many inert samples very rapidly. Further explanation of grouping techniques and their effectiveness appears later in the thesis.

3.5 Figure-of-merit Analysis Technique

The SBRS method (Dunn, et al. 2007a; Dunn, et al. 2007b) is an implementation of a template matching procedure. It involves calculating a figure-of-merit, ζ, from responses, called signatures, and their variances obtained from a test target. Define the figure-of-merit as

$$\zeta_\ell = \sum_{i=1}^{N} \alpha_i \frac{\left(\beta R_i - S_{\ell i}\right)^2}{\sigma^2\left(\beta R_i\right) + \sigma^2\left(S_{\ell i}\right)}, \tag{3.3}$$

where R_i is the response of the i^{th} signature from an unknown sample and $S_{\ell i}$ is the i^{th} signature from the ℓ^{th} template, N is the number of signatures, β is a factor that scales the measured response values to relate to the template values, σ^2 is the variance, and α_i is a weight factor, which is normalized and given by

$$\alpha_i = \frac{w_i}{\sum_{i=1}^{N} w_i}, \tag{3.4}$$

with $w_i \geq 0$ a relative weight assigned to the i^{th} signature. The standard deviation of the figure-of-merit may be estimated as

$$\sigma\left(\zeta_\ell\right) = 2\left[\sum_{i=1}^{N} \alpha_i^{\,2} \frac{\left(\beta R_i - S_{\ell i}\right)^2}{\beta^2\sigma^2\left(R_i\right) + \sigma^2\left(S_{\ell i}\right)}\right]^{1/2}. \tag{3.5}$$

If there is a close match between a template and a response, the figure-of-merit is small, while for poor matches, the figure-of-merit is much larger. Thus, in principle, an IED should have a small figure-of-merit and an inert target a large figure-of-merit. To prevent misidentification of targets, it is helpful to specify a margin of error. For this purpose, filter functions, $f_\pm$, are introduced

$$f_\pm(\lambda, \ell) = \zeta_\ell \pm \lambda\sigma(\zeta_\ell), \tag{3.6}$$

where λ is a parameter that can be used to adjust the false positive and false negative rates. The filter functions, $f_{\pm}$, ensure the value of the FOM will be sufficiently above or below a cutoff FOM value, f_o, which will be determined experimentally. Thus, the method will establish the specificity for screening suspect targets. If $f_{-}(\lambda) > f_o$, a suspect target is deemed inert within a confidence level determined by λ. However, if $f_{+}(\lambda) \leq f_o$, a suspect target is labeled as an explosive. If neither premise holds true, the test is deemed inconclusive. A false positive indicates an inert material labeled as an explosive and a false negative indicates an explosive labeled as an inert. The specificity is related to the false positive rate through

$$\text{Specificity} = \frac{\text{number of True Negatives}}{\text{number of True Negatives + number of False Positives}}, \tag{3.7}$$

and the sensitivity is related to the false negative rate through

$$\text{Sensitivity} = \frac{\text{number of True Positives}}{\text{number of True Positives + number of False Negatives}}. \tag{3.8}$$

These are manipulated by adjusting either f_o or λ, or both. In equation, (3.7), a specificity of 100% indicates no false positives, and in equation (3.8), a sensitivity of 100% indicates no false negatives. In explosive detection both high specificity and high sensitivity are sought.

In all simulations and analyses performed except for those reported in section 5.3.3, β=1 was used. Also, unit weight factors for each signature energy were generally used. However, simulations often did not incorporate the full list of signature energies, which implied weight factors of zero for absent signature energies.

A sufficient number of templates is necessary to ensure small figures-of-merit for IEDs in a variety of configurations. However, to minimize inert targets fitting a template through chance, it is important to minimize the number templates. Thus, a balance exists between achieving low false positives and low false negatives. Clearly, a foremost objective is to minimize false negatives and produce a technology ensuring high specificity. However, it is acceptable to have a specificity less than 100%, because some false positives are permissible. Furthermore, identification of other materials, including contraband or peroxide based explosives, may be possible with this technique.

3.6 MCNP Code for Simulation

MCNP, standing for Monte Carlo N-Particle, is a particle transport code developed at the Los Alamos National Laboratory (LANL). MCNP has been evolving since its introduction during the cold war. The code is able to simulate neutron, photon, electron or coupled particle transport. Of particularly interest, it is capable of transporting neutrons of energies 0 to 20 MeV. When using the MCNP code, the user creates what is known as the input file. Thus, a simulated experiment is designed by creating an appropriate input file and running it in the MCNP5 code. The input file is a collection of 'cards' specifying information about particular parts of the simulated experiment. A title card, cell cards, surface cards and data cards are used to specify the desired geometry specifications, sources, materials and tally information. An example input file may be found in Appendix G.

The code allows ray tracing by means of complex algorithms through user-defined geometries. Specifically, one may use the code to generate three-dimensional material geometries in what are defined as cells bounded by surfaces **(**X-5 Monte Carlo Team, 2003). The user specifies the cell boundaries by using surfaces and selects a side of the surface to contain the cell. This is decided by using a "+" to denote the outside of the surface and a "-"to denote the inside of the surface to define a cell. In this fashion, the user may specify a small universe in which certain geometries defined by multiple cells exist, along with a source and detectors. Because the code is a powerful modeling tool, enabling complex geometrical configurations to be modeled, it was used to model various target configurations to test the feasibility of the SBRS method and to model shielding for a 14.1-MeV neutron source.

After the geometry is modeled, the user employs material cards to define materials that occupy cells. A material card specifies elements contained in a cell by their ZAID number, which is a three digit Z and a three digit A number followed by a cross section specification. For example, ^{16}O may be specified, 8016.74c where .74c refers to the ENDF/V-BI cross section file. Initial simulations used cross section files of .50c (older cross section data) and more recent simulations used .66c and .74c cross section files. The code incorporates a regularly updated library of the ENDF/V-BI cross sections for neutrons and other particles based on experimental databases.

The code also allows complex source and tally conditions to be specified. Several different distributions may define the source particle energy including a Maxwellian distribution

and a Watt distribution (the sources used in the simulations are described in chapters 4 and 5). MCNP uses estimators, referred to as tallies, to calculate and score radiation events. A tally scores events similar to an actual detector with perfect efficiency. Typically, for experiments, the tally F5 was used. In this tally, an interaction was scored and sorted according to binned energy. The tally F5 measures the fluence

$$\Phi \equiv \lim_{\Delta A \to 0} \frac{\Delta N_p}{\Delta A} = \frac{dN_p}{dA}, \tag{3.9}$$

which has units cm^{-2}, where ΔA is the cross-sectional area of a sphere and N_p is the expected number of particles entering that sphere in some time interval. In general, when modeling the interactions of neutrons with matter, either the diffusion equation or the neutron transport equation (NTE) must be solved. Because the NTE is more accurate than the diffusion equation, a solution to it is preferred. The MCNP code uses complex transport methods to trace the path of a neutron from a source to a detector. The NTE is one form of the more general Boltzmann transport equation that very accurately models the transport of particles. The steady state NTE equation can be written in the form

$$\begin{aligned} &\Omega \bullet \nabla \varphi(\mathbf{r}, E, \Omega) + \Sigma_t(\mathbf{r}) \varphi(\mathbf{r}, E, \Omega) = \\ &\frac{1}{2\pi} \int_0^{2\pi} \int_{-1}^{1} \int_0^{\infty} \Sigma_s(\mathbf{r}, E', \Omega') f_E(E' \to E) f_\omega(\omega_s) \varphi(\mathbf{r}, E', \Omega') dE' d\omega_s d\psi' . \\ &+ s(\mathbf{r}, E, \Omega) \end{aligned} \tag{3.10}$$

In this equation, φ is the flux density as a function of position, **r**, energy, E, and angular direction, Ω; Σ_s is the macroscopic total scattering cross section; s is the source term; and f_E and f_ω are probability density functions where $\omega_s = \cos\theta_s$ and θ_s is the scattering angle.

As the name suggests, MCNP employs Monte Carlo methodology. Monte Carlo is a numerical procedure different than standard deterministic methods. Deterministic methods, such as discrete ordnances, generally develop approximate solutions to the transport equation. Monte Carlo solves the transport equation by tracing many individual particle histories and then averaging these histories to find the average behavior. The uncertainty in the result can be estimated using the central limit theorem **(**X-5 Monte Carlo Team, 2003). In particular, the Monte Carlo method describes a random statistical sampling process based on random number sampling that is used for solving problems numerically. The name "Monte Carlo" is derived from random number sampling, similar in comparison to throwing dice at a casino. Many

random number generators exist and work well for the Monte Carlo method. Generally, due to the large number of histories needed for adequate application of the central limit theorem, powerful computers are used when running the code. Fortunately, current processor speed and computer technology are sufficient to use the Monte Carlo method for solving the transport equation. If Moore's law holds, computer technology should continue to become even faster in the future, allowing for an increased number of histories. A large number is imperative for assisting with variance reduction. This is a crucial aspect of the precision of simulated experiments. However, the accuracy of the simulated experiments depends on the nuclear physics theory supporting the code and the accuracy of the cross section data used. Because the MCNP5 code is thoroughly tested and was developed at Los Alamos by professionals, it is assumed to be an accurate code and is often used in the design of nuclear reactors and other systems. Therefore, given that the code is both accurate and precise, it is theoretically possible to test the feasibility of neutron interrogation for explosive detection through simulation.

3.7 Data Analysis Techniques

To facilitate data analysis, often control scripts were used with the Perl language. Perl scripts were used in two ways. Primarily, Perl scripts were used in post-processing the MCNP output data files. With regular expressions and other features contained in Perl, it is possible to expediently and accurately process large amounts of text data for analysis. The regular expression function allows a user to search through a text file for a critical line of text and then extract data into variables typically stored in arrays in the script. Secondly, Perl scripts were used to generate MCNP input files and print them to a file. This was possible because a constant geometry was used in many input files, and thus the Perl script altered only the material cards and density via loops affecting both the ZAID numbers and their atomic fractions.

For the project, typically simulations with acceptable variance levels may be performed on a personal computer within a feasible time period. When histories are increased, it is more ideal to perform many simulations or more complex simulations with processors in parallel. Thus, to facilitate multiple simulations, a cluster of computers, consisting of several nodal processors called Hydra, was harnessed to increase the speed of simulations. This powerful system used up to 40 processors in parallel, allowing for an increased complexity, number of histories and number of simulations.

Through computer simulations and data processing methods, it is possible to simulate many situations at a much faster rate than would be possible to test experimentally. Hence, to test an expensive and complicated technique, simulations using the MCNP code save both time and resources. Ultimately, however, even a method exhibiting simulated excellence should be experimentally verified.

CHAPTER 4 - Shielding and Collimation Simulations

As mentioned in the goal statement, this research performed two main types of simulations. First, a series of simulations for shielding and collimating beams of neutrons for a D-T 14.1-MeV neutron source for the experimental portion of the SBRS project was performed. This work involved treating the D-T neutron generator as an isotropic point neutron source and then estimating both the collimation of the beam and the dose rates at different locations of the experimental laboratory. These simulations are considered in this chapter.

Secondly, simulations were performed in which parallel disk sources of ^{252}Cf and 14.1-MeV neutron beams were incident on actual targets in various configurations. These were representative of ideal experimental collimated beams that would be used for actual interrogations. The objective of these simulations was to determine the effectiveness of the SBRS theory when applied to differentiate explosive targets from inert targets. These simulations are considered in the next chapter.

4.1 Modeling of Shielding Design

Proper shielding of the D-T neutron generator is critical so that future experimental work will conform to regulations. A renowned shielding expert at Kansas State University, Dr. Kenneth Shultis, designed a multilayered collimator vault for shielding and collimating the neutron generator. Additionally, he designed a beam catcher to capture the neutron beam. The researcher modified Dr. Shultis' initial design as experimental plans evolved. Materials used in the shielding design consisted of iron sheets, polyethylene sheets, 5% and 8% borated polyethylene sheets and concrete. Then, radiation dose rate estimations were calculated through multiple simulations with the MCNP5 code and averaged over small disk areas at different locations inside and outside of the simulated future laboratory. During normal operation, the level of exposure desired was 2 mrem hr^{-1} or below for safe operating conditions. Because the technology is still in research and development stages, the shielding plan was designed as laboratory prototype shielding, not as a portable shielded field system. Locations on the roof of the laboratory where the source will be installed were shielded with borated polyethylene and polyethylene sheets due to openings caused from skylights in the rooms. The shielding modeling

evolved as the research continued. Initially, a setup involving only one room for the hot zone was used; see Figures 4.1 and 4.2. In Figures 4.1 and 4.2, materials are designated as follows:

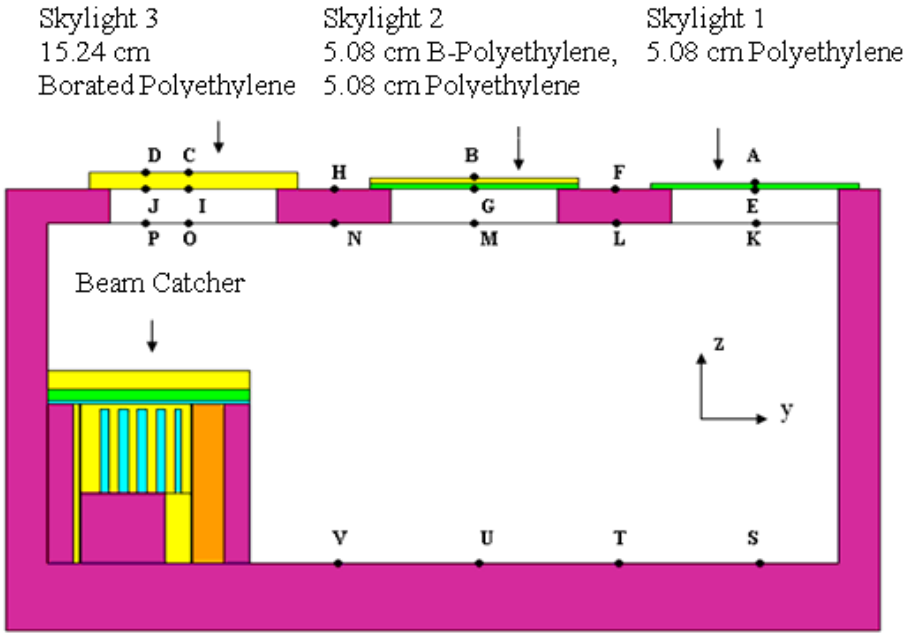

Figure 4.1 Preliminary MCNP Visual Edit cross-sectional diagram of laboratory setup examining roof and floor radiation dose rates.

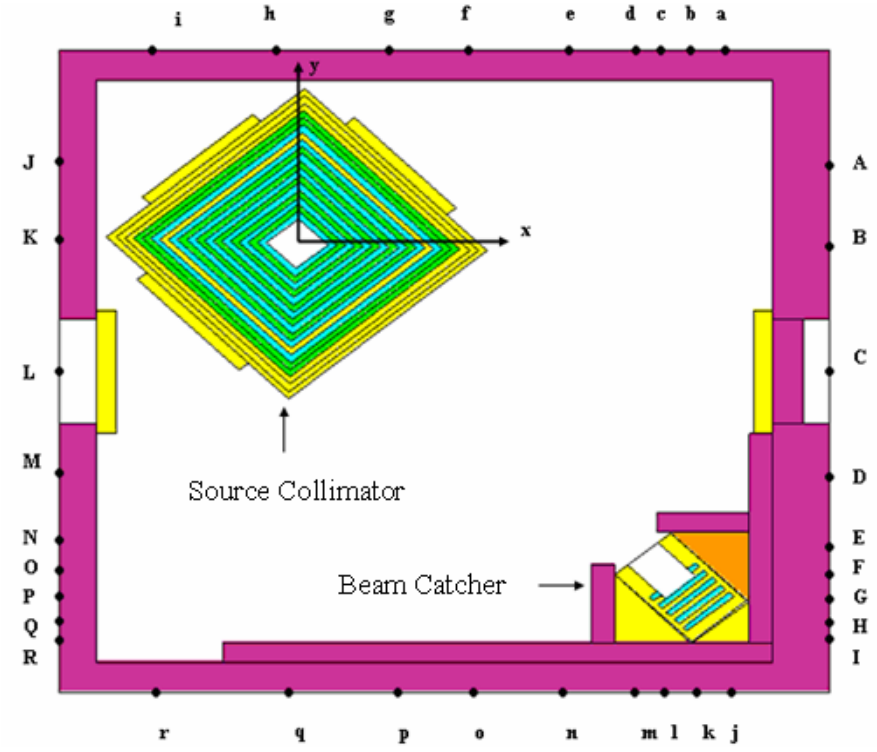

Figure 4.2 Preliminary MCNP Visual Edit cross-sectional diagram of laboratory setup examining wall radiation dose rates.

concrete, pink; 8% borated polyethylene, yellow; iron, light blue; polyethylene, green; and 5% borated polyethylene, tan. Ultimately, the room shown in Figures 4.1 and 4.2 in combination with a neighboring room for the experimental setup was more favorable for construction and operation purposes. Thus, the shielding plan was adapted to incorporate two rooms into the model. The revised shielding plans are shown in Figures 4.3 and 4.4.

During the shielding design alteration, several changes were implemented that created a more optimal shielding configuration. First, the beam catcher was enlarged to stop more of the beam. Additionally, the mouth or beam entrance of the beam catcher was made smaller to limit backscattering of the beam. For the same purpose, a cavity was designed inside of the beam catcher causing more neutrons to scatter into inner portions of the beam catcher, reducing backscatter. Some input specifications for the simulations are provided in Table 4.1.

Table 4.1 Shielding input specifications (double room).

Source Type:	Mono-energetic, 14.1-MeV neutrons
Source Bias:	Isotropic point source
Source Strength:	10^{11} n s^{-1}
Origin:	Center of source collimator
Source Position	(0,0,-20.32) 93.98 cm (37 in.) above floor
Operating Conditions	Performed in a vacuum
Dose Tallied	Neutron dose rate (mrem hr^{-1}) Photon dose rate (mrem hr^{-1})
Tally Type	F2 tally (with FM and SD cards) Ambient dose equivalent rates H*(10 mm) averaged over disks, 10 cm in radius
Source Collimator Dimensions	218.44 cm (86 in.) × 218.44 cm (86 in.) × 233.68 cm (92 in.)
Beam Catcher Dimensions	167.64 cm (66 in.) × 182.88 cm (72 in.) × 175.26 cm (69 in.)
Distance from Coll. to Beam Catcher Face	266.3 cm (8 ft. 8 in,) (Includes dividing wall)

The dividing wall in between the rooms also assisted with shielding. Next, the beam was collimated along the diagonal inside the source vault in the double room configuration. This further lengthened the degree of collimation and helped minimize scattering within the rooms. The beam opening on the collimator vault was also altered from a square cross-sectional hole to a circular cross-sectional hole, creating a fan-shaped beam with azimuthal symmetry along the axis of the beam. A further collimated beam and an improved beam catcher helped lower scattering within the rooms. Thus, material resources were conserved by using fewer materials in low dose rate areas of the room, including the roof skylights and next to the walls. In Figures 4.3 and 4.4, yellow denotes 8% borated polyethylene, green denotes regular polyethylene, red denotes concrete and light blue denotes iron. The dimensions of the insides of the two rooms are

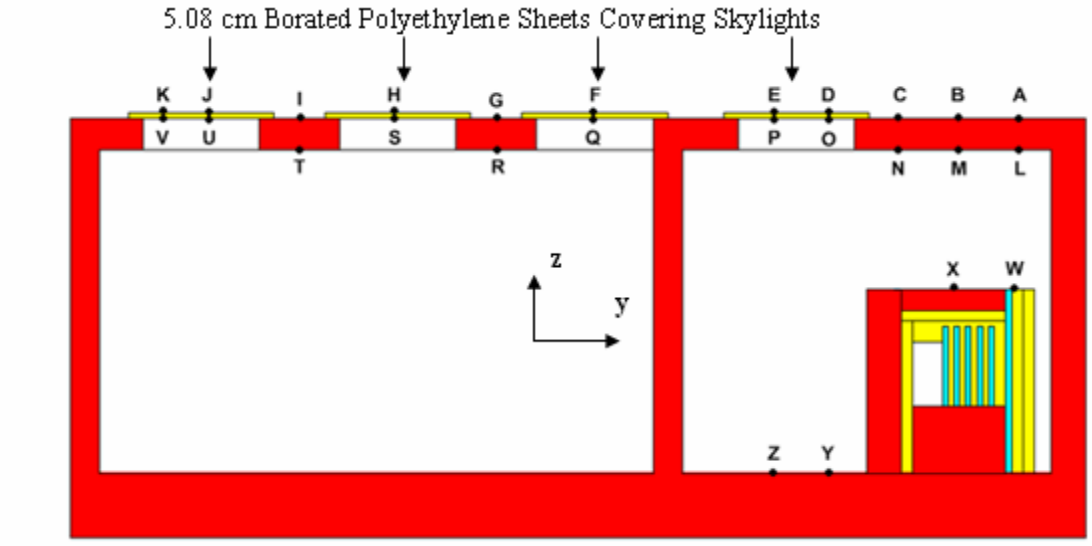

Figure 4.3 MCNP Visual Edit cross-sectional diagram of the double room laboratory setup examining roof radiation dose rates.

as follows, listed in order of x , y, z dimensions. The smaller room had dimensions 548.64 cm (18 ft.) × 579.12 cm (19 ft.) × 314.96 cm (10 ft. 4 in.), whereas the larger room had dimensions 568.96 cm (18 ft. 8 in.) × 386.08 cm (12 ft. 8 in.) × 314.96 cm (10 ft. 4 in.). The walls were typically 30.48 cm (1 ft.)-thick concrete, and the roof was 29.21 cm (11.5 in.)-thick concrete. The collimator vault and the beam catcher dimensions are shown in Table 4.1. The dose rates at many different points located on the walls, roof and floor were estimated. The specified points are shown in Figures 4.3 and 4.4. Dose rates at several different locations were estimated to ensure that the dose rate was uniform across the outsides of the rooms. For the points shown in Figure 4.3, dose rates for planes with x-values -60.0 cm, 60.0 cm, 170.0 cm, 260.0 cm, and 335

cm were calculated, assuming x=y=0 cm is the center of the collimator as shown in Figure 4.4. For the points shown in Figure 4.4, dose rates for planes with z-values -68.6 cm, -20.32 cm (beam height), 68.6 cm, and 99.1 cm were measured, where z= -114.3 cm was the floor height.

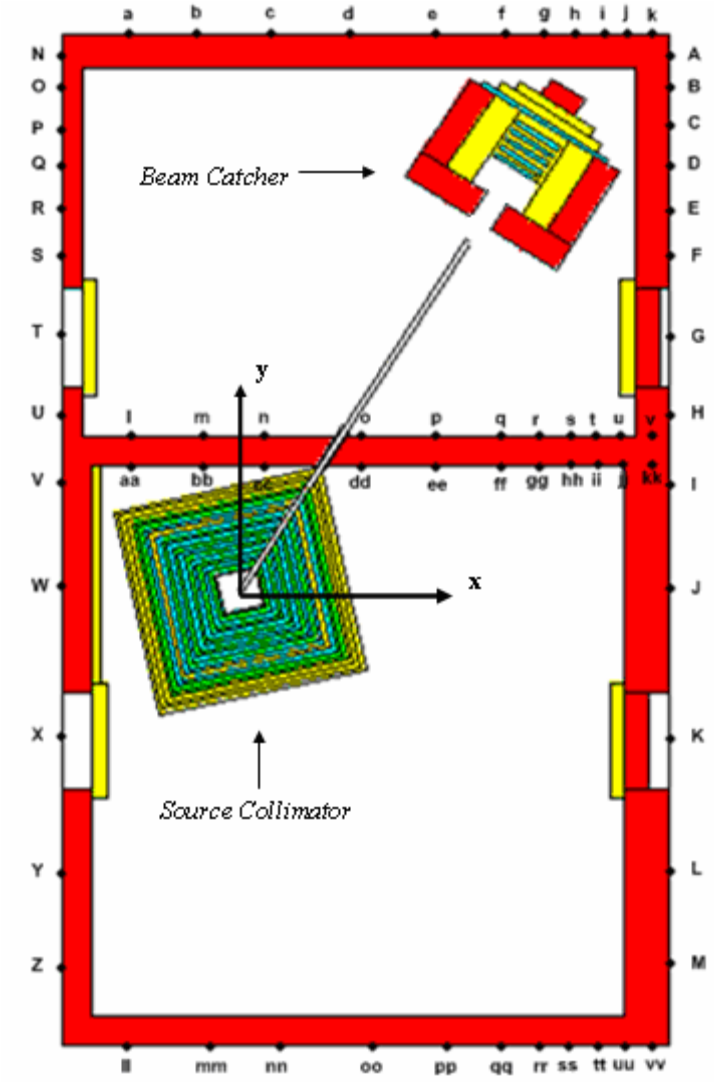

Figure 4.4 MCNP Visual Edit cross-sectional diagram of the double room laboratory setup examining wall radiation dose rates (picture shown at source elevation, z=-20.32 cm).

Of the planes chosen, those exhibiting the highest dose rates are listed in Appendix A. The simulations showed that dose rates for all points measured outside the two rooms were below 2 mrem hr^{-1}. Finally, a dose rate exceeding 2 mrem hr^{-1} was allowed within the rooms, as they would not be occupied during operation, and an interlock would be in place to turn off the source if a door into the room were opened. Overall, more operating room and improved beam collimation were achieved while using the double room configuration.

4.2 Neutron Beam Contour Mapping and Degree of Collimation

Simulations were performed to examine the profile of the beam that was perpendicular to the collimator (single room setup shown in Figures 4.1 and 4.2). It was critical for the design of the beam catcher and development of the interrogation technique that the approximate shape and intensity of the neutron beam be known. Therefore, simulations were performed to discretely map the beam intensity at different distances from the collimator vault. The results indicate the scattered neutron dose is dependent upon the level of collimation of the neutron beam and the dimensions of the opening of the beam catcher. When either was poorly chosen, a significant increase in scattered neutron dose resulted throughout the room. If the beam width at the position of the beam catcher face exceeds the mouth opening, significant scattering occurs, and the dose rates at other areas in the room increases substantially. However, if the opening is too large, then the beam will reflect out of the beam catcher without multiple scattering inside. This does not assist shielding and causes the neutron dose to increase within the rooms. Thus, these two latter effects must be balanced.

The level of collimation of the beam was investigated by testing two sizes of collimation openings on the collimator, a 10.16×10.16 cm (4×4 in.) hole and a 5.08×5.08 cm (2×2 in.) square hole. Additionally, a one foot thick concrete wall was placed in front of the collimator with an identical hole cut for further collimation. The ambient equivalent neutron dose rate (mrem hr^{-1}) was averaged over disks perpendicular to the direction of the beam in the y-z plan as shown in Figure 4.6. Estimates were performed at distances of 243.84 cm (8 ft.) and 365.84 cm (12 ft.) from the edge of the collimator and the concrete wall as seen in Figure 4.5.

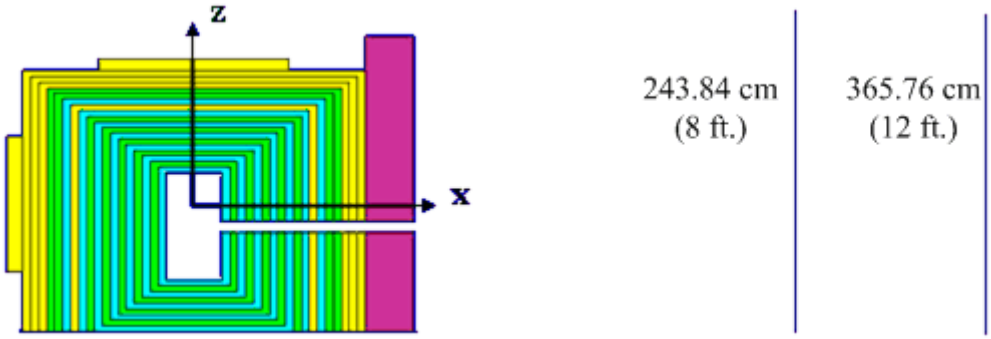

Figure 4.5 Cross-sectional diagram of xz-plane and beam collimation setup.

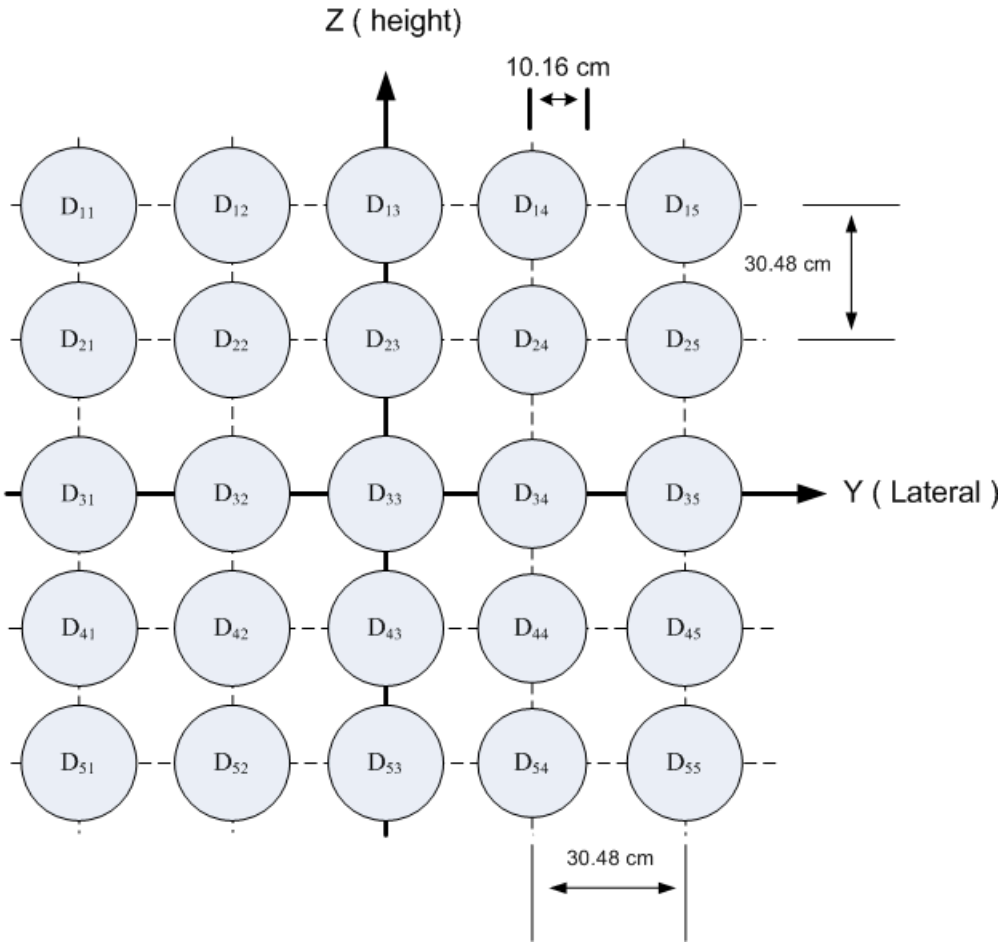

Figure 4.6 Schematic diagram of disks used for dose averaging in yz-plane.

These estimates examined the beam's intensity and width at two distances. The tabulated averaged dose rate results are given in Tables A.5 and A.6 of Appendix A. Surface plots demonstrating the beam intensity were generated, with example plots of the beam intensity incident on a normal plane positioned at x=243.84 cm shown in Figures 4.7 and 4.8 for the two different collimator hole sizes. The beam with the 5.08×5.08 cm hole showed an overall lower intensity than the 10.16×10.16 cm beam (see Tables A.5 and A.6). However, the 5.08×5.08 cm beam was better collimated (see Figures 4.7 and 4.8). Therefore, to keep scattering low, the 5.08×5.08 cm collimation system was chosen and helped to minimize shielding expenses in the laboratory rooms. The intensity will be lower; however, it will still be more than sufficient for swift interrogation applications.

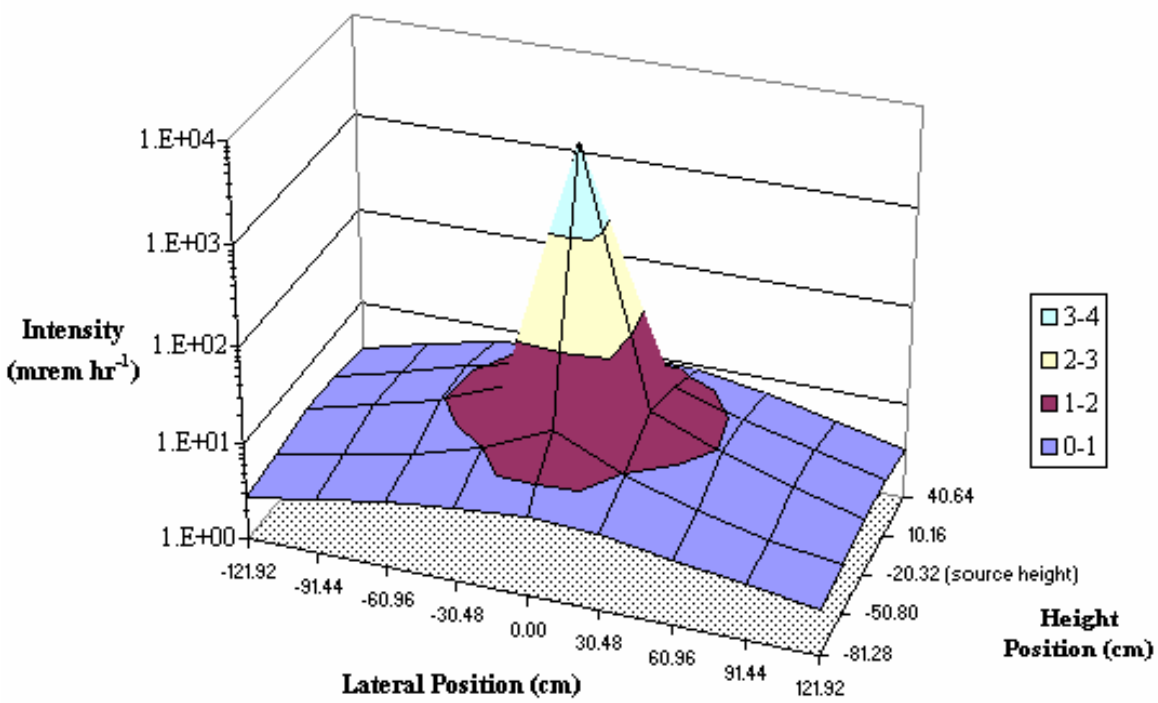

Figure 4.7 Semi-log plot of the Neutron beam intensity at 243.84 cm (8 ft.) incident on the yz-plane with 5.08×5.08 cm collimation hole.

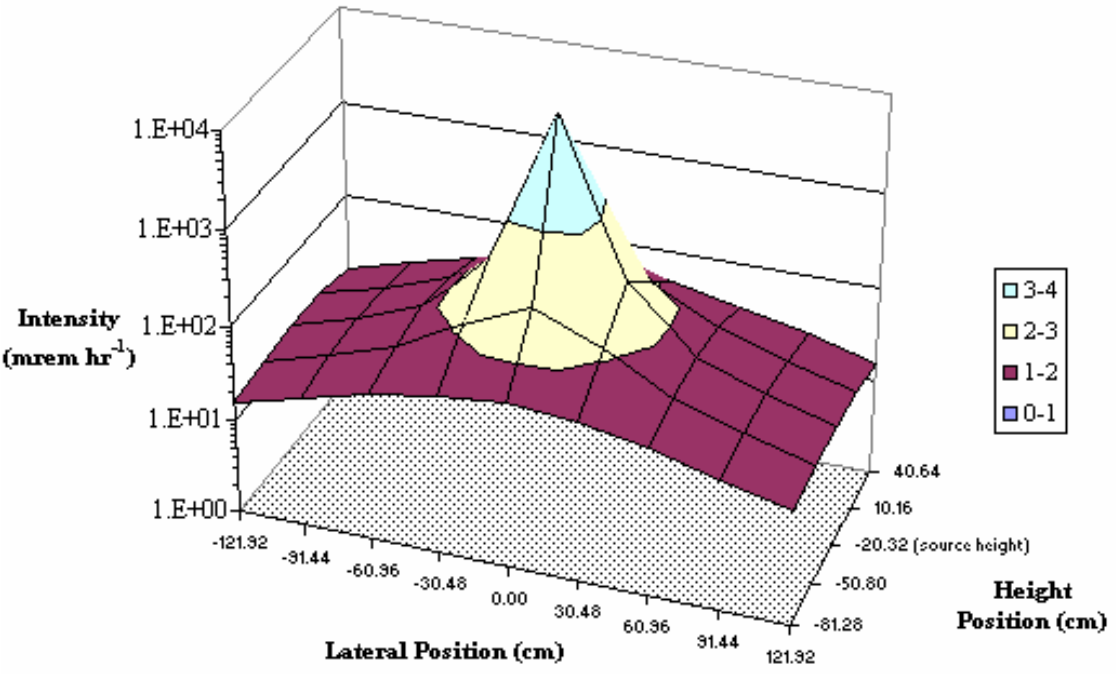

Figure 4.8 Semi-log plot of the Neutron beam intensity at 243.84 cm (8 ft.) incident on the yz-plane with a 10.16×10.16 cm collimation hole.

A second study of the contour of the neutron beam was performed with the final double room configuration (Figures 4.3 and 4.4). Here, the beam was changed from a square 5.08×5.08 cm hole in the collimator to a circular hole, radius 2.8661 cm, because it represented the same cross-sectional area of the 5.08×5.08 cm beam. Modeling ring surface areas outward from the center of the beam, yielded the dose rate of the neutron beam, see Figure 4.9, on the normal front plane of the beam catcher as a function of the radius. The width of the beam catcher's mouth was 25.4×25.4 cm, which the beam clearly fits inside. A hand calculation was also performed to find

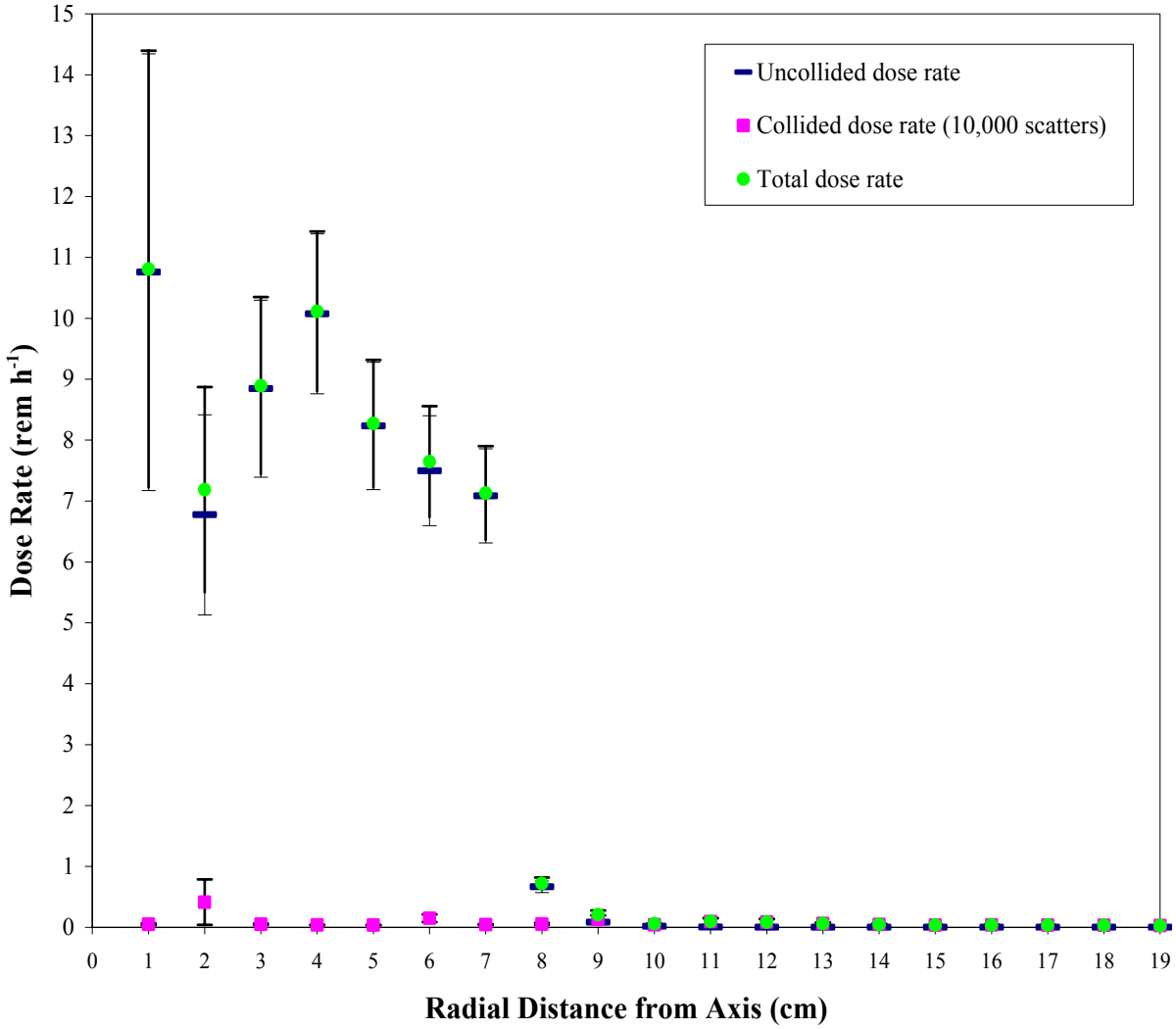

Figure 4.9 Estimated neutron dose rate as a function of radial distance on the front normal face of the beam catcher from a collimated 10^{11} n s^{-1} isotropic point source.

the uncollided dose rate at this distance, *r* from a point source in a vacuum (Shultis and Faw, 2000). It was found to be comparable to the simulated results shown in Figure 4.9.

Uncollided Dose Rate Calculation from a Point Isotropic Source:

The uncollided fluence from a point source emitting S_p particles a distance r from the source is

$$\Phi^o(r) = \frac{S_p}{4\pi r^2}. \tag{4.1}$$

The dose from mono-energetic particles a distance r from the source is

$$D^o(r) = \frac{S_p R}{4\pi r^2}, \tag{4.2}$$

where R is the appropriate detector response function for neutron ambient dose equivalents (H^*), or R =5.2 E-10 (Sv cm^{-2}) for neutrons of energy 14.0 MeV (ICRP 1996).

r is found to be (from point source to beam catcher front face):

$$r = \sqrt{(x_2 - x_o)^2 + (y_2 - y_o)^2} = 445.5 \text{ cm} \qquad \text{and} \qquad S_p = 1 \text{ part.} \tag{4.3}$$

Therefore, the dose at r is

$$D^o(445.5\ cm) = 2.085 \text{ E-16 Sv}, \tag{4.4}$$

and converting to rem with 1 Sv = 100 rem,

$$D^o(445.5\ cm) = 2.085 \text{ E-14 rem}. \tag{4.5}$$

Assuming a source strength of 10^{11} n s^{-1}, and making appropriate unit conversions, the uncollided dose rate is approximately:

$$\dot{D}^o(445.5\ cm) = 7.50 \text{ rem h}^{-1}. \tag{4.6}$$

4.3 Summary

Shielding simulations for a 14.1-MeV D-T isotropic point source of neutrons yielded a general plan for the shielding configuration. The double room configuration was chosen for the future laboratory. While the problem was not trivial, the design of the neutron beam catcher and the neutron collimation vault proved adequate to maintain dose rates below 2 mrem hr^{-1} at point measured outside the rooms. Also, the double room configuration was found to generate satisfactory neutron beams of high intensity, ~ 7-8 rem hr^{-1}, and sufficiently focused, ~ 14 cm in diameter, for interrogation of actual targets near the area of the beam catcher. The future laboratory was designed as a prototype, and therefore was a non-portable system. Future work for portable field applications will require further designing of the collimation system.

CHAPTER 5 - Target Simulation Modeling and Results

5.1 Target Interrogation Simulations

This section describes target simulation parameters used in most simulations within this chapter. Primarily, the goal of SBRS is to detect IEDs, often placed in vehicles. Thus, a simple car trunk was simulated representing potential vehicle targets. Several geometries were tried; however, the primary geometry used for simulations is shown in Figure 5.1. Many materials were simulated as both the sample and as the clutter material; they are listed in Appendix C including their composition and densities. For this chapter, the notation used in target simulations will now be defined.

- **Sample** – A steel cylindrical-shell volume approximately the size of 3.785 L (1 gal.) paint can, which contains an unknown material.
- **Explosive** – Nitrogen-rich explosive material that may occupy the sample volume.
- **Inert** – Any material that is not classified as a nitrogen-rich explosive (may be otherwise dangerous) that may occupy the sample or clutter volume.
- **Clutter** – A small rectangular volume of an inert material that may "shield" the explosive sample within the target.
- **Target** – A 1 m^3 aluminum-shelled box that contains an unknown sample and inert clutter.
- **IED** – A target in which the unknown sample is an explosive.
- **Source** – A MCNP disk source emitting either 14.1-MeV parallel neutron beams or a Watt distribution from ^{252}Cf parallel neutron beams, 7.62 cm in radius.
- **Detector** – A point flux detector F5 tally used in MCNP with radius 10 cm.

5.1.1 Target Geometry Specifications

The targets' 0.2 cm aluminum shell was used to resemble a car trunk. One face of the box rested on the xy-plane, centered on the origin. The target rose in the z-direction and its center was located at z=50 cm; it contained a sample, which was composed of a cylindrically-shaped carbon steel shell. The sample was used to house explosive and inert materials and had a radius

7.62 cm, height 20.75 cm and thickness 0.12 cm, with inner volume 3.785 L. The sample was centered in the target in the x, y and z directions at coordinates x=y=0 and z=50 cm. The target also contained a rectangular parallelepiped of clutter material 50 cm in height (z-direction), 32 cm in length (x-direction) and 10 cm in width (y-direction). The clutter material was placed in between the source and the cylindrical sample, as shown schematically in Figure 5.1. The center of the clutter material was offset in the y direction to y= -17 cm, and centered in the x and z directions at x=0 and z=50 cm within the target. The source was located at coordinates: (0, -150, 50), or a 1 m standoff distance from the nearest target face. It was aimed directly toward the middle of the clutter, cylindrical sample, and target box, at z=50 cm parallel to the y-axis and traveling in the positive y-direction. The gamma-ray fluence was tallied with an F5 tally (point detector) at a position 153 cm away from the outermost point of the target at coordinates (200, -100, 50). Simulations were performed in a vacuum using 4-keV wide energy bins in a tally, each with the signature energy at the center of the bin. The width of the energy bins was chosen to be similar to the energy resolution of some HPGe detectors.

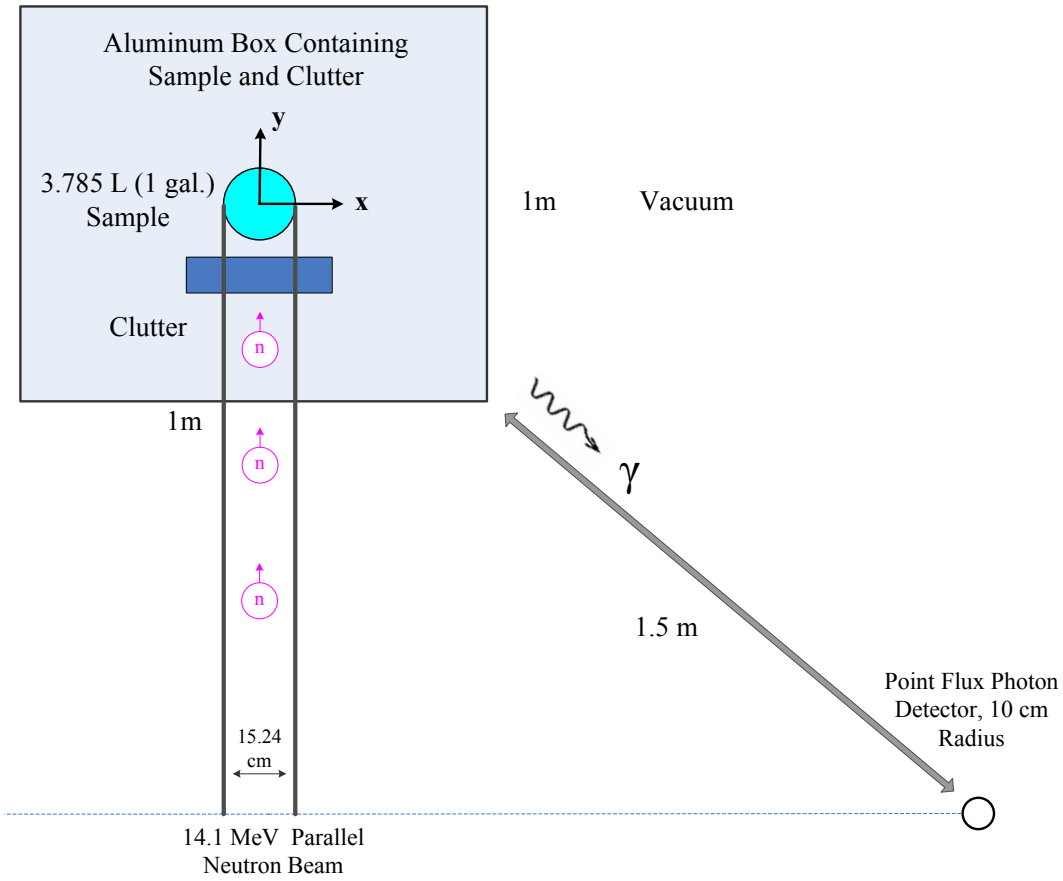

Figure 5.1 Schematic diagram of simulated target geometry.

In all simulations, histories of at least 10 million and up to 50 million particles were simulated. All tally F5 fluence responses and their deviations were multiplied by a factor of 10^{12} neutrons for legibility. Several locations were tried for placement of the point detector with all positions located near source. For detectors with similar distances to the sample, the responses received at different detector positions were similar, due to target symmetry (without the clutter present). It is sought to keep detectors close to the target, because the response decreases as $1/r^2$. However, it was placed at least 1 m away to achieve stand-off detection and was located near the source, because ideally the detection equipment for SBRS should be close together. The detector position shown in Figure 5.1 was used for all simulations in chapter 5, except section 5.2 and 5.4.3. However, shielding requirements of an experimental prototype would constrain detector locations. Ideally, the detector would be located near the source, but such that the geometry of the target would minimize the effect of clutter. For example, if a rectangular shaped target is interrogated, the detector should be placed such that it is exposed to side of the target that is the least thick. Thus, if the target contained homogenous clutter throughout, the response would travel through the least amount of attenuating material, increasing the detection probability. In initial simulations, the clutter volume was not used. Later simulations involved the clutter volume, and many possible inert materials were considered, as either the clutter, or the sample and the clutter. However, the detector was positioned such that the gamma ray fluence from the sample did not travel through a significant portion of the clutter volume.

5.1.2 Neutron Sources Used for Target Simulations

Two neutron sources were simulated for explosive interrogation. Initially, a ^{252}Cf spontaneous fission neutron source was investigated, generating a Watt fission spectrum

$$f(E) = C\exp(-E/a)\sinh(\sqrt{bE}), \tag{5.1}$$

with constants a=1.025 and b=2.926 from MCNP5 manual I. Because ^{252}Cf is a portable neutron source and less costly than a neutron generator, it was used initially for interrogation purposes. The second and primary source used in the simulations was a 14.1-MeV neutron beam, representative of a collimated D-T neutron generator neutron beam. For this source, a mono-energetic beam was assumed, although the actual energy distribution may vary slightly from generator to generator but should be primarily composed of 14.1-MeV neutrons. A plane parallel

disk source, radius 7.62 cm (3 in.) specified both sources, similar to a highly collimated neutron point source at some distance away.

5.1.3 Estimated Count Time Required with a HPGe Detector and 14.1-MeV Neutrons of Intensity 10^{11} s^{-1}.

Assume a gamma-ray fluence Φ_γ from the RDX sample (with distance > 2 m) of energy E=2 MeV incident upon the location of the point detector that can be approximated by a parallel beam. Also, assume a HPGe crystal is positioned at the location of the point detector as shown in Figure 5.2, perpendicular to the beam. Typical responses from the F5 tally within a 4-keV energy

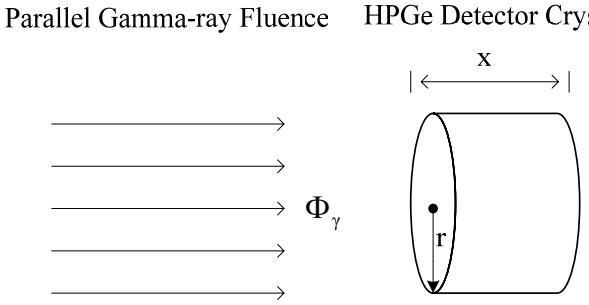

Figure 5.2 Parallel gamma-ray fluence incident upon a HPGe detector.

bin centered on the signature energies in target simulations were of the order of magnitude of 10^{-9} to 10^{-8} cm^{-2}, normalized per source neutron. Thus, assume a fluence of 2 MeV gamma rays incident on the point detector of

$$\Phi_\gamma = 5\times10^{-9}\ \text{cm}^{-2}. \tag{5.2}$$

The 80% efficient HPGe detector from Canberra, model: GC8021 has crystal dimensions: radius r= 3.675 cm and length x= 7.25 cm. A density ρ= 5.32 g cm^{-3} was assumed for the crystal. The area of the detector is

$$A_{\text{det}} = \pi r^2 = 41.43\ \text{cm}^2. \tag{5.3}$$

The photoelectric absorption attenuation coefficient for photons with E=2 MeV, is

$$\mu = \mu_o \rho = (2.02\times10^{-4}\text{cm}^2\ \text{g}^{-1})(5.32\ \text{g cm}^{-3}) = 0.00107\ \text{cm}^{-1}. \tag{5.4}$$

The intrinsic full-energy efficiency of the detector can be approximated by

$$\varepsilon(E) = 1 - e^{-\mu x}. \tag{5.5}$$

Therefore, for photons of energy E =2 MeV, the intrinsic efficiency is

$$\varepsilon(2\ \text{MeV}) = 0.00776. \tag{5.6}$$

Finally, the counts in the full energy peak per source neutron are approximately

$$\Phi_{\gamma} A_{\text{det}} \varepsilon = \left(5\times10^{-9}\ \text{cm}^{-2}\right)\left(42.43\ \text{cm}^{2}\right)\left(0.00776\right) = 1.65\times10^{-9}. \quad (5.7)$$

For a neutron source intensity=10^{11} s^{-1} and a time= 10 s, the number of counts in the full energy peak would be approximately

$$\text{Counts}=\left(1.65\times10^{-9}\right)(10^{11}\ \text{s}^{-1})(10\ \text{s}) = 1646. \quad (5.8)$$

Therefore, with a 14.1 MeV neutron source of intensity 10^{11} s^{-1} and an efficient HPGe detector, it is approximately feasible to obtain significant counts for the detection of explosives in terms of seconds.

5.2 Interference Gamma Rays from Low-to-Mid Atomic Number Elements

It would be very useful for the purpose of explosive detection to obtain characteristic signature energies from the elements H, C, N, and O. Ideally, signature energies would be easy to detect and unique. However, almost all elements can emit numerous gamma rays during de-excitation. Some of these gamma rays may be emitted by elements at energies equivalent to or very near the signature energies shown in Table 3.1. An **interference** gamma ray is one that is emitted by a nucleus from some element and whose energy is within a 4-keV wide energy bin of the energy of one of the signature energies in Table 5.1. A signature energy that is unique has no interferences and is conclusive in identifying the element from which it was emitted. Signature energies with little interference are better than those with much interference.

The MCNP5 code was used to generate pulse height tallies from irradiation of elements with atomic numbers ranging from 1 to 30 by a 14.1-MeV source. 10 million histories were performed for each simulation. A one gallon cylindrical sample contained the element considered and had radius=7.62 cm, height=20.75 cm and center at (x=y=0, z=50) with the axis of the cylinder on the z-axis. A 14.1-MeV source was used identical to the source discussed in section 5.1. Natural densities were used for elements existing in a solid state (at STP). For gaseous elements (at STP), a density of 0.5 g cm^{-3} was used. A higher density than the natural density was used for gaseous elements to ensure the neutron beam would interact with a significant amount of the element. Because the noble gases below atomic number 30 (specifically He, Ne and Ar) very rarely form compounds of significant densities, they were not included in simulations. Also, naturally existing isotopes of the 27 elements modeled that had an abundance of at least 1% of the element's composition were included. A cylindrical detector of

germanium, density 5.32 g cm^{-3} was modeled and a gamma-ray pulse height tally (F8 tally) was recorded in the cell of the cylinder. The F8 tally provides the energy distribution of pulses in a cell, modeled after a physical detector. A very large germanium detector was used to ensure detection of many pulses. The cylinder had a radius of 9 cm and was 33 cm long. The detector was placed near the target with the base of the cylinder orientated towards the target. The center of the base was located 85 cm away from the center of the target. The axis of the cylinder was parallel to the normal of the side of the sample at a height of z= 50 cm (center of the sample). The pulse height tally was binned by energy with 4-keV wide bins, from 0 to 11 MeV.

Using the MCNP output, spectra for H, C, N, and O first were constructed. Each peak was fit by a Gaussian distribution with MATLAB. This was similar to a spectrum using a HPGe detector with decent energy resolution (HPGe detectors typically have ~2.5 keV energy resolution). The N spectrum for energies 0-10 MeV is shown in Figure 5.3. The pulse height spectra for H, C, and O are shown in Figures F.1–F.3 of Appendix F.

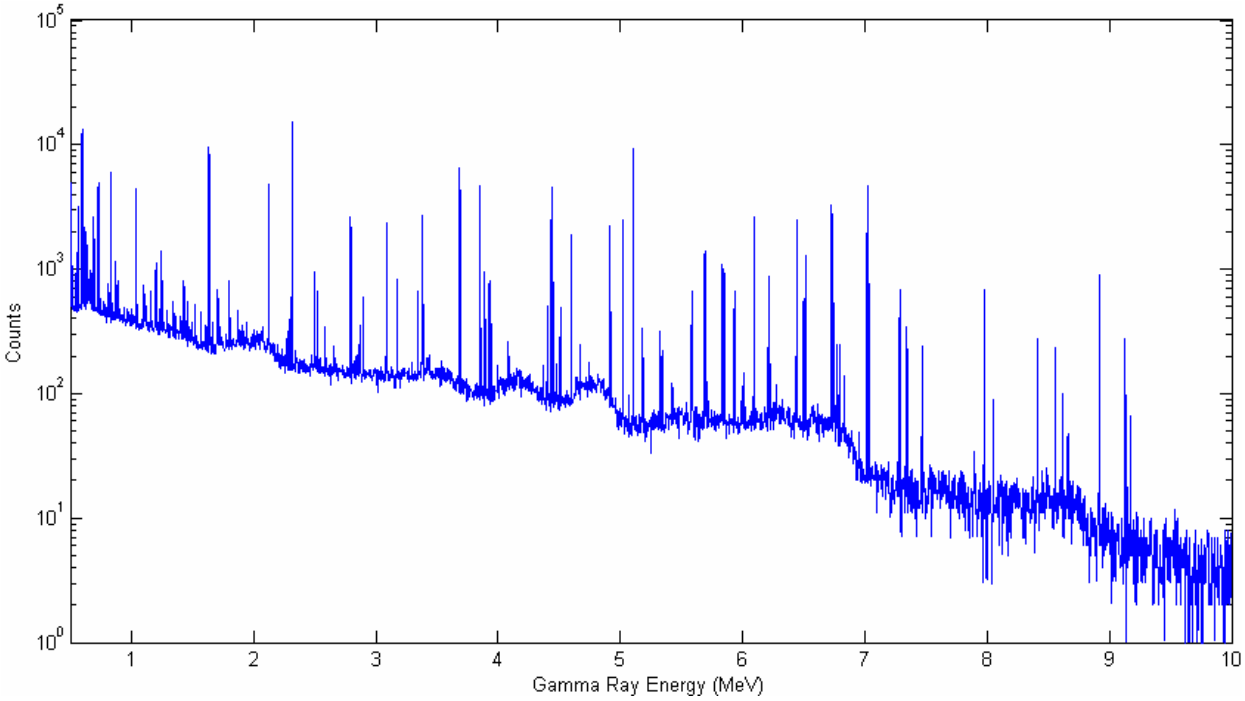

Figure 5.3 MCNP simulated pulse height tally spectrum for a sample containing pure N irradiated by 14.1-MeV neutrons.

Next, the number of peaks emitted into the same 4-keV wide bin that one of the signature energies was emitted into was found for each of the remaining 27 elements (elements whose Z is from 1 to 30, less He, Ne, and Ar). Peaks were considered to occur in bins with counts exceeding

the local count continuum by 2σ. These peaks were considered interferences. The same process was applied to an RDX sample to see if the signatures energies in Table 3.1 could be identified as peaks from RDX, and results are shown in Table 5.1. Table 5.1 also shows the total number of interferences found for each signature energy from 27 elements and their naturally occurring isotopes. Results showing the number of interferences for each signature energy found from each of the 27 elements are given in Appendix B.

Table 5.1 The number of interference peaks emitted into 4-keV wide energy bins containing the signature energies that had counts exceeding 2σ of the count continuum from a pulse height tally for 27 elements and the peaks found from an RDX sample.

Element	Signature Energy (MeV)	Total Interference Peaks	Peaks with RDX Sample
H	2.2232		1
C	1.2618	1	
	3.6839	2	1
	4.4390	2	1
	4.9453		
N	0.7284	1	1
	1.6353	22	1
	1.8848	1	
	2.3128		1
	2.7931	1	1
	3.3786	1	1
	3.8907	1	1
	4.9151		1
	5.1059		1
	5.2692	1	
	6.4462	1	1
	7.0291		1
	10.8291		
O	0.8707	1	
	1.0879	3	
	2.1845	2	
	2.7420		1
	6.1299		1
	6.9171	1	1
	7.1168		1

Next, optimal signature energies were selected from Table 5.1, where an optimal signature energy had a peak from the RDX sample, and no interferences. However, C had no signature energies without interferences; therefore, optimal signature energies for C were selected that had a peak from the RDX sample and the least number of interferences. Interestingly, the C sample had no peak for the 3.6839-MeV signature energy, but N and O were found to have interferences. Most likely, the peak from the RDX sample for the 3.6839-MeV C signature energy is not from C but either N or O, because the concentration of C is much lower within the RDX sample than within the C sample. A N prompt-capture gamma ray (not included in Table 3.1) might have caused the interference, which was emitted at 3.6777 MeV with cross section 0.0115 barns (Molnar, 2004). This energy was not contained within the 4-keV wide energy bin (limits 3.6831 – 3.6869 MeV), which suggests that the MCNP END/F database may have used a slightly higher energy value. Examining the NNDC database for O, no gamma rays were found to be emitted within the energy bin for this signature energy. It is unclear what caused this interference, but it must be from data in the MCNP database. Whatever the case, the C 3.6839-MeV signature energy was not selected to be an optimal signature energy. C was found to have a large peak within the bin for the 4.4390-MeV signature energy. However, both N and O samples also had interferences with this signature energy. However, no gamma rays from the NNDC database were found near the energy of 4.4390 MeV for either O or N. Therefore, the C signatures in Table 3.1 were not found to be unique within the bounds of this study; nevertheless, the 4.4390-MeV signature energy was selected for C. The results were very encouraging. Nine optimal signature energies were found and are shown in Table 5.2. Thus, if the SBRS method exploits these optimal signatures, it should be a powerful method for explosive identification.

Table 5.2 The 9 optimal HCNO inelastic-scatter and prompt-capture signature energies.

Element	Signature Energy (MeV)	Thermal Cross Section (barns)	14.1-MeV Cross Section (barns)
H	2.2232	0.3326	-
C	4.4390	-	0.2106
N	2.3128	-	0.0557
N	4.9151	-	0.00687
N	5.1059	-	0.0437
N	7.0291	-	0.0242

O	2.7420	-	0.0433
O	6.1299	-	0.144
O	7.1168	-	0.0625

5.3 Simulations Using Strictly Explosive or Inert Samples and the Average Explosive Template

This section addresses results dealing with either explosive or inert samples (no clutter), two neutron sources and the effect of having the sample off-set from the beam in the xy-plane. First, a ^{252}Cf neutron source was used for simulations. Then, simulations were performed with a 14.1-MeV neutron source.

5.3.1 Results Using a ^{252}*Cf Neutron Source*

A ^{252}Cf spontaneous fission neutron source was modeled as a collimated disk source, emitting a cylindrical beam 3 cm in radius parallel to the y-axis as described in section 5.1. In these simulations, only targets containing strictly explosive materials and strictly inert materials were examined. The objective was to test the ability of SBRS to distinguish between nitrogen-rich explosives and inert materials, using a portable ^{252}Cf radioisotope source.

During many experiments, particularly initial experiments, the optimal signature energies were not yet known. Thus, various signature energies were tried for their utility in explosive identification. These experiments were performed at the beginning of the research and used 11 signature energies that are shown in Appendix D. Energy bins of ± 10 keV were used to bin the signature energies in tallies. Several different inert and explosive materials, shown in Table 5.3, were simulated. The densities and compositions for the materials modeled in these simulations can be found in Appendix C. A simple geometric scenario was used, identical to Figure 5.1, with the clutter volume absent. Two types of templates were used for analysis. First, templates were made by using responses for each of the simulated explosives individually. For example, an ammonium nitrate template was made from the responses of ammonium nitrate. Secondly, a template was formed from the responses of an average composition nitrogen-rich explosive, with composition 2.98% H, 20.29% C, 30.81% N and 46.14% O (National Research Council, 2004) and density 1.65 g cm^{-3}. This template was defined as the average explosive composition template (AECT).

Results demonstrated that the AECT worked more effectively than individual explosive templates at differentiating multiple types of explosives. AECT results are shown in Table 5.3. Individual explosive templates were effective at differentiating the explosive they were designed for, ie. the ammonium nitrate template clearly differentiated ammonium nitrate, but could not differentiate other explosives well.

Table 5.3 ^{252}Cf neutron beam results with AECT for 21 explosive materials and 11 inert materials.

Sample Material	ζ	$\sigma(\zeta)$	$f_{-}(3) = \zeta - 3\sigma(\zeta)$	$f_{+}(3) = \zeta + 3\sigma(\zeta)$
Ammonium Nitrate	5114.26	43.13	4984.89	5243.63
Ammonium Picrate	59.85	4.67	45.85	73.84
Cyclonite (RDX)	67.11	4.94	52.29	81.94
Guanidine Nitrate	1558.55	23.81	1487.14	1629.97
HMTD	2060.26	27.37	1978.14	2142.37
HNIW	5669.80	45.41	5533.58	5806.01
Hydrazine Nitrate	4037.70	38.32	3922.75	4152.65
Nitroglycerin	186.98	8.25	162.24	211.72
Nitrotriazolone (NTO)	4718.73	41.42	4594.46	4843.00
Octogen (HMX)	24.30	2.97	15.38	33.21
PETN	195.45	8.43	170.16	220.74
Picric Acid	3920.65	37.76	3807.38	4033.93
TAGN	1860.26	26.01	1782.24	1938.29
TATB	169.66	7.86	146.10	193.23
Tetrazene	9431.12	58.56	9255.44	9606.81
Tetryl	2080.81	27.51	1998.28	2163.33
TNAZ	490.70	13.36	450.62	530.77
TNB	3804.59	37.20	3693.00	3916.18
TNT	194.32	8.41	169.10	219.53
Trinitropyridine	11924.89	65.85	11727.34	12122.44
Urea Nitrate	1177.80	20.70	1115.71	1239.88
Air	47474.03	131.39	47079.87	47868.20

Aluminum	37893.57	117.39	37541.41	38245.73
Concrete	23722.01	92.88	23443.38	24000.65
Glass	42415.33	124.19	42042.75	42787.90
Petroleum	29441.82	103.47	29131.40	29752.23
Polyethylene	29354.60	103.32	29044.65	29664.55
Soil	2094.44	27.60	2011.65	2177.23
Soy	17180.21	79.04	16943.09	17417.33
Steel	31411.00	106.88	31090.37	31731.62
Water	28423.30	101.67	28118.31	28728.30
Wood	5245.46	43.67	5114.43	5376.48

Uniform weight factors were used for the signature energies chosen and the AECT was applied to all targets. Choosing f_o=15,000, soil and wood were false positives with $f_+(3)$ values of 2177.23 and 5376.48, indicating that their signatures did not match well enough with those from the template. However, there were no false negatives because all 21 explosive targets had $f_+(3)$ values below f_o=15,000, indicating that their signatures matched those from the template well. It was found that a ^{252}Cf source can be used to achieve fairly good explosive-inert differentiation of targets containing only a single sample. However, disadvantages of a ^{252}Cf source and other radioisotope sources are that they pose a risk of contamination and they decay with time.

5.3.2 Results Using a 14.1-MeV Neutron Source

The second series of experiments used higher energy neutrons of 14.1 MeV, such as those from a DT generator. This source offered advantages of higher energy and higher intensity than an isotope source and was capable of generating additional signature energies. The same experimental parameters were applied in this set of experiments as in the previous section, with only the source energy altered. Because not all the signature energies had been identified yet and the optimal signature energies were not yet known, the eleven signature energies used for the ^{252}Cf experiments were used and are listed in Appendix D. Templates were fashioned in a similar manner, and the analysis code was used to determine the effectiveness of various types of templates. A third type of template was also used in addition to individual explosive templates

and the AECT. The third template is defined as the average explosive template (AET), and it was made as follows. The responses for the twenty-one explosives shown in Table 5.4 were averaged for each of the signature energies. Using error propagation, the standard deviations for each response in the average explosive template was estimated. A matrix of response vectors

$$\vec{\vec{R}} = \begin{pmatrix} R_{11} & \cdots & R_{1n} \\ \vdots & \ddots & \vdots \\ R_{N1} & \cdots & R_{Nn} \end{pmatrix} \tag{5.9}$$

was formed, where N indicates the signature number and n the explosive number, using the explosives shown in Table 5.4 arranged alphabetically. Similarly, a matrix of response standard deviations was formed. The standard deviation was calculated for row one of $\vec{\vec{R}}$ by

$$\sigma_{1ave} = \sqrt{\left(\frac{\partial R_{1ave}}{\partial R_{11}}\right)^2 \sigma_{11}^2 + \left(\frac{\partial R_{1ave}}{\partial R_{12}}\right)^2 \sigma_{12}^2 \ldots + \left(\frac{\partial R_{1ave}}{\partial R_{1n}}\right)^2 \sigma_{1n}^2}\,, \tag{5.10}$$

where

$$R_{1ave} = \frac{\sum_{n=1}^{N} R_{1n}}{n}\,. \tag{5.11}$$

This was performed for each row of the matrix to estimate the standard deviations for the AET. The results of the simulations with analysis using the AECT and the AET are shown in Tables 5.4 and 5.5. It was found, that the AECT and the AET both worked reasonably effectively. Statistics of both template results are shown in Table 5.6.

Table 5.4 14.1-MeV neutron beam results with AECT for 21 explosive and 11 inert samples.

Sample Material	ζ	$\sigma(\zeta)$	$f_{-}(3) = \zeta - 3\sigma(\zeta)$	$f_{+}(3) = \zeta + 3\sigma(\zeta)$
Ammonium Nitrate	27777.4	100.5	27475.8	28078.9
Ammonium Picrate	3585.7	36.1	3477.4	3694.1
Cyclonite (RDX)	930.1	18.4	874.9	985.3
Guanidine Nitrate	9493.0	58.8	9316.7	9669.2
HMTD	10164.1	60.8	9981.7	10346.5
HNIW	2116.4	27.7	2033.2	2199.7
Hydrazine Nitrate	24086.5	93.6	23805.7	24367.3

Nitroglycerin	6098.8	47.1	5957.6	6240.1
Nitrotriazolene	2994.9	33.0	2895.9	3093.9
Octogen (HMX)	992.2	19.0	935.2	1049.2
PETN	4699.7	41.3	4575.7	4823.7
Picric Acid	8226.7	54.7	8062.6	8390.8
TAGN	21095.2	87.6	20832.4	21357.9
TATB	4060.6	38.4	3945.3	4175.9
Tetrazene	57496.7	144.6	57062.9	57930.5
Tetryl	3359.6	35.0	3254.8	3464.5
TNAZ	885.6	17.9	831.8	939.4
TNB	7719.3	53.0	7560.3	7878.2
TNT	9885.0	60.0	9705.2	10064.9
Trinitropyridine	5023.1	42.7	4894.9	5151.3
Urea Nitrate	22095.3	89.6	21826.4	22364.2
Air	115777.9	205.2	115162.3	116393.4
Aluminum	101469.3	192.1	100893.1	102045.6
Concrete	40619.2	121.5	40254.6	40983.8
Glass	40244.5	121.0	39881.5	40607.4
Petroleum	125414.0	213.6	124773.3	126054.6
Polyethylene	129363.9	216.9	128713.2	130014.6
Soil	41938.6	123.5	41568.1	42309.1
Soy	51670.4	137.1	51259.2	52081.6
Steel	100394.0	191.1	99820.8	100967.2
Water	73442.5	163.4	72952.2	73932.8
Wood	20321.0	86.0	20063.1	20578.9

Table 5.5 14.1-MeV neutron beam results with AET for 21 explosive and 11 inert samples.

Sample Material	*ζ*	*σ(ζ)*	$f_{-}(3) = \zeta - 3\sigma(\zeta)$	$f_{+}(3) = \zeta + 3\sigma(\zeta)$
Ammonium Nitrate	78451.1	168.9	77944.4	78957.8
Ammonium Picrate	7968.7	53.8	7807.2	8130.2

Cyclonite (RDX)	1687.2	24.8	1612.9	1761.5
Guanidine Nitrate	17241.1	79.2	17003.5	17478.6
HMTD	32689.8	109.0	32362.7	33016.8
HNIW	5436.6	44.5	5303.2	5570.0
Hydrazine Nitrate	79250.4	169.8	78741.1	79759.7
Nitroglycerin	13365.7	69.7	13156.6	13574.9
Nitrotriazolene	5563.5	45.0	5428.5	5698.4
Octogen (HMX)	2076.9	27.5	1994.5	2159.3
PETN	10342.1	61.3	10158.2	10526.1
Picric Acid	17847.2	80.6	17605.5	18088.9
TAGN	42029.7	123.6	41658.8	42400.6
TATB	8012.4	54.0	7850.5	8174.3
Tetrazene	320202.7	341.2	319179.0	321226.3
Tetryl	7478.4	52.1	7322.0	7634.9
TNAZ	2803.2	31.9	2707.4	2899.0
TNB	16090.4	76.5	15860.9	16319.9
TNT	19373.6	83.9	19121.8	19625.4
Trinitropyridine	11174.7	63.7	10983.4	11365.9
Urea Nitrate	55967.8	142.7	55539.8	56395.8
Air	1562790.5	753.8	1560529.0	1565052.1
Aluminum	954384.3	589.1	952617.0	956151.6
Concrete	170551.0	249.0	169803.9	171298.1
Glass	102691.7	193.2	102112.0	103271.4
Petroleum	981769.5	597.5	979977.0	983562.0
Polyethylene	991448.6	600.4	989647.3	993249.9
Soil	192159.5	264.3	191366.5	192952.5
Soy	276506.2	317.1	275554.9	277457.5
Steel	891198.9	569.3	889491.1	892906.7
Water	285541.3	322.2	284574.6	286508.0
Wood	162539.7	243.1	161810.4	163269.1

Table 5.6 Comparison of results using AECT and AET.

	AECT	*AET*
Average Inert ζ	76423.2	597416.5
σ of Inert ζs	39373.3	492872.9
Average Explosive ζ	11085.0	35954.9
σ of Explosive ζs	13360.4	69175.2
	(f_o=35,000) for AECT	(f_o=100,000) for AET
False Positives	1	0
False Negatives	1	1

Using f_o=35,000, the AECT had only one false positive, wood with $f_+(3)$= 20578.9, and one false negative, tetrazene with $f_+(3)$= 57,930.5. When the AET was applied with f_o=100,000, tetrazene was again a false negative with $f_+(3)$= 321,226.3; however, there were no false positives. Thus, the AET was more effective. Tetrazene is particularly difficult to distinguish among explosives because it has a density of 0.45 g cm^{-3} and is 74.44% N by weight, differing strongly from the average explosive composition and density of 30.81% weight N and 1.65 g cm^{-3} (see Appendix C). Using the average figure-of-merit and standard deviation from the figures-of-merit for each class of materials, probability density functions were generated as shown in Figures 5.4 and 5.5, comparing the general effectiveness of the AECT and the AET. Overall,

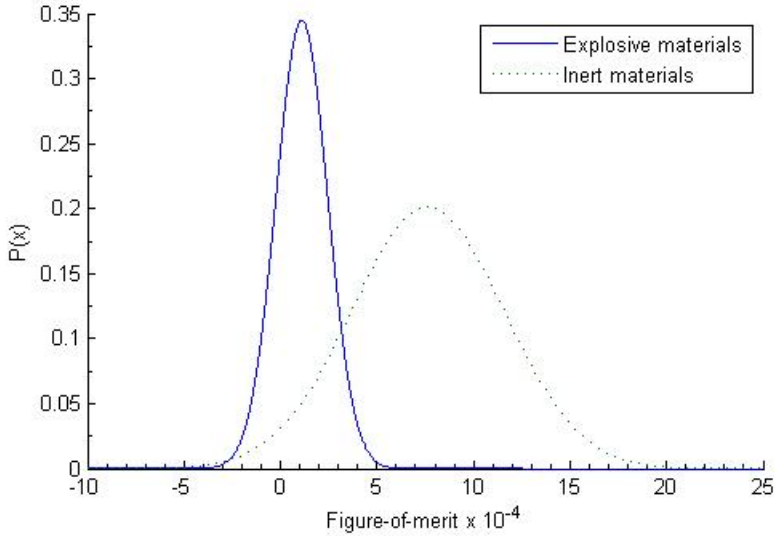

Figure 5.4 PDF comparing the figures-of-merit for two classes of materials, nitrogen-rich explosives and inert materials, with AECT.

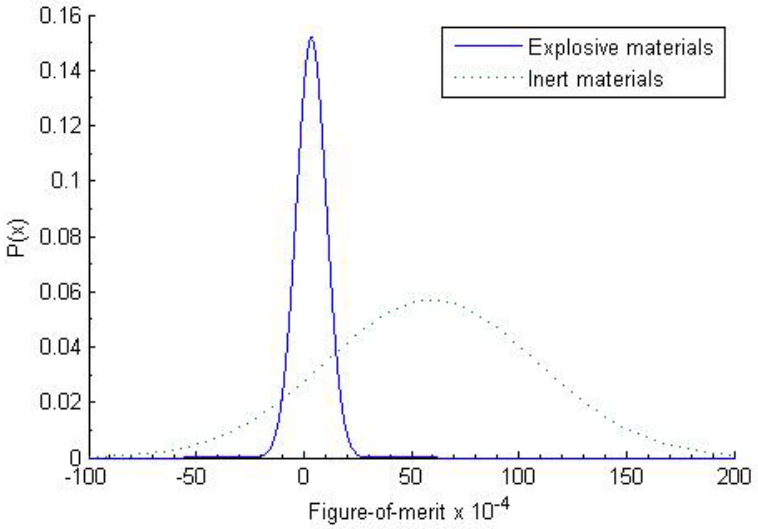

Figure 5.5 PDF comparing the figures-of-merit for two classes of materials, nitrogen-rich explosives and inert materials, with the AET.

the results show improvement with the 14.1-MeV neutron source compared to the ^{252}Cf neutron source. Therefore, only the 14.1-MeV source was focused on in remaining experiments.

5.3.3 Placement of the Sample in the XY-Plane

Let direct interrogation refer to the situation in which the center of the beam is aligned with the center of the target and let off-set interrogation refer to the situation in which the centers are off-set from each other. In these simulations, the neutron beam sometimes only partially overlapped the sample, similar to what occurs during target scanning in which a neutron beam sweeps across a fixed target. An average explosive sample was first placed completely in the path of the beam as in direct target interrogations and the response was found. Next, the sample was off-set from its initial position by 7.62 cm laterally (x-direction), such that the beam passed through only one-half of the sample. The results were examined to determine how the off-set affected responses (see Table 5.7). Recall these experiments used a perfectly collimated beam

Table 5.7 Average explosive response for direct and off-set interrogation.

Element	*Signature Energy (MeV)*	*Direct* ***R***	*σ(**R**)*	*Offset* ***R***	*σ(**R**)*
H	2.2232	3025.36	28.44	1501.15	20.57
C	1.2618	2778.59	72.24	1322.87	17.73
	3.6839	19002.5	49.41	7503.33	29.26
	4.439	52473.4	78.71	20924.2	48.13

	4.9453	2803.74	21.03	1175.7	13.76
N	1.6353	5562.65	27.26	2187.42	17.28
	1.8848	784.16	16.7	456.01	12.59
	2.3128	12630.5	39.16	4873.58	23.39
	3.3786	2790.68	22.05	1214.91	14.82
	3.8907	1565.38	18.32	708.7	12.47
	4.9151	2104.24	17.68	894.57	11.9
	5.1059	8322.06	33.29	3432.09	20.59
	5.2692	326.29	10.38	200.69	8.19
	6.4462	2186.43	17.27	934.4	11.77
	10.8291	72.51	3.04	31.98	2.05
O	0.8707	5564.46	45.07	2414.96	25.84
	2.1845	724.18	16.66	464.84	13.67
	6.1299	38620.5	65.66	15648.6	40.69
	6.9171	14082.2	42.25	5809.59	25.56
	7.1168	16205	45.37	6636.28	27.87

with radius 7.62 cm (3 in.). The sample had diameter 15.24 cm (6 in.) and height 20.752 cm (8.17 in.), with the beam passing through the entire width and height of the sample during direct interrogation. Because the optimal signature energies had not been identified at the time of this research, the twenty signature energies shown in Appendix D were used for these simulations.

As shown in Table 5.7, the responses when the sample was off-set relative to the beam are close to one-half the value of the normal responses. Therefore, the effect of the off-set was roughly linear. Also, scanning only part of an explosive target is similar to scanning a smaller explosive volume. This suggests that it may be possible to create templates based on either the explosive size or the amount of the target scanned by neutron beams. Ideally, templates will be made for discrete explosive sizes and a process similar to the one in section 5.4.2 will be applied.

Next, figure-of-merit results were calculated and are shown in Tables 5.8 and 5.9 using five explosives and five inert materials with the AET and the sample in the direct position and the off-set position. The scaling parameter β (in equations 3.3 and 3.5) was used first as 1

Table 5.8 Direct sample interrogation using AET to the find figures-of-merit.

Sample Material	ζ	$\sigma(\zeta)$	$f_-(3) = \zeta - 3\sigma(\zeta)$	$f_+(3) = \zeta + 3\sigma(\zeta)$
Aluminum	50846.50	96.15	50558.05	51134.95
Concrete	19323.51	59.27	19145.69	19501.33
Rubber	53580.62	98.70	53284.51	53876.72
Steel	49976.99	95.32	49691.02	50262.96
Wood	12435.84	47.55	12293.18	12578.49
Ammonium Nitrate	10371.72	43.43	10241.44	10502.00
Cyclonite (RDX)	401.90	8.55	376.25	427.54
Nitroglycerin	3335.10	24.63	3261.23	3408.98
PETN	2797.61	22.55	2729.95	2865.27
TNT	2689.02	22.11	2622.69	2755.36

Table 5.9 Off-set sample interrogation using AET with (a) β=1 (b) β=0.5 to the find the figures-of-merit.

(a)

Sample Material	ζ	$\sigma(\zeta)$	$f_-(3) = \zeta - 3\sigma(\zeta)$	$f_+(3) = \zeta + 3\sigma(\zeta)$
Aluminum	63822.36	112.98	63483.42	64161.30
Concrete	32954.93	81.19	32711.37	33198.48
Rubber	50655.77	100.65	50353.81	50957.73
Steel	64479.18	113.56	64138.50	64819.86
Wood	33006.83	81.25	32763.09	33250.58
Ammonium Nitrate	19013.38	61.67	18828.39	19198.38
Cyclonite (RDX)	16953.92	58.23	16779.23	17128.61
Nitroglycerin	18900.64	61.48	18716.19	19085.08
PETN	18032.62	60.05	17852.46	18212.78
TNT	19125.01	61.85	18939.47	19310.55

(b)

Sample Material	ζ	$\sigma(\zeta)$	$f_-(3) = \zeta - 3\sigma(\zeta)$	$f_+(3) = \zeta + 3\sigma(\zeta)$
Aluminum	54072.33	103.99	53760.35	54384.31
Concrete	18201.30	60.34	18020.30	18382.30
Rubber	47345.72	97.31	47053.79	47637.65
Steel	54900.28	104.79	54585.92	55214.64
Wood	12267.52	49.53	12118.93	12416.12
Ammonium Nitrate	7146.22	37.81	7032.80	7259.64
Cyclonite (RDX)	927.31	13.62	886.45	968.16
Nitroglycerin	2900.81	24.09	2828.55	2973.07
PETN	2271.20	21.31	2207.26	2335.14
TNT	2520.32	22.45	2452.97	2587.68

and then as 0.5. A β =0.5 value was chosen because the beam only interacted with one-half of the sample. No parameter other than β was altered in the analysis. The direct interrogation resulted in no false positives or false negatives with f_o=11,000. The off-set sample using the AET with β=1 required a larger cutoff value, f_o=25,000, but also had no false positives or false negatives. Finally, the off-set sample using the AET with β=0.5 and the same cutoff as the direct interrogation, f_o=11,000, had no false positives or false negatives. However, taking the ratio of the average explosive figure-of-merit and the average inert figure-of-merit, one finds that when β=1 is used the ratio is 0.38 and when β=0.5 is used the ratio is 0.08 for the data in Table 5.9. Therefore, with β=0.5 the average explosive and average inert figures-of-merit were much farther apart than the case with β=1, and thus results were improved. Clearly, judicious use of β may assist in template matching.

5.4 Simulations with the 14.1-MeV Source Involving Clutter

This section covers methods to deal with the problem of clutter in explosive-inert differentiation with a 14.1-MeV source. Methods of dealing with clutter examined include the following: templates that group clutter according to its density and an approach that uses tiers to group clutter according to its density and composition. Finally, clutter thickness is altered to observe the effect upon the responses.

5.4.1 Grouping Clutter by Density

The effects of clutter materials could be managed by making a template for each type of clutter material in front of RDX. However, this would require many templates to account for all possible clutter materials. As mentioned, excessive templates may lead to false positives occurring by chance. Therefore, it is desired to keep the number of templates as small as possible. Thus, a method was explored that requires fewer templates by grouping clutter materials according to their density.

Twenty-five inert materials were chosen for the simulations, with an effort made to choose common materials possessing diverse compositions. The experimental parameters specified in section 5.1 were used for the simulations. RDX was chosen for the explosive because it is a very common military explosive used in artillery shells, which often are transformed into IEDs.

Initially, twenty-five clutter materials were simulated while the sample material, RDX, was held constant. Next, twenty-five more simulations were performed, that used the same inert material for both the sample and the clutter. Combinations of differing inert sample and inert clutter materials were not considered. Thus, fifty simulations were performed. The twenty-five inert materials were separated into four groups based on density including very low density (VLD, 0-0.5 g cm^{-3}), low density (LD, 0.5-1.5 g cm^{-3}), medium density (MD, 1.5-3.0 g cm^{-3}) and high density (HD, 3.0-8.0 g cm^{-3}). Then, a template was generated for each density group, resulting in a VLD template, a LD template, a MD template and a HD template. This was accomplished by averaging the responses of RDX for each signature energy with inert clutter materials within the density range of the group.

Next, each of the four templates was applied to all fifty targets to calculate figures-of-merit and $f_{\pm}(1)$ values, using all templates on all targets. Responses and their standard deviations and the VLD, LD, MD and HD templates that were used to calculate these values are listed in Appendix E. Using the $f_{+}(1)$ values found from explosive targets, a cutoff value of $f_0 = 2,000$ was chosen. The false positive and false negative results are shown in Tables 5.10-5.13. Only the five N signature energies listed in Table D.3 were used in this analysis. Unit weight factors were used. It was found that when the signature energies from H, C, and O were included in templates the results became worse. This was because significant concentrations of H, C, and O are present in most common inert materials, and therefore interfere with HCO

signatures from an RDX sample. Significant concentrations of N, however, are found much more rarely in inert materials. Thus, this method capitalized on the relatively low N content of common inert materials and the relatively high N content of nitrogen-rich explosives.

Table 5.10 Results for the VLD clutter group, density 0– 0.5 g cm^{-3}.

VLD Inert Material	*Density (g cm^{-3})*	*False Positives* (Inert/Inert)	*False Negatives* (RDX/Inert)
Air	0.001205		
Polyurethane (foam)	0.10		

Table 5.11 Results for the LD clutter group, density 0.5– 1.5 g cm^{-3}.

LD Inert Material	*Density (g cm^{-3})*	*False Positives* (Inert/Inert)	*False Negatives* (RDX/Inert)
Ethanol	0.80		
FertA (nitrogenous)	0.81	X	X
FertB (non-nitrogenous)	0.99		
Gasoline	0.68		
Nylon	1.14	X	
Petroleum	0.97		
Plexiglass	1.19		
Polyethylene	0.93		
Rubber	0.92		
Soy	0.72		
Water	1.00		
Wax	0.93		
Wood	0.75		

Table 5.12 Results for the MD clutter group, density 1.5– 3.0 g cm^{-3}.

MD Inert Material	*Density (g cm^{-3})*	*False Positives* (Inert/Inert)	*False Negatives* (RDX/Inert)
Aluminum	2.70		
Bricks	1.80		

Carbon (Graphite)	1.70
Concrete	2.35
Glass	2.40
Granite	2.73
Salt	2.18
Soil	1.61

Table 5.13 Results for the HD clutter group, density 3.0–8.0 g cm^{-3}.

HD Inert Material	*Density (g cm^{-3})*	*False Positives* (Inert/Inert)	*False Negatives* (RDX/Inert)
Steel	7.85		
Copper	8.92		

It was found that using a cut-off value of $f_0 = 2,000$, RDX was identified in all but one target in which it was present (the $f_+(1)$ values of explosive targets were below 2000). The correct template for each density group differentiated RDX with clutter materials having a density within the group, for all targets except one. For example, the VLD template identified RDX with each of the VLD clutter materials air and polyurethane. Thus, each template filtered out the targets for which it was designed. The only false negative occurred with the LD template, with FertA as clutter in front of cyclonite for which the $f_+(1)$ value was 13,160. There were only two false positives, FertA (as sample and clutter) and Nylon (as sample and clutter), with $f_+(1)$ values 715 and 786, respectively. Both of these inert materials contain N (see Appendix C). For example, FertA is composed of 0.36 weight percent N. Because only N signatures were used, it is expected that inert materials containing substantial amounts of N may yield false positives or false negatives with these templates. Therefore, to prevent false negatives, this technique would require a N response size cutoff to "flag" any nitrogen-rich target as being a possible IED. Thus, unknown targets having a N response exceeding a specified N cutoff response, would be labeled as suspect explosive targets. The next section helps overcome the problem of false positives with nitrogen containing clutter by adding the signature energies of H, C, and O to discriminate against N containing inert targets while still accounting for the effects of clutter.

5.4.2 Grouping Clutter by Composition and Density with a Tiered Filter Approach

In the last section it was shown that the number of templates may be reduced by grouping inert clutter materials by a shared characteristic of the materials, specifically, their density. Furthermore, density is not the only characteristic by which materials can be grouped; composition is another such characteristic. In this section, it will be shown that grouping clutter by density and composition is superior for explosive-inert differentiation than grouping clutter only by its density.

Clearly, as shown in the last section, clutter density is a variable that should be accounted for in templates that deal with clutter. Also, because the signature energies are based on responses from H, C, N and O, templates should account for various concentrations of these elements within clutter materials. For example, a clutter material composed of H will cause the 2.2232-MeV H response to increase. However, explosive templates typically contain relatively low H responses. Therefore, a large figure-of-merit will result for the H signature when templates are applied to the explosive target with H-rich clutter. This may cause a false negative, depending upon what value is used for f_o. Similarly, the same effects from the clutter can occur for the C, N and O signatures. Therefore, templates should be made to incorporate a contribution to the signatures by a clutter containing H, C, N, or O. Let any reduction of the gamma-ray signatures by an element within a clutter material be defined as **attenuation**. Density has been found to affect attenuation; however, it is already accounted for in a method described in the last section. The atomic number of the clutter material also affects the attenuation of the signature energies.Therefore, the effects of elements differing from HCNO are considered in the following section.

5.4.2.1 Filler Elements

Before an explanation of the tiered filter approach is considered, it is important to define what is meant by a filler element.

- **Filler Element (FE)** – An element of atomic number Z' chosen to represent attenuation caused by a group of elements in the periodic table close in atomic number to Z'.

To help minimize the number of templates, it was desired to group elements close in atomic number together and represent attenuation caused by elements within the group by the attenuation caused by an element near the center of the group. Simulations were performed to

test whether attenuation by a FE was similar to attenuation caused by other elements near in atomic number to Z', assuming a constant density.

First, elements having atomic numbers from 1 to 82 were divided into four groups based on the mass of their nuclei. The ratio between the masses of a Z-1 nuclei and a Z nuclei increases as atomic number increases. For example, the ratio of the mass of a H (Z=1) nucleus and a He (Z=2) nucleus is 0.25; however, the ratio of the mass of a K (Z=19) nucleus and a Ca (Z=20) nucleus is 0.98. Therefore, groups containing elements low in atomic number were chosen to be smaller than groups containing elements higher in atomic number. Noble gases were excluded because they are not present in typical clutter materials. Also, signature elements (HCNO) were not included in the study. They are incorporated into the tiered filter approach explained next. The ranges selected for the four groups are shown in Table 5.14. Next, every element at the edges of each group was simulated as the clutter material. The experimental setup from section 5.1 was used with RDX as the sample. The clutter was composed only of one element and had a constant density of 1 g cm^{-3}. Finally, the fluences of the signature energies from RDX with elements at the edges of each group used for clutter materials were examined. The fluences for the 2.3128-MeV N signature energy with clutter composed of elements at the edges of each group are shown in Figure 5.6. Overall, the fluence was attenuated by lower atomic number elements more strongly that higher atomic number elements (with density constant). These results indicate that the 2.3128-N fluence from the RDX sample appears not to be greatly influenced for clutter materials of constant density made of elements within a given group, except for the first group. Therefore, four FEs were chosen which had atomic numbers near the middle of each group; these elements are identified in Table 5.14. These FEs were used to represent, though not precisely, the attenuation (related to atomic number) from any clutter material composed of elements having atomic numbers within the groups shown in Table 5.14.

Table 5.14 FEs chosen to represent four atomic number groups.

	FE	*Group Atomic Number Range*
Group 1	Lithium	3-5 (Li–B)
Group 2	Fluorine	6-9 (C-F)
Group 3	Phosphorous	11-17 (Na-Cl)
Group 4	Chromium	19-82 (K-Pb)

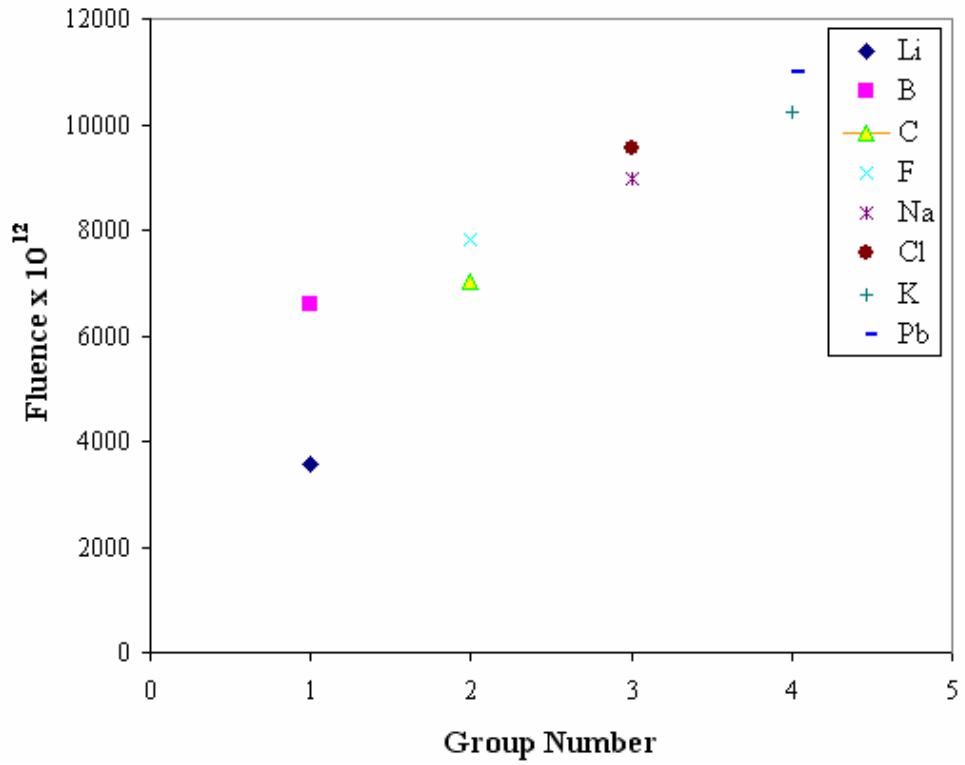

Figure 5.6. Comparison of the fluences of the 2.3128-N signature from RDX in the presence of clutter containing elements at the edges of each group shown in Table 5.14.

5.4.2.2 Tiered Filter Approach

Next, templates were formed that incorporated the effect upon the responses of RDX from clutter materials varying in density and HCNO and FE composition. A systematic approach was implemented that employs filtering unknown targets in tiers or stages. Accordingly, the tiered filter approach requires a target to match several templates before it is classified as either an explosive, inert or unknown material (inconclusive test).

The simulation procedure was the same as for the last section. However, the number of clutter materials was increased to fifty. Thus, one-hundred simulations were performed with fifty inert/inert (sample/clutter) and fifty RDX/inert (sample/clutter). No simulations involved combinations of inert materials. One of the fifty clutter materials used was not a true inert but was instead the explosive, TNT, which was treated as "inert" clutter to determine the effect. Tables 5.20 and 5.21 list the materials used as inert samples and clutter. The responses of these target simulations were analyzed using a tiered filter approach, described below.

Four tiers were used in the approach. The first tier, depicted in Figure 5.7, was designated to identify x, where x indicates the density template group from among the following density ranges:

- **Very Low Density (VLD)** (0.0 – 0.5 g cm^{-3})
- **Low Density (LD)**, (0.5 – 1.5 g cm^{-3})
- **Medium Density (MD)**, (1.5 – 3.0 g cm^{-3})
- **High Density (HD)**, (3.0 – 11.0 g cm^{-3})

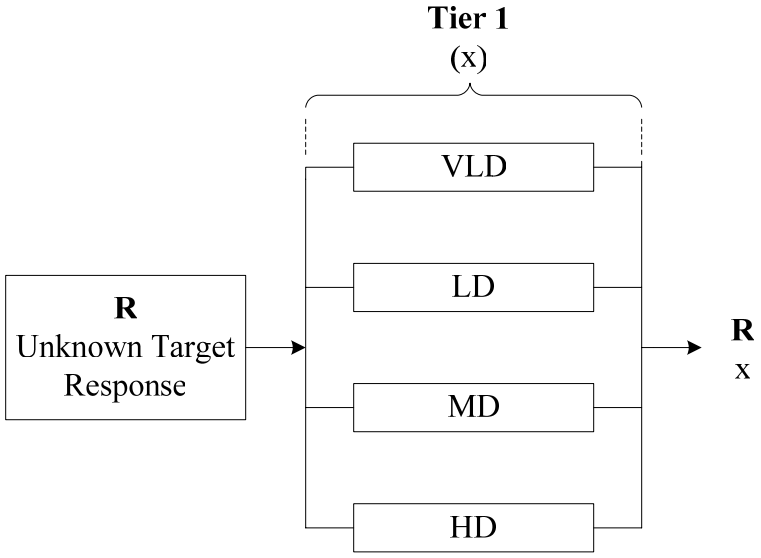

Figure 5.7 Tier 1: density template groups.

Each density template group contained four sub-template (ST) groups that were grouped according to the clutter's HCNO composition. This was the second tier of the approach, illustrated in Figure 5.8, which identifies y, where y indicates the ST group (H STs, C STs, N

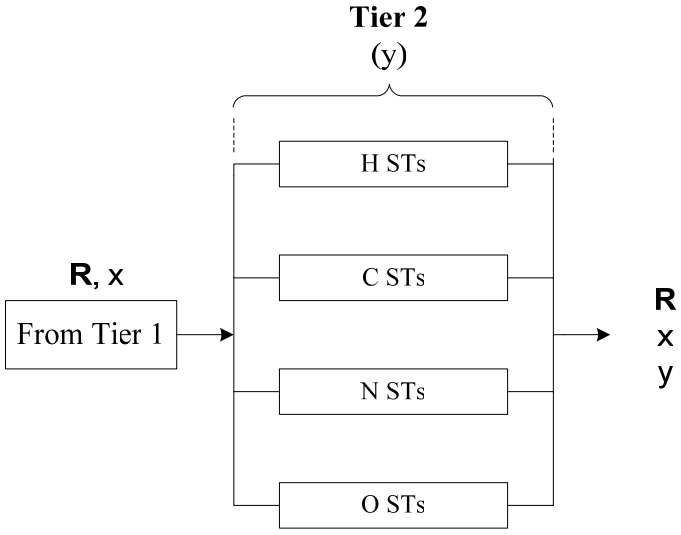

Figure 5.8 Tier 2: ST groups.

STs or O STs). The third tier, shown in Figure 5.9, contained templates for each ST group within a density template group and was designated by z, where z indicates the template number.

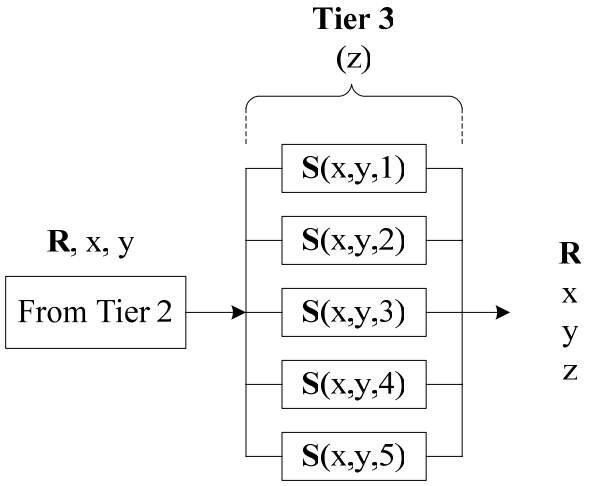

Figure 5.9 Tier 3: templates.

Templates were made by performing simulations with artificial clutter materials in MCNP for particular HCNO and FE concentrations and densities.

Perl was used to generate many input files for artificial clutter materials and a RDX sample. The responses of these input files were used to form templates. These templates had the following characteristics. A template containing responses from RDX using only one of the signature elements H, C, N or O was paired with only one FE in the clutter. Only one FE was used for each density template group. This was to limit the number of templates and prevent unrealistic templates with FEs of unnatural densities (ex. Li in HD template group). The density template groups for which each FE was used are shown in Table 5.15.

Table 5.15 FE used for each density template group.

Density Template Group	FE used for the Group
VLD	Lithium
LD	Fluorine
MD	Phosphorous
HD	Chromium

Concentrations and densities of HCNO and FEs were divided into discrete groups. For each group, the concentration of an element ranged from 0-25%, 25-50%, 50-75% and 75-100% of the clutter composition. The midpoint of each concentration group was used to represent that

group (ie. for group 0-25%, 12.5% concentration was used). Similarly, the midpoint for each density template group was also used to represent the density template group (ie. VLD, 0.0 – 0.5 g cm^{-3} implies density = 0.25 g cm^{-3}). Table 5.16 demonstrates the concentration parameters (midpoints of the group ranges) governing the clutter compositions used for simulating templates. The number and specificity of the templates may be adjusted by altering the range of the concentration or density groups. The FE completes the remaining percentage of either H, C, N, or O composition of the clutter such that it totals 100%. Additionally, for templates where either the H, C, N, or O composition is 0%, the FE composes 100% of the clutter composition. Table 5.17 shows five O and Li concentrations used to make the five templates for the O ST group and VLD template group. Other templates in each ST group and density template group were made in a similar fashion.

Table 5.16 Template parameters.

S(x,y,z)	**H%, C%, N% or O%**	**FE%**
S(x,y,1)	0	100
S(x,y,2)	12.5	87.5
S(x,y,3)	37.5	62.5
S(x,y,4)	62.5	37.5
S(x,y,5)	87.5	12.5

Table 5.17 Five clutter compositions that were used to create the five templates for the VLD template group (0.25 g cm^{-3}) and O STs group.

S(x,y,z)	**O%**	**Li%**	**Density (g cm^{-3})**
S(VLD, O STs, 1)	0	100	0.25
S(VLD, O STs, 2)	12.5	87.5	0.25
S(VLD, O STs, 3)	37.5	62.5	0.25
S(VLD, O STs, 4)	62.5	37.5	0.25
S(VLD, O STs, 5)	87.5	12.5	0.25

Finally, the fourth tier involved calculating figures-of-merit and $f_{\pm}(1)$ values from the responses of each template and the responses from each target. The total number of templates contained within the approach is shown below and all templates were applied to all targets.

Total Template Number:

(4 density template groups) × (4 ST groups) × (5 templates within each group) = **80 templates**

Judiciously, cutoff values were chosen using the $f_{+}(1)$ values for explosives targets. Each ST group within each density template group had a corresponding cut-off value, designated by f_{yo}^{x}, as shown in Table 5.18. The cut-off values used for analysis are shown in Table 5.19.

Table 5.18 ST group cutoff values.

	VLD	**LD**	**MD**	**HD**
H STs	f_{Ho}^{VLD}	f_{Ho}^{LD}	f_{Ho}^{MD}	f_{Ho}^{HD}
C STs	f_{Co}^{VLD}	f_{Co}^{LD}	f_{Co}^{MD}	f_{Co}^{HD}
N STs	f_{No}^{VLD}	f_{No}^{LD}	f_{No}^{MD}	f_{No}^{HD}
O STs	f_{Oo}^{VLD}	f_{Oo}^{LD}	f_{Oo}^{MD}	f_{Oo}^{HD}

Table 5.19 Cutoff values used for each ST group.

	VLD	**LD**	**MD**	**HD**
H STs	$f_{Ho}^{VLD} = 1000$	$f_{Ho}^{LD} = 250000$	$f_{Ho}^{MD} = 6000$	$f_{Ho}^{HD} = 1000$
C STs	$f_{Co}^{VLD} = 4000$	$f_{Co}^{LD} = 11500$	$f_{Co}^{MD} = 34000$	$f_{Co}^{HD} = 3000$
N STs	$f_{No}^{VLD} = 1000$	$f_{No}^{LD} = 2500$	$f_{No}^{MD} = 2000$	$f_{No}^{HD} = 3500$
O STs	$f_{Oo}^{VLD} = 1000$	$f_{Oo}^{LD} = 12000$	$f_{Oo}^{MD} = 10000$	$f_{Oo}^{HD} = 18000$

Next, the explosive elemental content (EEC) is introduced that assures that a target matches the H, C, N or O content at least one of the templates to an accuracy given by the cut-off value used. Using the cut-off value of the ST group and the $f_{\pm}(1)$ values from templates within the group, a logic test was performed. The logic test returns one of three values for the EEC. If an EEC value of -1 exists for each ST group (H STs, C STs, N STs and O STs) within a density template group, this implies an **explosive**. If an EEC value of 1 exists for each ST group and there are no EEC values of -1 or 0 in found in each ST group, this implies an **inert**. Finally, if the EEC value is 0 for any ST group and there are no EEC values of -1 in the ST group, the test is **inconclusive**. Figure 5.10 demonstrates the fourth tier of the approach, which performs the EEC logic test. Finally, Figure 5.11 demonstrates the sequence of the tiered filter approach combining all four tiers for a specific case using x=VLD, y=H STs and z=1, which results in an EEC value of -1 ($f_{-}(1,1) < f_{Ho}^{VLD}$).

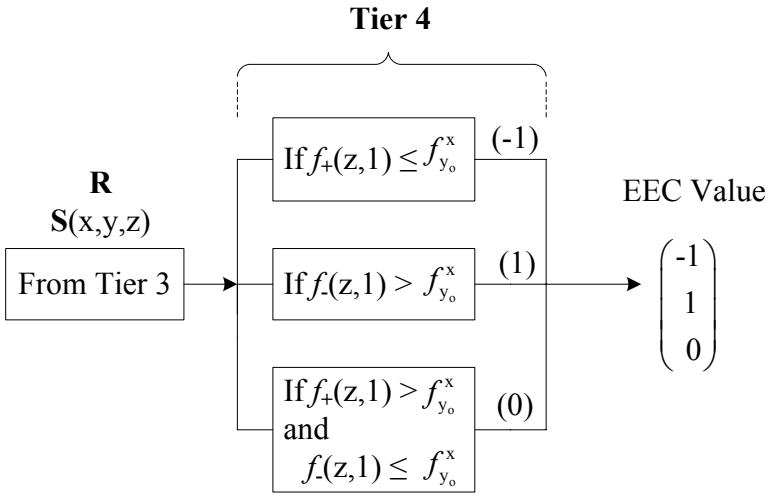

Figure 5.10 Tier 4: EEC logic test.

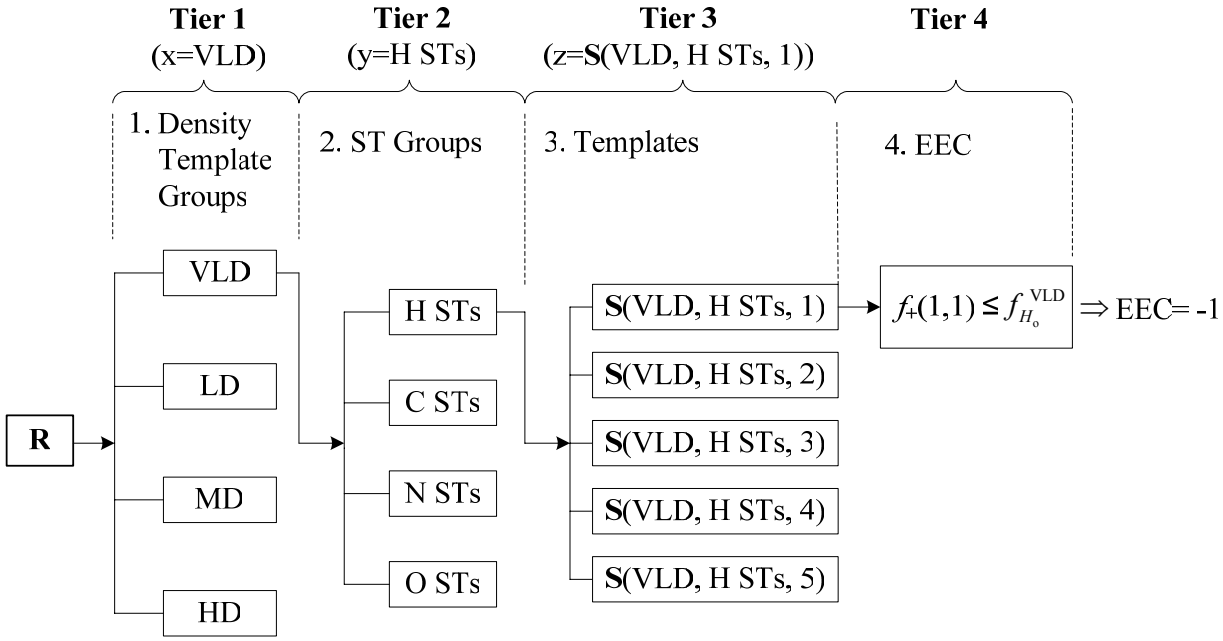

Figure 5.11 Specific example applying the tiered filter approach for VLD template group, H ST group and the 1st H template, resulting in an $f_+(1,1)$ value ≤ than the correct cutoff.

The results from the tiered filter approach were promising. Tables 5.20 and 5.21 show the false positives and false negatives found in the experiments using the tiered filter approach with cut-off values shown in Table 5.19. In this experiment, 1 H, 1 C, 5 N and 2 O signatures, listed in Table D.4, were used with unit weight factors. The optimal signature energies had not been found when the experiments were performed, but the majority of them, including at least one for each element, were used in the experiment (found by trial and error by using signatures that gave the best results).

Table 5.20 Results using a tiered filter approach.

	Inert Materials	Density ($g\ cm^{-3}$)	False Positives (Inert/Inert)	False Negatives (RDX/Inert)
1	**Air**	0.001205		
2	**Propane**	0.0019		
3	**Cyanurate**	0.0321		
4	**Styrofoam**	0.1		
5	**Polyurethane (foam)**	0.1		
6	**Cherry Wood**	0.43		
7	**Ash**	0.641		
8	**Gasoline**	0.6837		
9	**Cardboard**	0.689		
10	**Soy**	0.721		
11	**Wood**	0.75		
12	**Ethanol**	0.8		
13	**Soap**	0.801		
14	**FertA (with nitrogen)**	0.81	X	
15	**Rubber**	0.92		
16	**Polyethylene**	0.93		
17	**Wax**	0.93		
18	**Petroleum**	0.973		
19	**FertB (non nitrogenous)**	0.99		
20	**Water**	0.998		
21	**Tissue**	1.04		
22	**Polystyrene**	1.06		
23	**Antifreeze**	1.1132		
24	**Nylon**	1.14		
25	**Herbicide 1**	1.17	X	
26	**Herbicide 3**	1.187		
27	**Plexiglass**	1.19		

Table 5.21 Results using a tiered filter approach.

	Inert Materials	Density ($g\ cm^{-3}$)	False Positives (Inert/Inert)	False Negatives (RDX/Inert)
28	**Lucite**	1.19		
29	**Herbicide 2**	1.25		
30	**Sugar**	1.54		
31	**Cotton**	1.55		
32	**Soil**	1.6104		
33	**TNT (treated as an inert)**	1.654	X	
34	**Carbon (graphite)**	1.7		
35	**Borax**	1.73		
36	**Bricks**	1.8		
37	**Potassium Hydroxide**	2.044		
38	**Rock Salt**	2.18		
39	**Concrete**	2.35		
40	**Limestone**	2.35		
41	**Glass**	2.4		
42	**Ceramic**	2.403		
43	**Al**	2.7		
44	**Granite**	2.729		
45	**Titanium**	4.54		
46	**Zirconium**	6.506		
47	**Steel**	7.85		
48	**Nickel**	8.9		
49	**Copper**	8.92		
50	**Lead**	11.35		

It was found that there were 2 false positives, FertA and Herb1, and no false negatives. Both FertA and Herb1 were in the LD template group and they each had $f_{+}(1)$ values below the cutoff values corresponding to each ST group and therefore were false positives. As shown in

Table 5.19, the cutoff values for the LD template group were f_{Ho}^{LD}=250,000 f_{Co}^{LD}=11,500, f_{No}^{LD}=2500 and f_{Oo}^{LD}=12,000 for H, C, N and O ST groups. FertA had minimum $f_{+}(1)$ values (for 5 STs in each ST group) 4734.7 (H), 2934.3 (C), 901.3 (N) and 3229.0 (O) for the LD template group H, C, N and O STs. Herb1 had minimum $f_{+}(1)$ values (for 5 STs in each ST group) 334.3 (H), 658.5 (C), 1886.0 (N) and 2061.5 (O) for the LD template group H, C, N and O STs. TNT as the sample and clutter was identified with the MD template group STs (the correct set for TNT, density 1.654 g cm^{-3}), with minimum $f_{+}(1)$ values 3203.5 (H), 14,708.4 (C), 665.4 (N) and 3074.5 (O), which were below the corresponding ST cutoff values for the MD template group. TNT was not counted as a false positive because it was an explosive.

The tiered filter approach offers several advantages over earlier template matching techniques. Primarily, both composition and density are incorporated. Secondly, few templates are needed to characterize a large clutter material parameter space. A wide density range of 0-11 g cm^{-3} was used, and elements of a wide range in atomic number were included in the material compositions. Thirdly, the method achieved a high specificity of 96% and a perfect sensitivity of 100% (equations 3.7 and 3.8). Fourth, the cutoff values within a ST group are adjustable. Fifth, it incorporates a minimum nitrogen response by requiring a match within the nitrogen templates, and similarly requires minimums for elements H, C and O. The approach also effectively filters out many nitrogen containing clutter materials as shown in Table 5.22. Additionally, the

Table 5.22 Nitrogen-containing clutter materials.

Inert Material	Nitrogen Atom Fraction	Filtered Effectively
Air	0.784437	Yes
Polyurethane	0.076459	Yes
Cyanurate	0.06900	Yes
Herb2	0.06667	Yes
Herb3	0.178572	Yes
Tissue	0.02600	Yes
Nylon	0.052632	Yes
Herb1	0.076924	No
FertA	-0.3600 (weight fraction)	No

explosive TNT was identified as explosive when it was used as “inert” clutter. Finally, the tiered filter approach may be programmed into an algorithm and thus be automated.

5.4.3 The Effects of Clutter Thickness on Response Size

In the preceding sections, clutter thickness was constant at 10 cm. In these simulations, the variable of clutter thickness was manipulated. The goal was to consider the maximum clutter thickness for a material in each density group in which an informative response may be detected from the RDX sample. The 14.1-MeV source was used. Four different inert clutter materials were simulated and the case with no clutter material, with one representing each density group including foam, polyethylene, concrete , steel and a vacuum. The target configuration was the same as section 5.1, with the exception of the clutter dimensions and detector and sample placement, with the configuration shown in Figure 5.12. The clutter material was first increased

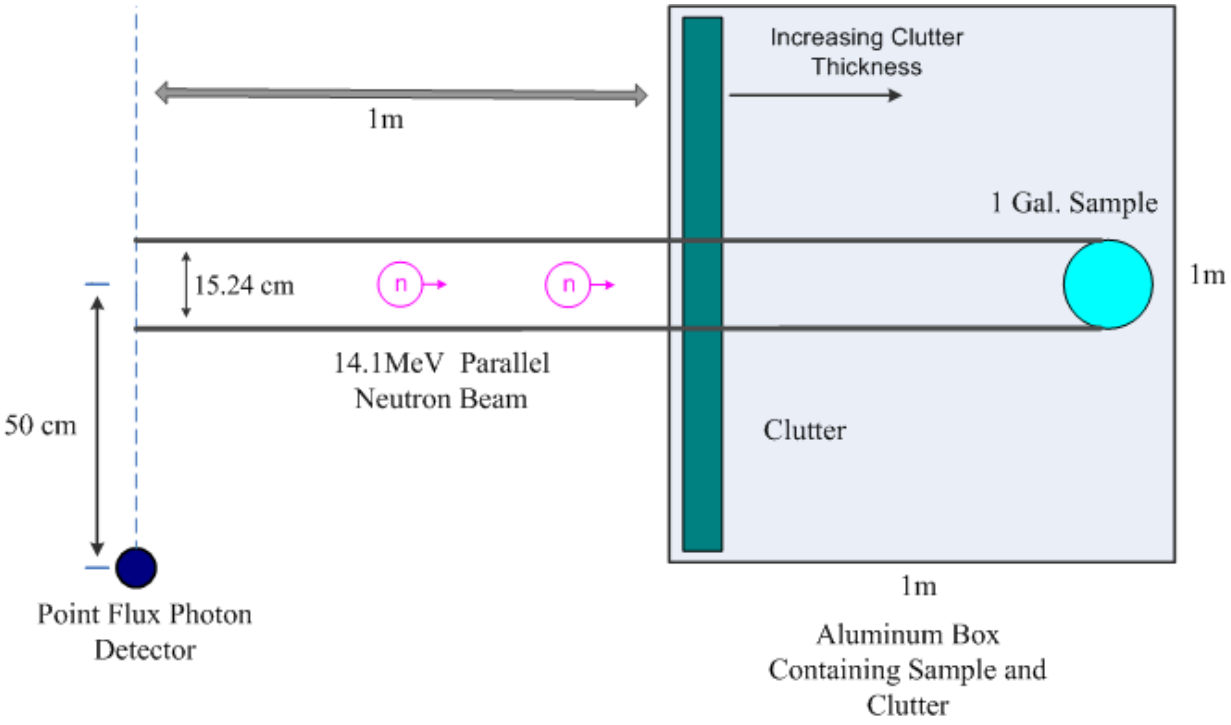

Figure 5.12 Geometry for simulations in which clutter thickness was increased.

in height and length, such that it occupied a larger area in the xz-plane inside the target. Thus, the gamma rays from the sample must pass through the clutter volume for detection. Next, the clutter material was increased incrementally in thickness from 2.5 cm to 32.5 cm, as shown in Figure 5.12. The responses for an optimal N signature, 2.3128 MeV, with non-nitrogenous inert clutter as a function of clutter thickness were plotted, as shown in Figure 5.13.

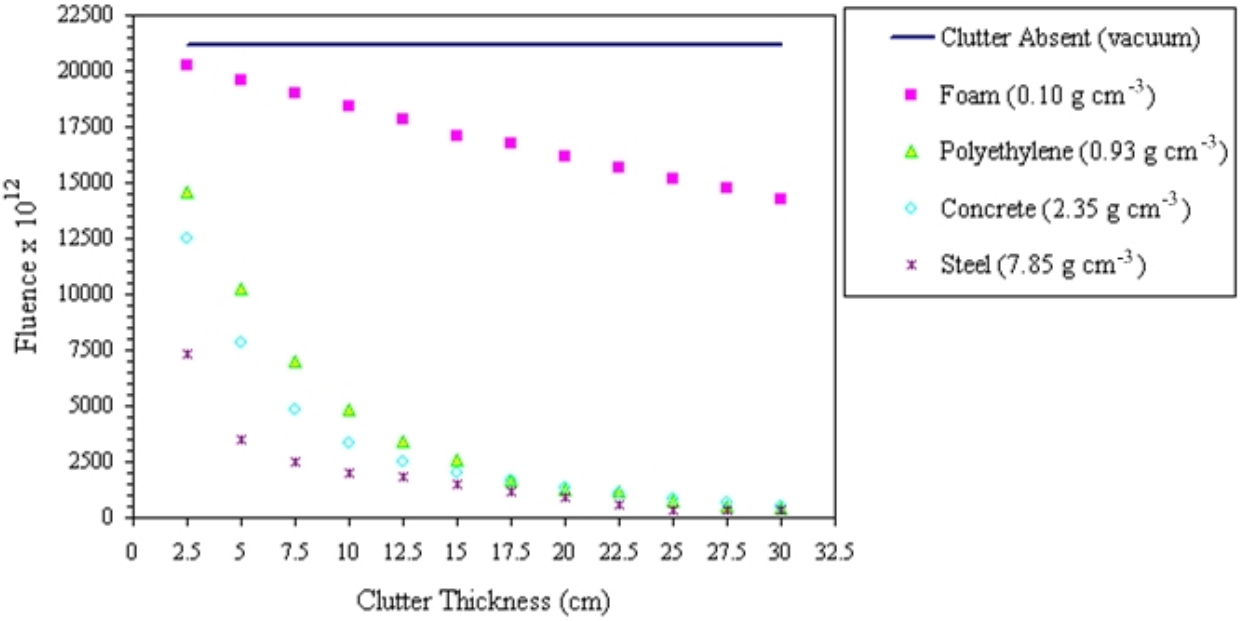

Figure 5.13 Responses from an RDX sample with four clutter materials and clutter absent as a function of clutter thickness for the 2.3128-MeV inelastic-scatter N signature.

Figure 5.13 clearly shows that large thicknesses of the VLD clutter material (foam) poses little problem for detection, and detection of significant responses may occur with thicknesses up to and beyond 25 cm. The LD and MD clutter materials (polyethylene and concrete) attenuate the response at much sooner thicknesses, but detection should be possible with thicknesses of 12.5-15 cm. The HD inert clutter material (steel) attenuates the response very quickly with detection only likely with clutter thickness less than 12.5 cm. Clearly, templates dealing with thickness will be needed to assist in differentiation.

The results of this study reaffirmed that altering clutter thickness and clutter density affect the RDX response. It is suggested that templates be made for targets at discrete thicknesses, and the scaling factor, β, be applied to interpolate. Results also suggest that differentiation may not be possible through very thick clutter, depending on the density of the clutter. Fortunately, with thick clutter, particularly very dense thick clutter, the danger posed by an IED detonation is minimized through absorption of the blast energy in the clutter. Therefore, it is less critical to identify heavily shielded explosives because they pose less danger. Additionally, this reduces the probability that thick explosive shielding will be used by terrorists.

CHAPTER 6 - Conclusions and Future Work with SBRS

6.1 Discussion and Conclusions

A shielding design has been simulated for producing a collimated beam from a D-T neutron generator, which emits 14.1-MeV neutrons isotropically. Estimated dose rates are below 2 mrem hr^{-1} at all points tested outside the laboratory rooms. A neutron interrogation technique using fast and thermal neutron analysis with SBRS template matching has been demonstrated. The SBRS method was demonstrated with bare and shielded explosives. The results suggest use of a D-T neutron generator, with 14.1-MeV neutrons and a flux of 10^{11} n s^{-1}, coupled with HPGe detectors, because of good efficiency and high energy resolution, for nitrogen-rich explosive interrogation. The research isolated 9 optimal signature energies with little or no interference and good probability for detection for the elements H, C, N, and O, which compose nitrogen-rich explosives. Simulations demonstrated that a neutron beam is potentially a powerful tool for explosive-inert differentiation because of its ability to penetrate shielding materials.

Clutter in front of explosives was found to be a non-trivial problem. However, simulations demonstrated that explosives may be identified with good specificity and sensitivity, despite the presence of clutter of a fixed thickness (10 cm) in front of the explosives by constructing sub templates based on a finite number of density and composition variables. A tiered filter template matching approach, portrayed in section 5.4.2, was shown to be reasonably successful at dealing with the effects of clutter. Further work remains to form a more general template library, specifically with incorporating the clutter thickness, explosive volume, and target distance into templates. However, a process to keep the number of templates finite has been demonstrated. While neutron interrogation may be coupled with X-ray or trace methods, it has been found to be capable of explosive-inert differentiation independently. This is because neutrons are penetrating and can identify targets by their stoichiometry, while X-ray and trace detection methods fail to do so as effectively.

In conclusion, SBRS using neutron interrogation merits attention and has advantages over present X-ray or trace detection methods particularly with detection of explosives in large volume targets. Simulations have demonstrated that SBRS technology can be used to differentiate fixed-geometry targets containing a one-gallon IED (RDX) shielded by 10 cm of clutter at distance of at least 1 m with good sensitivity and specificity. This was accomplished for

an extensive variety of common material compositions used for clutter and inert materials. In section, 5.4.2, RDX was differentiated in all examined cases with only 2 false positives.

6.2 Build a Field Prototype to Experimentally Verify Results

Currently, work with SBRS involves building an experimental laboratory prototype to conduct field tests. The experimental prototype will involve a 14.1-MeV D-T neutron generator, a two-dimensional translation target stage and many types of targets. Experimental research should be performed to confirm the conclusions reached by simulations. Specifically, the tiered filter approach should be implemented experimentally to test its validity. A photon interrogation source and neutron counters may be added to assist interrogation. Scanning of targets should be tested with an experimental system to determine the time required for SBRS to identify IEDs. Finally, the technology must be streamlined and shielding materials reduced in preparation for field or checkpoint implementation. Ideally, SBRS will eventually become portable or truck mounted.

6.3 Further Refinements to the Template Matching Method

An experimental template library should be created. Additionally, the tiered filter approach should be tried with combinations of inert clutter materials. Characteristics including clutter thickness, target distance and explosive volume should be incorporated into the tiered filter approach. It may be possible to manage clutter thickness by adding another tier in the approach shown in section 5.4.2, but this must be shown. Variable target distances and explosive volumes might be accounted for by using the scaling factor β already contained within the figure-of-merit approach to create another tier. Templates may be generated for discrete distances, and the scaling factor β may be applied to interpolate the response size in between distances. This may be accomplished by using a rangefinder coupled with control software. Also, the method described in section 5.4.2 should be programmed as an algorithm in control software, to make the process automated. Ultimately, SBRS has been shown in simulations to be capable of differentiating explosive targets with good sensitivity and good specificity, but requires further development to effectively implement in a field environment.

References

Adelphi, "Neutron Systems," San Carlos, California, 2005. <http://www.adelphitech.com/products/neutrons_systemsMain.html>

Buffler, A. "Contraband Detection Using Fast Neutrons," *Radiation Physics and Chemistry*, Department of Physics, University of Cape Town, Vol. 71, pp. 853-861, 2004.

Correa, J.E., "The Dog's Sense of Smell," Food and Animal Sciences, Alabama A&M University, July 2005. <http://www.aces.edu/pubs/docs/U/UNP-0066/>

Dunn, W.L., K. Banerjee, A. Allen, J. van Meter, "Feasibility of a method to identify targets that are likely to contain conventional explosives," *Nuclear Instruments and Methods in Physics Research B*, Vol. 263, pp. 179-182, 2007. (a)

Dunn, W.L., R. Brewer, K. Loschke, J. Lowrey, "Radiation Interrogation Using Signature Analysis for Detection of Chemical Explosives," *Proc. IEEE Conference on Technologies for Homeland Security: Enhancing Critical Infrastructure Dependability*, Boston, MA, 16-17 May, 2007, pp. 7-12. (b)

Dunn, W.L., C.J. Solomon, K.W. Loschke, D.B. Bradley, W.B. Gilboy, "Ionizing Photon Methods for Standoff Bomb Detection," *Nuclear Instruments and Methods in Physics Research A,* Vol. 580**,** 778-781, 2007. (c)

Furstenberg, R., C.A. Kendziora, J. Stepnowski, S.V. Stepnowski, M. Rake, M.R. Papantonakis, V. Nguyen, G.K. Hubler, R.A. McGill, "Stand-off Detection of Trace Explosives Via Resonant Infrared Photothermal Imaging," *Applied Physics Letters*, Vol. 93, 224103, 2008.

Garroway, A.N., M.L. Buess, J.B. Miller, B.H. Suits, A.D. Hibbs, G.A. Barrall, R. Matthews, L.J. Burnett, "Remote Sensing by Nuclear Quadrupole Resonance," *IEEE Transactions on Geoscience and Remote Sensing*, Vol 39, No. 6, 2001.

Group T-16 (Nuclear Physics), "Neutron Data," *Theoretical Division of the Los Alamos National Laboratory,* 1998-2007. <http://t2.lanl.gov/data/neutron7.html>

Harding, G., "X-ray Scatter Tomography for Explosives Detection," *Radiation Physics and Chemistry*, Vol. 71, Elsevier, pp. 869-881, 2004.

Harper, R.J., K.G. Furton, Biological Detection of Explosives in Counterterrorist Detection Techniques of Explosives, J. Yinon, Elsevier, Netherlands, pp. 395-431, 2007.

Hussein, E.M., E.J. Waller, "Review of one-side approaches to radiographic imaging for detection of explosives and narcotics," *Radiation Measurements*, Vol. 29, No. 6, pp. 581-591,1998.

Iraq Coalition Casualty Count, June 2008, Deaths Caused by IED, 1 July 2008. <http://icasualties.org/oif/>

Inert Explosive Training Products, "Inert, 122mm Replica Artillery Shell IED with Pressure Plate (Hacksaw Blades)," 2009. <http://www.inertproducts.com/inc/sdetail/2946>

Jimenez, A.M., M.J. Navas, "Chemiluminescence Detection Systems for the Analysis of Explosives," *Journal of Hazardous Materials*, Vol. 106A, pp. 1-8, 2004.

Jimenez, A.M., M.J. Navas, Detection of Explosives by Chemiluminescence in Counterterrorist Detection Techniques of Explosives, J. Yinon, Elsevier, Netherlands, pp. 1-39, 2007.

Koltick, D., Y. Kim, S. McConchie, I. Novikov, I. Novikov, M. Belbot, G. Gardner, "A neutron based vehicle-borne improvised explosive device detection system," *Nuclear Instruments and Methods in Physics Research B*, Vol. 261, pp. 277-280, 2007.

Kuznetsov, A., A. Evsenin, MS-SRIP – Microwave System for Secret Standoff Inspection of People in Stand-off Detection of Suicide Bombers and Mobile Suspects, H. Schubert and A. Rimski-Korsakov, Springer, pp. 5-10, 2006.

Kuznetsov, A.V., O.I. Osetrov P., M. Stancl, Detection of Improvised Explosives (IE) and Explosive Devices (IED) in Detection and Disposal of Improvised Explosives, H. Schubert and A. Kuznetsov, Springer, Netherlands, pp. 7-25, 2006.

Lacey, R.J., "Why is it that Neutron Based Systems have not been Implemented?" *International Atomic Energy Agency*, Padova, Italy, 2007.

Lanza, R.C., Neutron Techniques for Detection of Explosives in Counterterrorist Detection Techniques of Explosives, J. Yinon, Elsevier, Netherlands, pp.131-155, 2007.

Marolda, E.J., "Water Mine Warfare in South Vietnam," Naval Historical Center, Washington, D.C. 2003. <http://www.history.navy.mil/wars/vietnam/minesouthviet.htm>

Miller, J.B., Nuclear Quadrupole Resonance Detection of Explosives in Counterterrorist Detection Techniques of Explosives, J. Yinon, Elsevier, Netherlands, pp. 157-198, 2007.

Mines Action Canada, "Landmine Monitor Report 2008: Toward a Mine-Free World," 2008. <http://www.icbl.org/lm/2008/es/landmine_casualties_and_survivor_assistance.html>

Molnar, G. L., Handbook of Prompt Gamma Activation Analysis with Neutron Beams, Kluwer Academic Publishers, Boston, London, 2004.

Mostak, P., M. Stancl, IEDs Detection by Existing Detection Techniques in Detection and Disposal of Improvised Explosives, H. Schubert and A. Kuznetsov, Springer, Netherlands, pp. 33-41, 2006.

National Research Council, Existing and Potential Standoff Explosives Detection Techniques, National Academies Press, Washington D.C., 2004.

NNDC, Accessed June 2009, Brookhaven National Laboratory. <http://www.nndc.bnl.gov/>

Rudakov, T.N., T.J. Rayner, P.A. Hayes, K.L. Russeth, Detection of Explosives by Quadrupole Resonance Method: New Aspects for Security in Detection and Disposal of Improvised Explosives, H. Schubert and A. Kuznetsov, Springer, Netherlands, pp. 191-204, 2006.

Runkle, R.C., T.A. White, E.A. Miller, J.A. Caggiano, B.A. Collins, "Photon and neutron interrogation techniques for chemical explosives detection in air cargo: A critical review," *Nuclear Instruments and Methods in Physics Research A*, Vol. 603, pp. 510-528, 2009.

Sanchez, J.C., S.J. Toal, Z. Wang, R.E. Dugan, W.C. Trogler, "Selective Detection of Trace Nitroaromatic, Nitramine, and Nitrate Ester Explosive Residues Using a Three-Step Fluorimetric Sensing Process: A Tandem Turn-off, Turn-on Sensor," *J Forensic Sci*, Vol. 52, No. 6, 2007.

Senesac, L., T. Thundat, Explosive Vapor Detection Using Microcantilever Sensors in Counterterrorist Detection Techniques of Explosives, J. Yinon, Elsevier, Netherlands, pp. 109-130, 2007.

Sheen, D.M., D.L. McMakin, T. E. Hall, Detection of Explosives by Millimeter-wave Imaging in Counterterrorist Detection Techniques of Explosives, J. Yinon, Elsevier, Netherlands, pp. 237-277, 2007.

Schubert, H., Disposal of Improvised Explosives and – Devices in Detection and Disposal of Improvised Explosives, H. Schubert and A. Kuznetsov, Springer, Netherlands, pp.1-6, 2006.

Shultis, J.K., R.E. Faw, Radiation Shielding, American Nuclear Society Inc., La Grange Park, Illinois, 2000.

Sigaltchik, Y., "*Dokszyc-Parafianow Memorial Book - Belarus (Sefer Dokshitz-Parafianov)*," D. Stockfish, Tel Aviv: Association of Former Residents of Dokszyce-Parafianow in Israel. pp. 274, 1970. <http://www.jewishgen.org/yizkor/dokshitsy/dok274.html>

Singh, S., M. Singh, "Explosives Detection Systems (EDS) for Aviation Security," *Signal Processing,* Vol. 83, pp. 31-55, 2003.

Steinfeld, J.I., J. Wormhoudt, "Explosives Detection: A Challenge for Physical Chemistry," *Annual Review Physics and Chemistry*, Vol. 49, pp. 203-32, 1998.

Todd, M.W., R.A. Provencal, T.G. Owano, B.A. Paldus, A. Kachanov, K.L. Vodopyanov, M. Hunter, S.L. Coy, J.I. Steinfeld, J.T. Arnold, "Application of Mid-infrared Cavity-ringdown Spectroscopy to Trace Explosives Vapor Detection Using a Broadly Tunable (6-8μm) Optical Parametric Oscillator," *Applied Physics B*, Vol. 75, pp. 367-376, 2002.

Tourneur, P.L., "Landmine Detection by Associated Particle Imaging Neutron Technique: Lab and Field Results," *International Atomic Energy Agency*, Padova, Italy, 2007.

Van Neste, C.W., L.R. Senesac, D. Yi, T. Thundat, "Standoff Detection of Explosive Residues Using Photothermal Microcantilevers," *Applied Physics Letters*, Vol. 92, 134102, 2008.

Vourvopoulos, G., P.C. Womble, "Pulsed fast/thermal neutron analysis: a technique for explosives detection," *Talanta*, Vol. 54, pp. 459-468, 2001.

Williams III, R., C. Gesh and R. Pagh, "Compendium of Material Composition Data for Radiation Transport Modeling," *Pacific Northwest National Laboratory*, prepared for DOE, PNNL-15870, 2006.

Wilson, C., "Improvised Explosive Devices (IEDs) in Iraq: Effects and Countermeasures," Navy Department Library, Washington D.C. 2006. <http://www.history.navy.mil/library/online/ied.htm>

X-5 Monte Carlo Team, "MCNP – A General Monte Carlo N-Particle Transport Code, Version 5, Volume I: Overview and Theory," *Los Alamos National Laboratory*, 2003.

Yinon, J., Detection of Explosives by Mass Spectrometry in Counterterrorist Detection Techniques of Explosives, J. Yinon, Elsevier, Netherlands, pp. 41-59, 2007.

Yoshikawa, K., K. Masuda, T. Takamatsu, T. Fujimoto, S. Shiroya, T. Misawa, Y. Takahashi, M. Ohnishi, H. Osawa, E. Hotta, K. Yamauchi, "Current Status of R&D of the Humanitarian Landmine Detection System by a Compact Fusion Neutron Source," *International Atomic Energy Agency*, Padova, Italy, 2007.

Appendix A - Simulated Dose Rates

Table A.1 Ambient dose equivalent rates (mrem hr^{-1}) averaged over a 10 cm radius circular area on roof/floor on yz-plane at x = 60 cm (~above collimator).

Position	Neutron	σ	Photon	σ
A	0.01	0.28	0.00	0.19
B	0.01	0.26	0.00	0.19
C	0.03	0.17	0.00	0.12
D	N/A	N/A	N/A	N/A
E	N/A	N/A	N/A	N/A
F	1.05	0.05	0.32	0.03
G	0.35	0.07	0.09	0.04
H	0.34	0.08	0.15	0.04
I	0.07	0.12	0.02	0.07
J	0.30	0.08	0.15	0.04
K	0.34	0.09	0.17	0.05
L	0.49	0.07	0.04	0.05
M	0.54	0.07	0.04	0.06
N	0.59	0.06	0.05	0.05
O	0.03	0.17	0.00	0.12
P	0.02	0.19	0.00	0.15
Q	1.79	0.04	0.41	0.03
R	3.66	0.03	0.74	0.02
S	0.88	0.06	0.21	0.03
T	0.83	0.05	0.19	0.03
U	0.86	0.06	0.22	0.04
V	0.89	0.06	0.22	0.04
W	N/A	N/A	N/A	N/A
X	N/A	N/A	N/A	N/A
Y	1.56	0.05	0.12	0.04
Z	1.93	0.04	0.14	0.05

Table A.2 Ambient dose equivalent rates (mrem hr^{-1}) averaged over a 10 cm radius circular area on walls on xy-plane at z = -20.32 cm (source elevation).

Position	Neutron	σ	Photon	σ
A	0.00	0.00	0.00	0.00
B	0.00	0.69	0.00	0.83
C	0.00	0.59	0.00	0.76
D	0.00	0.41	0.00	0.45
E	0.02	0.30	0.00	0.27
F	0.01	0.33	0.00	0.38
G	0.01	0.44	0.00	0.44
H	0.01	0.38	0.00	0.47
I	0.16	0.08	0.01	0.09
J	0.11	0.09	0.00	0.10
K	0.05	0.20	0.00	0.20
L	0.02	0.21	0.00	0.23
M	0.01	0.23	0.00	0.31
N	0.01	0.35	0.00	0.39
O	0.04	0.16	0.00	0.18
P	0.04	0.16	0.00	0.19
Q	0.04	0.14	0.00	0.17
R	0.06	0.14	0.00	0.16
S	0.06	0.16	0.00	0.17
T	0.04	0.18	0.00	0.20
U	0.05	0.14	0.00	0.17
V	0.07	0.22	0.00	0.21
W	1.04	0.04	0.03	0.04
X	0.40	0.06	0.02	0.07
Y	0.05	0.13	0.00	0.15
Z	0.05	0.17	0.00	0.17

Table A.3 Ambient dose equivalent rates (mrem hr^{-1}) averaged over a 10 cm radius circular area on walls on xy-plane at z = -20.32 cm (source elevation).

Position	Neutron	σ	Photon	σ
a	0.04	0.48	0.01	0.08
b	0.03	0.19	0.01	0.08
c	0.04	0.17	0.01	0.09
d	0.04	0.18	0.01	0.15
e	0.03	0.17	0.00	0.11
f	0.01	0.42	0.00	0.21
g	0.00	0.52	0.00	0.30
h	0.01	0.37	0.00	0.40
i	0.00	0.73	0.00	0.50
j	0.00	0.71	0.00	0.52
k	0.00	0.93	0.00	0.62
l	1.08	0.04	0.26	0.02
m	3.44	0.02	0.73	0.01
n	9.04	0.03	0.57	0.02
o	13.66	0.04	0.40	0.03
p	1.30	0.05	0.11	0.03
q	0.77	0.05	0.07	0.04
r	0.58	0.06	0.05	0.04
s	0.45	0.07	0.04	0.05
t	0.40	0.08	0.03	0.06
u	0.31	0.07	0.03	0.08
v	0.00	0.00	0.00	0.00

Table A.4 Ambient dose equivalent rates (mrem hr^{-1}) averaged over a 10 cm radius circular area on walls on xy-plane at z = -20.32 cm (source elevation).

Position	Neutron	σ	Photon	σ
aa	9.59	0.02	2.57	0.01
bb	33.01	0.01	7.49	0.01
cc	83.81	0.03	5.90	0.02
dd	84.91	0.04	2.64	0.02
ee	16.01	0.04	1.60	0.02
ff	9.61	0.05	1.22	0.02
gg	6.89	0.05	1.05	0.03
hh	5.44	0.06	0.82	0.03
ii	5.00	0.06	0.75	0.04
jj	2.40	0.08	0.40	0.06
kk	0.00	0.00	0.00	0.00
ll	0.14	0.09	0.04	0.05
mm	0.20	0.09	0.06	0.04
nn	0.28	0.09	0.08	0.05
oo	0.23	0.08	0.06	0.04
pp	0.18	0.09	0.05	0.05
qq	0.17	0.13	0.04	0.05
rr	0.11	0.10	0.03	0.06
ss	0.09	0.14	0.03	0.07
tt	0.10	0.20	0.02	0.08
uu	0.06	0.14	0.02	0.09
vv	0.02	0.28	0.01	0.11

Table A.5 Neutron dose rate (mrem hr $^{-1}$) averaged over circular areas as depicted in Figure 4.6 with a 10.16x10.16 cm collimation hole at (a) 243.84 cm (8 ft.) and (b) 365.76 cm (12 ft.) from the edge of the collimator (elements of matrix: z-dim= columns, y-dim = rows).

(a)

D. Rate	σ	D. Rate	σ	D. Rate	σ	D. Rate	σ	D. Rate	σ
36.00	0.42	49.85	0.56	56.31	0.61	49.60	0.57	35.84	0.42
48.96	0.56	113.00	3.47	240.52	17.46	117.72	5.07	49.32	0.56
55.56	0.61	235.10	15.07	10007.20	237.17	229.57	15.43	55.56	0.61
49.45	0.56	116.47	5.24	247.56	17.58	112.15	3.36	49.41	0.56
35.90	0.42	49.62	0.56	56.37	0.61	49.57	0.56	35.55	0.43

(b)

D. Rate	σ	D. Rate	σ	D. Rate	σ	D. Rate	σ	D. Rate	σ
29.11	0.44	41.88	0.85	50.57	0.98	44.28	0.90	30.09	0.49
42.95	0.82	118.07	11.49	226.71	20.61	134.22	13.61	42.37	0.82
51.58	1.07	231.09	19.16	5793.46	180.18	217.59	18.06	48.85	1.03
42.72	0.80	95.52	6.18	226.95	20.22	109.09	9.55	42.79	0.84
29.55	0.44	43.19	0.83	51.55	1.22	41.73	0.85	29.29	0.44

Table A.6 Neutron Dose rate (mrem hr $^{-1}$) averaged over circular areas as depicted in Figure 4.6 with a 5.08x5.08 cm collimation hole at (a) 243.84 cm (8 ft.) and (b) 365.76 cm (12 ft.) from the edge of the collimator (elements of matrix: z-dim= columns, y-dim = rows).

(a)

D. Rate	σ	D. Rate	σ	D. Rate	σ	D. Rate	σ	D. Rate	σ
6.65	0.17	9.07	0.24	9.51	0.24	8.95	0.23	6.94	0.19
8.88	0.23	13.92	0.33	18.88	0.44	13.59	0.33	8.73	0.23
9.47	0.24	18.42	0.41	6853.15	192.57	19.14	0.47	9.59	0.24
8.91	0.23	14.06	0.33	18.53	0.41	13.53	0.32	8.79	0.23
6.81	0.18	8.71	0.22	9.72	0.25	8.83	0.23	6.87	0.18

(b)

D. Rate	σ	D. Rate	σ	D. Rate	σ	D. Rate	σ	D. Rate	σ
4.94	0.15	5.98	0.18	6.42	0.19	5.79	0.17	4.87	0.15
5.93	0.17	10.02	0.34	18.42	2.25	9.94	0.33	5.99	0.18
6.54	0.20	20.19	2.29	5505.15	175.61	20.02	2.31	6.55	0.19
6.08	0.18	9.82	0.30	15.29	0.93	9.64	0.28	5.94	0.18
4.85	0.15	5.99	0.18	6.24	0.18	5.79	0.17	4.93	0.16

Appendix B - Interference Gamma Rays

Table B.1 Results showing the number of peaks in 4-keV wide bins exceeding 2σ of the count continuum from a pulse height tally for elements with Z =1 - 12.

Element	Energy (MeV)	H	Li	Be	B	C	N	O	F	Na	Mg
H	2.22324	1									
C	1.26176								1		
C	3.68392						1	1			
C	4.439					1	1	1			
C	4.9453										
N	0.72836						1				
N	1.6353		1	1	1	1	1	1		1	1
N	1.88482										
N	2.3128						1				
N	2.7931						1				
N	3.3786				1		1				
N	3.8907						1				
N	4.9151						1				
N	5.1059						1				
N	5.2692										
N	6.4462						1	1			
N	7.0291						1				
N	10.8291										
O	0.87071										
O	1.08793		1				1				
O	2.18448										
O	2.742							1			
O	6.1299							1			
O	6.9171							1			
O	7.1168							1			

Table B.2 Results showing the number of peaks in 4-keV wide bins exceeding 2σ of the count continuum from a pulse height tally for elements with Z =13 - 22.

Element	Energy (MeV)	Al	Si	P	S	Cl	K	Ca	Sc	Ti
H	2.22324									
C	1.26176									
C	3.68392									
C	4.439									
C	4.9453									
N	0.72836									
N	1.6353	1	1		1	1	1		1	1
N	1.88482									
N	2.3128									
N	2.7931									
N	3.3786									
N	3.8907									1
N	4.9151									
N	5.1059									
N	5.2692									
N	6.4462									
N	7.0291									
N	10.8291									
O	0.87071	1								
O	1.08793						1			
O	2.18448		1				1			
O	2.742									
O	6.1299									
O	6.9171		1							
O	7.1168									

Table B.3 Results showing the number of peaks in 4-keV wide bins exceeding 2σ of the count continuum from a pulse height tally for elements with Z =23 - 30.

Element	Energy (MeV)	V	Cr	Mn	Fe	Co	Ni	Cu	Zn
H	2.22324								
C	1.26176								
C	3.68392								
C	4.439								
C	4.9453								
N	0.72836			1					
N	1.6353	1	1	1	1		1	1	1
N	1.88482			1					
N	2.3128								
N	2.7931							1	
N	3.3786								
N	3.8907								
N	4.9151								
N	5.1059								
N	5.2692		1						
N	6.4462								
N	7.0291								
N	10.8291								
O	0.87071								
O	1.08793								
O	2.18448								
O	2.742								
O	6.1299								
O	6.9171								
O	7.1168								

Appendix C - Simulated Materials

Table C.1 Inert material compositions used in simulations (Williams III, 2006).

Material	*Density (g cm^{-3})*	*Element*	*ZAID*	*Atomic Fraction (or weight percent indicated by a – sign)*
Air	0.001205	C	6012	0.000151
		N	7014	0.784437
		O	8016	0.210750
		Ar	18000	0.004671
Aluminum	2.70	Al	13027	1.000000
Antifreeze (Ethylene Glycol)	1.1132	H	1001	0.60
		C	6012	0.20
		O	8016	0.20
Ash (General Wood)	0.641	C	6000	0.13
		O	8016	0.42
		Mg	12000	0.01
		Al	13027	0.02
		K	19000	0.08
		Ca	20000	0.34
Borax	1.73	H	1001	0.465118
		B-10	5010	0.018600
		B-11	5011	0.074423
		O	8016	0.395346
		Na	11023	0.046511
Bricks	1.80	O	8016	0.663062
		Al	13027	0.003916
		Si	14000	0.323140
		Ca	20000	0.007272
		Fe	26000	0.002610
Carbon (Graphite)	1.70	C	6012	1.000000
Cardboard	0.689	H	1001	0.4762
		C	6000	0.2857
		O	8016	0.2381

Table C.2 Inert material compositions used in simulations (Williams III, 2006).

Material	*Density (g cm^{-3})*	*Element*	*ZAID*	*Atomic Fraction (or weight percent indicated by a – sign)*
Ceramic	2.403	O	8016	0.6364
		Al	13027	0.1818
		Si	14000	0.1818
Cherry Wood	0.43	H	1001	0.476191
		C	6012	0.285714
		O	8016	0.238095
Concrete	2.35	H	1001	-0.0056
		O	8016	-0.4983
		Na	11023	-0.0171
		Mg	12000	-0.0024
		Al	13027	-0.0456
		Si	14000	-0.3158
		S	16032	-0.0012
		K	19000	-0.0192
		Ca	20000	-0.0826
		Fe	26000	-0.0122
Copper	8.920	Cu	29000	1.000000
Cotton	1.55	H	1001	0.4762
		C	6000	0.2857
		O	8016	0.2381
Cyanurate (Polyiso)	0.0321	H	1001	0.34500
		C	6012	0.51700
		N	7014	0.06900
		O	8016	0.06900
Ethanol	0.80	H	1001	0.66667
		C	6012	0.22222
		O	8016	0.11111
FertA (nitrogenous)	0.81	H	1001	-0.0300
		C	6012	-0.2500
		N	7014	-0.3600
		O	8016	-0.3460
		S	16000	-0.0140

Table C.3 Inert material compositions used in simulations (Williams III, 2006).

Material	*Density (g cm^{-3})*	*Element*	*ZAID*	*Atomic Fraction (or weight percent indicated by a – sign)*
FertB(non-nitrogenous)	0.99	H	1001	0.001848
		O	8016	0.001657
		Na	11023	0.014039
		Mg	12000	0.000313
		S	16000	0.000183
		Cl	17000	0.497978
		K	19000	0.483587
		Ca	20000	0.000254
		Br	35079	0.000153
Gasoline	0.68	H	1001	0.694164
		C	6012	0.305836
Glass	2.40	O	8016	0.603858
		Na	11023	0.088145
		Si	14028	0.251791
		Ca	20000	0.056205
Granite	2.73	H	1001	0.027122
		C	6012	0.000502
		O	8016	0.607735
		Na	11023	0.025866
		Mg	12000	0.018081
		Al	13027	0.062783
		Si	14000	0.205927
		K	19000	0.013938
		Ca	20000	0.018960
		Fe	26000	0.019086
Herbicide 1	1.17	H	1001	0.487179
		C	6000	0.333333
		N	7014	0.076924
		O	8016	0.102564
Herbicide 2	1.25	H	1001	0.46666
		C	6012	0.40000
		N	7014	0.06667
		Cl	17000	0.06667

Table C.4 Inert material compositions used in simulations (Williams III, 2006).

Material	*Density (g cm^{-3})*	*Element*	*ZAID*	*Atomic Fraction (or weight percent indicated by a – sign)*
Herbicide 3	1.187	H	1001	0.50000
		C	6012	0.28572
		N	7014	0.17857
		Cl	17000	0.03571
Lead	11.35	Pb	82000	1
Limestone	2.35	C	6000	0.2
		O	8016	0.6
		Ca	20000	0.2
Lucite	1.19	H	1001	0.53332
		C	6000	0.33335
		O	8016	0.13333
Nickel	8.9	Ni	28000	1
Nylon	1.14	H	1001	0.578932
		C	6012	0.315803
		N	7014	0.052632
		O	8016	0.052633
Petroleum	0.97	H	1001	0.620069
		C	6012	0.368589
		N	7014	0.003904
		O	8016	0.002523
		S	16000	0.004913
Plexiglass	1.19	H	1001	0.533320
		C	6012	0.333345
		O	8016	0.133335
Polyethylene	0.93	H	1001	0.666662
		C	6012	0.333338
Polystyrene	0.10	H	1001	0.49999
		C	6012	0.50001
Polyurethane (Foam)	0.10	H	1001	0.360023
		C	6012	0.400878
		N	7014	0.076459
		O	8016	0.162639

Table C.5 Inert material compositions used in simulations (Williams III, 2006).

Material	*Density (g cm^{-3})*	*Element*	*ZAID*	*Atomic Fraction (or weight percent indicated by a – sign)*
Potassium Hydroxide	2.044	H	1001	0.33333
		O	8016	0.33333
		K	19000	0.33331
Propane	0.0019	H	1001	0.72726
		C	6012	0.27274
Rubber	0.92	H	1001	0.615370
		C	6012	0.384630
Salt	2.18	Na	11023	0.500000
		Cl	17000	0.500000
Soap	0.801	H	1001	0.614
		C	6000	0.318
		O	8016	0.045
		Na	11023	0.023
Soil	1.61	H	1001	-0.02331
		O	8016	-0.55922
		Si	14000	-0.22259
		Al	13027	-0.06528
		Fe	26000	-0.04015
		Ca	20000	-0.02915
		K	19000	-0.02080
		Na	11023	-0.02272
		Mg	12000	-0.01678
Soy	0.72	H	1001	0.6127
		C	6012	0.3295
		O	8016	0.0578
Steel	7.85	C	6012	-0.0015
		N	7014	-0.0025
		Si	14000	-0.0075
		Cr	24000	-0.1600
		Mn	25055	-0.0500
		Fe	26000	-0.7385
		Ni	28000	-0.0400

Table C.6 Inert material compositions used in simulations (Williams III, 2006).

Material	*Density (g cm^{-3})*	*Element*	*ZAID*	*Atomic Fraction (or weight percent indicated by a – sign)*
Styrofoam	1.06	H	1001	0.49994
		C	6012	0.50006
Sugar	1.54	H	1001	0.50
		C	6012	0.25
		O	8016	0.25
Tissue	1.04	H	1001	0.10117
		C	6012	0.11100
		N	7014	0.02600
		O	8016	0.76183
Titanium	4.54	Ti	22000	1
Water	1.00	H	10001	0.666657
		O	8016	0.333343
Wax	0.93	H	1001	0.675311
		C	6012	0.324689
Wood	0.75	H	1001	0.4762
		C	6012	0.2857
		O	8016	0.2381
Zirconium	6.506	Zr	40000	

Table C.7 Explosive compositions used in simulations (National Research Council, 2004).

Material	*Density (g cm^{-3})*	*Element*	*ZAID*	*Weight Percent*
Ammonium nitrate (AN)	1.70	H	1001	0.0504
$H_4N_2O_3$		C	6012	0
		N	7014	0.3501
		O	8016	0.5997
Ammonium picrate (Expl D)	1.72	H	1001	0.0246
$C_6H_6N_4O_7$		C	6012	0.2928
		N	7014	0.2276
		O	8016	0.4550
Cyclonite (RDX)	1.80	H	1001	0.0272
$C_3H_6N_6O_6$		C	6012	0.1622
		N	7014	0.3784
		O	8016	0.4322
Guanidine nitrate	1.436	H	1001	0.0495
$CH_6N_4O_3$		C	6012	0.0984
		N	7014	0.4589
		O	8016	0.3932
HMTD	0.88	H	1001	0.0581
$C_6H_{12}N_2O_6$		C	6012	0.3462
		N	7014	0.1346
		O	8016	0.4611
HNIW	1.98	H	1001	0.0138
$C_6H_6N_{12}O_{12}$		C	6012	0.1645
		N	7014	0.3836
		O	8016	0.4382
Hydrazine nitrate (HN)	1.20	H	1001	0.0530
$H_5N_3O_3$		C	6012	0
		N	7014	0.4420
		O	8016	0.5009
Nitroglycerin (NG)	1.60	H	1001	0.0222
$C_3H_5N_3O_9$		C	6012	0.1587
		N	7014	0.1850
		O	8016	0.6341

Table C.8 Explosive compositions used in simulations (National Research Council, 2004).

Material	*Density (g cm^{-3})*	*Element*	*ZAID*	*Weight Percent*
Nitrotriazolone (NTO)	1.88	H	1001	0.0155
$C_2H_2N_4O_3$		C	6012	0.1847
		N	7014	0.4308
		O	8016	0.3690
Octogen (HMX)	1.90	H	1001	0.0272
$C_4H_8N_8O_8$		C	6012	0.1622
		N	7014	0.3784
		O	8016	0.4322
Pentaerythritol tetranitrate	1.77	H	1001	0.0255
(PETN)		C	6012	0.1900
$C_5H_8N_4O_{12}$		N	7014	0.1772
		O	8016	0.6073
Picric acid	1.80	H	1001	0.0132
$C_6H_3N_3O_7$		C	6012	0.3146
		N	7014	0.1834
		O	8016	0.4888
Tetrazene	0.45	H	1001	0.0429
$C_2H_8N_{10}O$		C	6012	0.1277
		N	7014	0.7444
		O	8016	0.0850
Tetryl	1.57	H	1001	0.0176
$C_7H_5N_5O_8$		C	6012	0.2928
		N	7014	0.2439
		O	8016	0.4458
Trinitrobenzene (TNB)	1.64	H	1001	0.0142
$C_6H_3N_3O_6$		C	6012	0.3382
		N	7014	0.1972
		O	8016	0.4505
Trinitrotoluene (TNT)	1.65	H	1001	0.0222
$C_7H_5N_3O_6$		C	6012	0.3702
		N	7014	0.1850
		O	8016	0.4226
Triaminoguanidine nitrate	1.54	H	1001	0.0543
(TAGN)		C	6012	0.0719
$CH_9N_7O_3$		N	7014	0.5867
		O	8016	0.2872

Table C.9 Explosive compositions used in simulations (National Research Council, 2004).

Material	*Density (g cm^{-3})*	*Element*	*ZAID*	*Weight Percent*
Triaminotrinitrobenzene	1.93	H	1001	0.0234
(TATB)		C	6012	0.2792
$C_6H_6N_6O_6$		N	7014	0.3255
		O	8016	0.3719
1,3,3-Trinitroazetidine (TNAZ)	1.85	H	1001	0.0210
$C_3H_4N_4O_6$		C	6012	0.1876
		N	7014	0.2917
		O	8016	0.4998
Trinitropyridine	1.86	H	1001	0.0094
$C_5H_2N_4O_6$		C	6012	0.2805
		N	7014	0.2617
		O	8016	0.4484
Urea nitrate	0.69	H	1001	0.0409
$CH_5N_3O_4$		C	6012	0.0976
		N	7014	0.3414
		O	8016	0.5200

Appendix D - Signature Energies Used in Experiments

Table D.1 11 Signature energies used in sections 5.3.1, ^{252}Cf explosive-inert experiments, and 5.3.2, 14.1-MeV explosive-inert experiments.

Element	*Signature Energy (MeV)*
Hydrogen	2.2232
Carbon	1.2618
	4.4390
	4.9453
Nitrogen	1.6353
	1.8848
	2.3128
	5.1059
Oxygen	0.8707
	2.1845
	6.1299

Table D.2 20 Signature energies used in section 5.3.3 for placement of the sample.

Element	*Signature Energy (MeV)*
Hydrogen	2.2232
Carbon	1.2618
	4.4390
	4.9453
Nitrogen	1.6353
	1.8848
	2.3128
	3.6839
	3.3786
	3.8907

	4.9151
	5.1059
	5.2692
	6.4462
	10.8291
Oxygen	0.8707
	2.1845
	6.1299
	6.9171
	7.1168

Table D.3 Nitrogen signature energies used in section 5.4.1, grouping by density.

Element	*Signature Energy (MeV)*
Nitrogen	2.3128
	3.3786
	4.9151
	5.1059
	6.4462

Table D.4 Signature energies used in section 5.4.2, a tiered filter approach.

Element	*Signature Energy (MeV)*
Hydrogen	2.2232
Carbon	4.4390
Nitrogen	2.3128
	3.3786
	4.9151
	5.1059
	6.4462
Oxygen	6.1299
	6.9171

Appendix E - Four Templates and Fifty Target Responses and Standard Deviations Used in Section 5.4.1, Grouping Clutter by Density, to Calculate FOMs and their Standard Deviations and $f_{\pm}(1)$ Values.

Table E.1 VLD, LD, MD and HD templates.

	i	E_i (MeV)	VLD	LD	MD	HD
S_1	1	2.3128	15301.55	9492.46	7078.31	3192.66
$\sigma(S_1)$			41.31	31.87	28.05	20.92
S_2	2	3.3786	3008.22	1839.75	1487.90	842.42
$\sigma(S_2)$			19.40	15.46	14.99	13.03
S_3	3	4.9151	2436.34	1428.65	1173.91	580.34
$\sigma(S_3)$			16.69	12.56	11.86	9.45
S_4	4	5.1059	10402.65	6370.55	4864.00	1996.40
$\sigma(S_4)$			35.88	27.20	24.35	16.64
S_5	5	6.4462	2457.02	1538.74	1158.26	524.44
$\sigma(S_5)$			17.69	13.73	12.35	8.76

Table E.2 Responses and standard deviations for RDX with clutter materials shown.

	i	E_i (MeV)	Air	Aluminum	Bricks	Carbon	Concrete
R_1	1	2.3128	15490.30	6708.81	8015.11	7095.06	6432.09
$\sigma(R_1)$			41.82	27.51	29.66	27.67	27.02
R_2	2	3.3786	3049.51	1498.23	1653.07	1431.43	1347.58
$\sigma(R_2)$			19.52	17.08	15.37	14.60	14.28
R_3	3	4.9151	2479.78	1175.50	1333.19	1101.51	1067.93
$\sigma(R_3)$			16.86	12.23	12.93	10.91	11.32
R_4	4	5.1059	10526.30	4582.70	5732.37	4730.81	4553.89
$\sigma(R_4)$			35.79	23.83	26.37	23.65	23.23
R_5	5	6.4462	2474.17	1136.43	1341.17	1114.32	1088.02
$\sigma(R_5)$			17.81	11.71	13.55	11.92	12.95

Table E.3 Responses and standard deviations for RDX with clutter materials shown.

	i	E_i (MeV)	Copper	Ethanol	FertA	FertB	Gasoline
R_1	1	2.3128	2972.00	8437.61	19124.40	11897.00	8760.83
$\sigma(R_1)$			21.70	30.38	47.81	35.69	30.66
R_2	2	3.3786	801.99	1637.55	3667.87	2461.08	1698.42
$\sigma(R_2)$			13.96	14.90	21.64	17.72	15.46
R_3	3	4.9151	522.37	1286.68	2620.09	1952.86	1336.05
$\sigma(R_3)$			9.51	11.97	17.82	15.04	12.02
R_4	4	5.1059	1775.45	5503.64	13945.50	8043.89	5718.43
$\sigma(R_4)$			16.87	25.87	41.84	30.57	26.31
R_5	5	6.4462	462.80	1298.49	3628.48	1902.17	1359.11
$\sigma(R_5)$			9.07	12.60	22.13	15.22	13.18

Table E.4 Responses and standard deviations for RDX with clutter materials shown.

	i	E_i (MeV)	Glass	Granite	Nylon	Petroleum	Plexiglass
R_1	1	2.3128	6615.71	5897.31	10661.40	7858.39	7231.48
$\sigma(R_1)$			27.12	25.95	34.12	29.08	28.20
R_2	2	3.3786	1357.44	1256.06	2009.89	1524.05	1399.92
$\sigma(R_2)$			14.12	13.94	16.28	14.33	14.00
R_3	3	4.9151	1113.50	989.28	1493.23	1190.47	1115.83
$\sigma(R_3)$			11.69	11.28	12.84	11.43	11.05
R_4	4	5.1059	4400.98	4153.49	7464.47	5146.46	4710.16
$\sigma(R_4)$			23.77	22.84	29.86	24.70	23.55
R_5	5	6.4462	1060.85	947.95	1855.16	1229.28	1107.66
$\sigma(R_5)$			12.09	11.38	15.58	12.29	11.74

Table E.5 Responses and standard deviations for RDX with clutter materials shown.

	i	E_i (MeV)	Poly-ethylene	Poly-urethane	Rubber	Salt	Soil
R_1	1	2.3128	7365.98	15112.80	7860.44	8070.17	7792.18
$\sigma(R_1)$			27.99	40.81	29.08	29.86	29.61
R_2	2	3.3786	1414.44	2966.93	1508.74	1768.32	1591.04
$\sigma(R_2)$			13.86	19.29	14.18	15.38	15.12
R_3	3	4.9151	1120.64	2392.90	1195.66	1349.40	1260.93
$\sigma(R_3)$			11.21	16.51	11.60	12.28	12.23
R_4	4	5.1059	4770.83	10279.00	5109.05	5433.35	5324.44
$\sigma(R_4)$			23.85	35.98	24.52	25.54	25.56
R_5	5	6.4462	1125.86	2439.87	1209.53	1311.92	1265.46
$\sigma(R_5)$			11.82	17.57	12.22	12.46	12.78

Table E.6 Responses and standard deviations for RDX with clutter materials shown.

	i	E_i (MeV)	Soy	Steel	Water	Wax	Wood
R_1	1	2.3128	9250.55	3413.32	7735.64	7284.02	9934.29
$\sigma(R_1)$			31.45	20.14	29.40	27.68	32.78
R_2	2	3.3786	1782.14	882.85	1493.47	1393.26	1925.98
$\sigma(R_2)$			15.15	12.10	14.49	13.52	15.41
R_3	3	4.9151	1413.96	638.32	1192.03	1108.22	1546.76
$\sigma(R_3)$			12.44	9.38	11.80	10.97	13.15
R_4	4	5.1059	6067.95	2217.35	5016.39	4715.92	6604.44
$\sigma(R_4)$			26.70	16.41	24.58	23.58	27.74
R_5	5	6.4462	1437.99	586.08	1179.90	1114.22	1555.82
$\sigma(R_5)$			13.66	8.44	12.15	11.70	14.16

Table E.7 Responses and standard deviations for inert materials shown used as the clutter and the sample.

	i	E_i (MeV)	Air	Aluminum	Bricks	Carbon	Concrete
R_1	1	2.3128	173.68	530.73	353.55	120.91	350.56
$\sigma(R_1)$			5.92	12.58	10.82	6.88	10.17
R_2	2	3.3786	113.28	410.54	253.17	116.66	263.35
$\sigma(R_2)$			5.02	13.59	8.94	8.38	10.53
R_3	3	4.9151	52.77	226.52	149.40	18.99	128.37
$\sigma(R_3)$			3.39	6.80	8.08	1.88	6.43
R_4	4	5.1059	112.30	361.99	749.24	23.51	555.84
$\sigma(R_4)$			5.73	8.36	11.76	2.11	9.34
R_5	5	6.4462	36.65	216.86	192.15	15.97	162.19
$\sigma(R_5)$			2.53	6.16	6.71	1.71	6.65

Table E.8 Responses and standard deviations for inert materials shown used as the clutter and the sample.

	i	E_i (MeV)	Copper	Ethanol	FertA	FertB	Gasoline
R_1	1	2.3128	700.94	72.58	15652.90	489.20	81.15
$\sigma(R_1)$			17.52	5.17	43.83	10.27	5.67
R_2	2	3.3786	431.85	82.82	3027.56	378.79	72.67
$\sigma(R_2)$			13.99	6.07	20.29	8.64	5.03
R_3	3	4.9151	165.68	26.50	1776.74	178.36	21.54
$\sigma(R_3)$			7.72	3.77	14.93	5.82	2.10
R_4	4	5.1059	192.30	30.09	12361.00	168.09	28.70
$\sigma(R_4)$			8.58	3.03	40.79	5.87	2.34
R_5	5	6.4462	95.10	15.41	3461.42	84.35	14.78
$\sigma(R_5)$			4.18	1.87	22.15	4.73	1.69

Table E.9 Responses and standard deviations for inert materials shown used as the clutter and the sample.

	i	E_i (MeV)	Glass	Granite	Nylon	Petroleum	Plexiglass
R_1	1	2.3128	438.82	415.83	5548.10	495.11	94.63
$\sigma(R_1)$			11.23	11.81	25.52	8.76	6.18
R_2	2	3.3786	248.36	270.55	1042.43	151.85	87.12
$\sigma(R_2)$			9.41	9.23	12.41	6.09	6.80
R_3	3	4.9151	161.24	142.70	638.28	72.03	22.80
$\sigma(R_3)$			7.11	7.38	8.55	3.39	2.75
R_4	4	5.1059	170.87	524.38	4272.08	363.81	27.83
$\sigma(R_4)$			8.30	9.49	23.07	6.99	3.02
R_5	5	6.4462	103.50	104.71	1155.91	112.25	13.34
$\sigma(R_5)$			6.25	5.96	12.60	3.99	1.60

Table E.10 Responses and standard deviations for inert materials shown used as the clutter and the sample.

	i	E_i (MeV)	Poly-ethylene	Poly-urethane	Rubber	Salt	Soil
R_1	1	2.3128	68.98	1047.95	74.18	619.31	300.01
$\sigma(R_1)$			4.99	13.00	5.02	11.09	10.14
R_2	2	3.3786	69.46	278.96	69.42	462.23	241.38
$\sigma(R_2)$			5.49	7.31	5.03	10.03	9.20
R_3	3	4.9151	17.70	145.65	21.68	197.78	105.02
$\sigma(R_3)$			1.88	4.78	2.79	6.59	6.69
R_4	4	5.1059	26.73	808.34	27.51	257.70	392.04
$\sigma(R_4)$			2.60	11.88	2.26	6.83	8.90
R_5	5	6.4462	15.33	232.15	17.84	155.55	122.81
$\sigma(R_5)$			2.26	6.06	3.39	4.42	5.27

Table E.11 Responses and standard deviations for inert materials shown used as the clutter and the sample.

	i	E_i (MeV)	Soy	Steel	Water	Wax	Wood
R_1	1	2.3128	85.51	552.66	108.73	68.27	98.39
$\sigma(R_1)$			6.12	11.39	7.24	4.97	6.58
R_2	2	3.3786	76.74	397.86	89.91	64.59	86.21
$\sigma(R_2)$			5.43	9.27	7.27	5.16	6.04
R_3	3	4.9151	27.11	191.76	30.94	18.47	29.22
$\sigma(R_3)$			2.74	6.14	4.29	1.90	3.25
R_4	4	5.1059	28.80	265.75	34.78	27.19	31.12
$\sigma(R_4)$			2.33	6.80	4.03	2.60	2.94
R_5	5	6.4462	18.27	157.09	16.74	13.98	19.13
$\sigma(R_5)$			3.02	5.09	3.23	1.64	2.78

Appendix F - Additional Figures

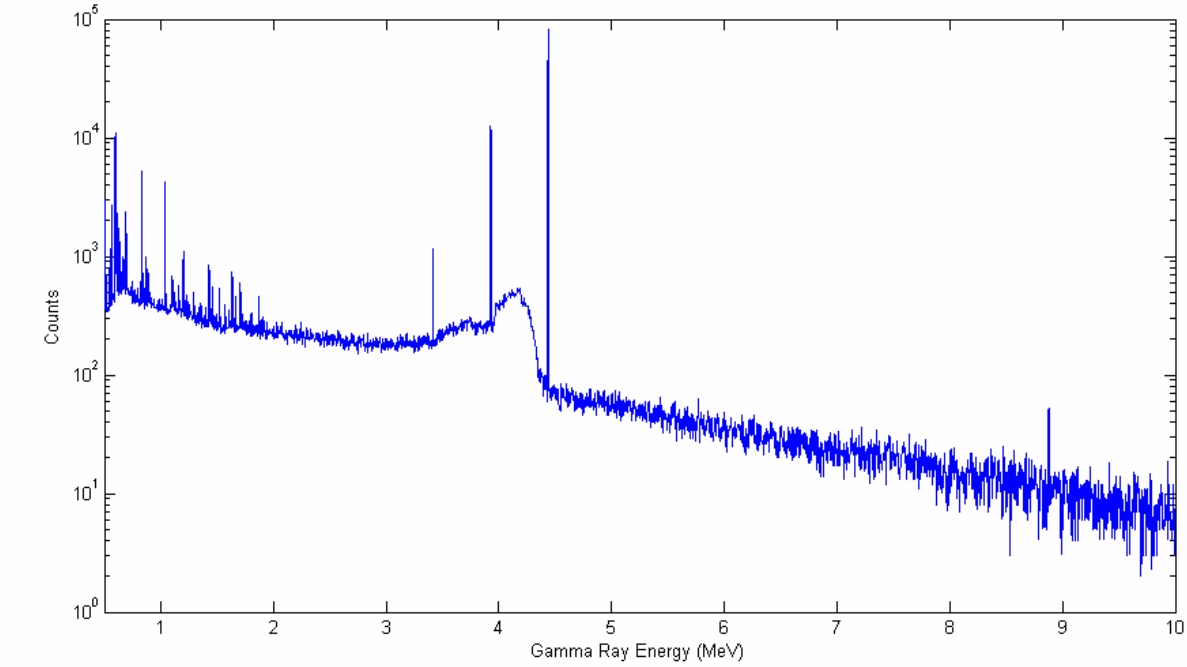

Figure F.1 Simulated pulse height tally spectrum for a sample containing pure C irradiated by 14.1-MeV neutrons.

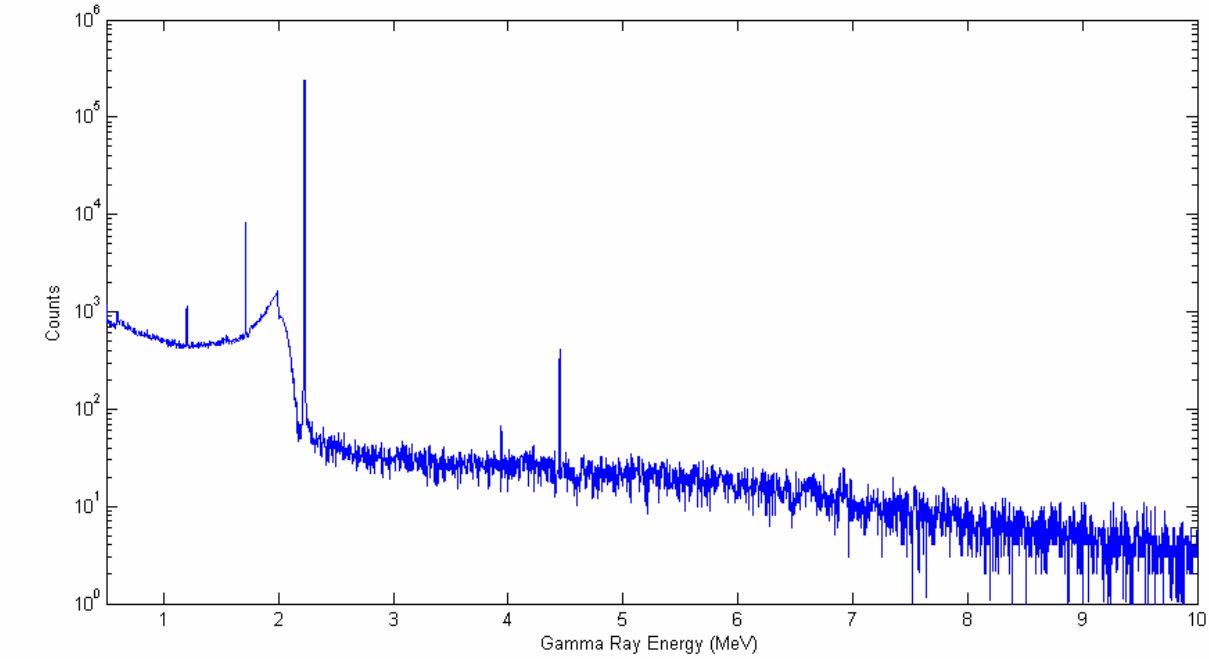

Figure F.2 Simulated pulse height tally spectrum for a sample containing pure H irradiated by 14.1-MeV neutrons.

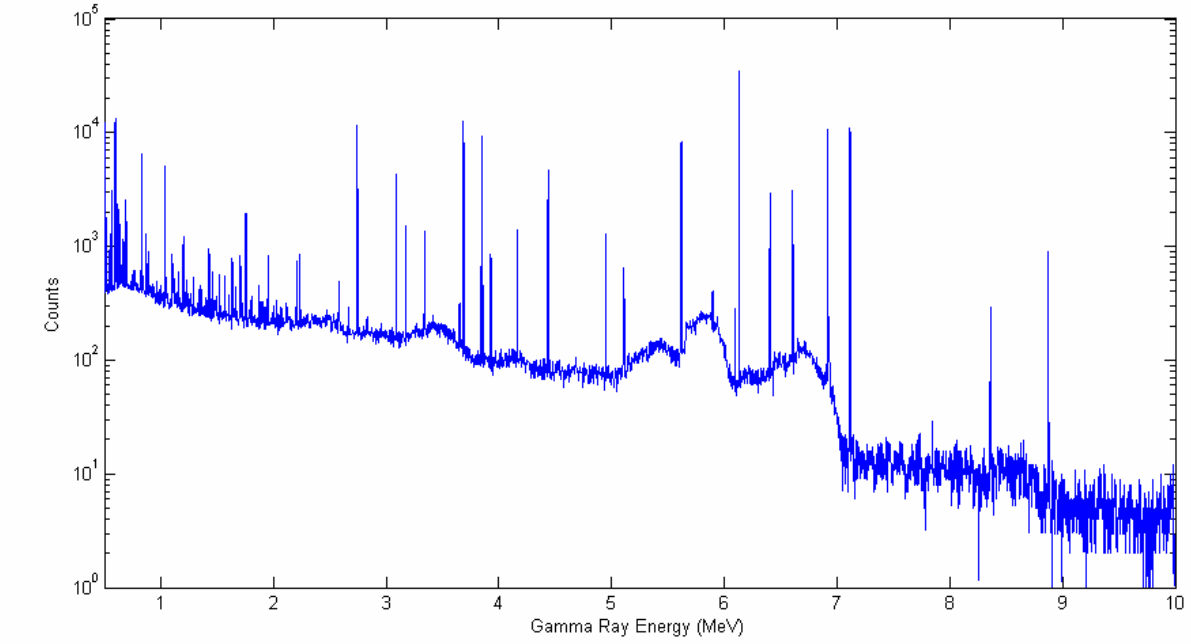

Figure F.3 Simulated pulse height tally spectrum for a sample containing pure O irradiated by 14.1-MeV neutrons.

Appendix G - Sample MCNP5 Input File and Perl Script

Table G.1 A typical MCNP input file.

```
Explosive Target Interrogation
C ************ BLOCK 1 -- CELLS  ******************************
1   2  -1.80  -15                imp:p,n=1
2   1  -7.82   15 -16            imp:n,p=1
3   0           16 -20           imp:n,p=1
4   3  -2.7     20 -21           imp:n,p=1
5   0           21   -999        imp:n,p=1
6   6  -1       -30              imp:n,p=1
13  0       999                  imp:n,p=0

C ************ BLOCK 2 -- SURFACES ***************************
15  RCC  0 0 39.624  0 0 20.7517  7.62
16  RCC  0 0 39.504  0 0 20.9917  7.74
20  RPP  -100   100    -50   50   0   100
21  RPP  -100.2 100.2  -50.2 50.2 -0.2 100.2
30  RPP  -98 98   -49.95 -39.95   2  98
999  SO   500.0

C ************ BLOCK 3 -- COMMANDS ****************************
mode n p
NPS 50000000
c
c ------ SOURCE: plane parallel cylindrical neutron beam
SDEF  POS= 0 -150 50
     AXS= 0 1 0
     EXT= 0
     RAD= d1
     PAR= 1
     VEC= 0 1 0
     DIR= 1
     ERG= 14.1
SI1  0  7.62
SP1  -21  1
c
F15:p
       121.92 -100 50 10
c      Energy Bins:
E15  0. 0.8687 0.8727 1.2598 1.2638
       1.6333 1.6373  2.2212 2.2252
       2.3108 2.3148  3.3766 3.3806
       3.8887 3.8927  4.4370 4.4410
       4.9131 4.9171  4.9433 4.9473
```

```
       5.1039 5.1079  6.1279 6.1319
       6.4442 6.4482  6.9151 6.9191
       7.1148 7.1188 10.8271 10.8311
c
c ------- MATERIALS:
c   ************************************************************
c    Carbon Steel
c     Density = 7.82 g cm-3
c   ************************************************************
m1    26000.55d  0.95510
        6000.74c  0.04490
c
c ************************************************************
c    RDX    (C3H6N6O6)
c    Density = 1.8 g cm-3
c ************************************************************
m2       1001.74c -.0272
         6000.74c -.1622
         7014.74c -.3784
         8016.74c -.4322
c
c  ************************************************************
c     Aluminum
c     Density = 2.70 g cm-3
c  ************************************************************
m3   13027.74c   1.00000
c
c ************************************************************
c     Artificial Clutter
c     Density = 1 g cm-3
c ************************************************************
m6       1001.74c  0.85
         6000.74c  0.05
         8016.74c  0.10
```

Table G.2 A sample Perl script for MCNP output processing.

```
#! /usr/bin/perl
# the program reads a MCNP output file and copies data to a user inputted output file
# read in two command line parameters, $ARGV[0]= INFILE name, $ARGV[1]= OUTFILE
# name. Check for correct number of command line parameters (2), if not print error and die.

if ($#ARGV < 1 || $#ARGV > 1)
{
  print "Incorrect number of command line parameters.\n",
        "The first parameter should be an input file name.\n",
        "The second parameter should be an output file name.\n";
  die;
}
else
{
 print "Input  file name is: $ARGV[0]\n",
         "Output file name is: $ARGV[1]\n";

open(INFILE,"<$ARGV[0]");
open(OUTFILE,">$ARGV[1]");

# initializing variables
$r=1;
$a=1;
print OUTFILE $ARGV[0], "\n";
# regular expression stores fluence and its standard deviation into an array.
# The fluence and its standard deviation is scaled by a numerical factor of 1E12
while($line = <INFILE>)
{
   if( $line =~ /^\s*detector\slocated\sat\sx,y,z\s=([\s-]\d\.\d+E[+-]\d+)([\s-]\d\.\d+E[+-
                    ]\d+)(\s\d\.\d+E[+-]\d+)\s*$/)
    {

     print OUTFILE $r, "\n";
     $r++;
     $j=4;
        for($i=1;$i<=$j;$i++)
        {
          $line = <INFILE>;
        }

          do
          {
            $line =~ /^\s*(\d\.\d+E[+-]\d+)\s+(\d\.\d+E[+-]\d+)\s(\d\.\d+)/;
             $array1[$a]= $2*1E12;
             $array2[$a]= $2*$3*1E12;
```

```
            $a++;
               $line = <INFILE>;
               $line = <INFILE>;
            } until  (  $line =~ /^\s+total/ || $line =~ /^ \s*$/ );
        }
}

print OUTFILE "\n";
print OUTFILE "\n";
   $d=16;
# printing stored variables in array to output file.
    for($c=1; $c<=$d; $c++)
        {
          print OUTFILE $array1[$c], "\n", sprintf("%.3f",  $array2[$c]), "\n";
        }
# Close the file
close INFILE;
close OUTFILE;
}
```